Spinning Arc Plasma Reactor

Characterisation of a novel reactor design for synthetic fuel production

T. Speelman

TU Delft

Spinning Arc Plasma Reactor

Characterisation of a novel reactor design for synthetic fuel production

by

T. Speelman

to obtain the degree of Master of Science
at the Delft University of Technology,
to be defended publicly on Monday September 30, 2019 at 02:00 PM.

Student number: 1359525

Thesis committee:		
	Prof. dr. ir. W. de Jong,	TU Delft, supervisor
	Prof. dr. D.J.E.M. Roekaerts	TU Delft
	Dr. Ir. E.L.V. Goetheer	TU Delft
	Dr. Ir. G. S. J. Sturm,	TU Delft
	Ir. J. van Kranendonk,	Zero Emission Fuels

TU Delft

Abstract

In recent years, the energy transition has led to increasingly higher installed capacities of intermittent renewable energy sources. This has sparked the interest in power-to-fuel technology to store excess renewable energy in the chemical bonds of synthetic fuels. As a highly reactive, turn-key process, plasma-chemical conversion offers a promising approach to power-to-fuel technology. However, recent studies have shown limitations in either energy efficiency, conversion or flow rate.

The novel Spinning Arc Plasma Reactor (SAPR) developed by J. van Kranendonk stabilises the plasma by mechanical rotation with the potential to contain a liquid film for in-situ product removal. The aim of this thesis is to characterise this reactor by studying the effect of rotational confinement on the reactor performance. To this end, the prototype initially built by J. van Kranendonk was further developed. A wealth of recent studies on the plasma-chemical conversion of CO_2 as a step in the formation of synthetic fuels serves as a benchmark to compare reactor performance of the SAPR concept against.

A series of experiments with argon were performed to establish the relationship between the system variables (pressure, power, flow rate and rotational speed) and the plasma parameters (electron temperature and electron density). Based on this knowledge, a series of experiments with CO_2 were performed to establish the relationship between the reactor performance measured by the conversion and energy efficiency and the system variables: pressure, power and flow rate. The maximum conversion of about 30% to 55% was obtained at an energy efficiency of approximately 0.25% and the maximum energy efficiency of about 3% was achieved at a conversion of approximately 8.5% conversion. Similarly to other studies, improvements to either one came at the expense of the other.

The performance of the SAPR proved comparable to dielectric barrier and other glow discharges but was outperformed by microwave and gliding arc discharges. Especially energy efficiency was inferior to these configurations. Further analysis of the discharge emission spectra suggested that CO_2 dissociation mainly occurred through electron impact excitation. This explains the large difference in energy efficiency as microwave and gliding arc configurations are able to exploit more energy efficient dissociation channels. Nonetheless, this study was able to further develop the concept and has laid the ground work to explore the potential effect of a liquid film and in-situ product removal on the reactor performance.

Contents

Nomenclature

Physics Constants

h	Planck constant	$6.626\,070\,04 \times 10^{-34}\,\mathrm{m^2\,kg\,s^{-1}}$
k_b	Boltzmann constant	$1.380\,648\,52 \times 10^{-23}\,\mathrm{m^2\,kg\,s^{-2}\,K^{-1}}$
N_a	Avogadro's number	$6.02 \times 10^{23}\,\mathrm{mol^{-1}}$
q_e	Elementary charge	$1.602 \times 10^{-19}\,\mathrm{J}$
R	Universal Gas Constant	$8.314\,\mathrm{J\,mol^{-1}\,K^{-1}}$

Greek Symbols

$\bar{\varepsilon}$	Mean energy	eV
χ	Conversion	-
η	Energy efficiency	-
λ	Wavelength	m
μ	Cross section	$\mathrm{cm^2}$
μ	Reduced mass	kg
υ	Collision frequency	$-1]$
ε	Energy	eV
ε_m	Most probable energy	eV

Roman Symbols

ΔH	Dissociation enthalpy	eV/molecule
$\dot{n}$	molar flowrate	$\mathrm{mol\,s^{-1}}$
A	Transition probability	$\mathrm{s^{-1}}$
C	Conversion factor	-
E	Energy	$\mathrm{cm^{-1}}$
g	Statistical weight	-
I	Intensity	$\mathrm{m^{-3}\,s^{-1}}$
J	Rotational number	-
K	Calibration factor	-
k	Reaction rate coefficient	$\mathrm{cm^3\,s^{-1}}$
m	Mass	kg
n	Number density	$\mathrm{m^{-3}}$
P	Power	W

p	Pressure	Pa
T	Temperature	K
V	Volumetric flow rate	$m^3 s^{-1}$
v	Vibrational number	-

Subscript Denotation

e	Electron
g	Gas
r	Rotational

Acronyms

AC alternating current. 11

DBD dielectric barrier discharge. 10, 11, 12, 13, 14, 15, 16, 48, 49, 51

DC direct current. 9, 10, 12

EEDF electron energy distribution function. 4, 5, 24, 30, 43, 46

GA gliding arc. 10, 11, 12, 13, 14, 15, 16, 47, 48, 49

GAP gliding arc plasmatron. 11, 15

LTE local temperature equilibrium. 3, 7, 10, 11, 24

MW microwave. 10, 11, 12, 13, 14, 15, 16, 48, 49

OES optical emission spectroscopy. 20

POM polyoxymethylene. 20

RF radio frequency. 10, 12, 13

SAPR spinning arc plasma reactor. 1, 2, 17, 19, 20, 37, 43, 48, 49

SEI specific energy input. 13, 14, 15, 47

VT vibrational-translational. 5, 14, 47

VV vibrational-vibrational. 5

1 Introduction

The detrimental effect CO_2 emissions have on our climate and environment emphasises the need to reduce our present dependence on fossil fuels in an endeavour to mitigate climate change. Especially now, as costs dwindle and technology advances, the transition towards renewable energy generation accelerates with increasingly higher installed capacities of wind and solar [1]. However, the wide-scale adoption of renewable energy poses a challenge; the irregular and intermittent nature as well as the regional disparity in the availability of renewable energy sources hampers the decarbonisation of the energy sector and necessitates large-scale energy storage and transportation [2].

Power-to-fuel technology enables the long-term storage of excess renewable energy in the chemical bonds of synthetic chemical fuels [3]. Easily stored and transported, energy-dense synthetic fuels are well-suited to cope with seasonal fluxes and regional disparity in the availability of renewable sources [2]. In this way, power-to-fuel technology can complement the use of batteries, which have far superior round trip efficiency and are more suited for short-term storage. Moreover, when coupled with carbon capture technology, the power-to-fuel process is able convert CO_2 from a detrimental greenhouse gas to carbon-neutral fuels and chemicals with renewable energy, thereby closing the carbon loop. These liquid synthetic fuels, often referred to as solar fuels, are dense energy carriers compatible with existing infrastructure for efficient storage and transportation. This enables the production in remote locations where conditions may be more suitable for generating renewable energy. Alternatively, the use of solar fuels as so-called drop-in fuels can decrease the carbon footprint of transportation sectors with a challenging shift towards electrification for instance, aviation [4]. Nonetheless, for any power-to-fuel technology to succeed it is vital that the technology is able to follow the irregular and intermittent supply of renewable energy.

The abundance of exited and highly reactive particles in plasmas enhances chemical reaction kinetics, making plasma-driven processes promising approach for power-to-fuel conversion. This energetic environment is able to activate even most thermodynamic stable molecules such as CO_2. In addition, plasma technology is what is called a turn-key process, able to instantaneously turn on and off, which makes it suitable for peak shaving and stabilisation of excess intermittent renewable energy. Another advantage is the lack of a dependence on any rare earth metals. Despite these benefits, for plasma-assisted chemical conversion to yield a viable alternative to other novel gas conversion technologies, mainly electrolysis, it should have an energy efficiency of at least 60% according to Snoeckx and Bogaerts [5]. Unfortunately, recent studies have shown limitations in either energy efficiency, conversion rate or mass flow rate [6].

This thesis introduces a novel plasma configuration, which is based on the mechanical stabilisation of a thermal arc. The spinning arc plasma reactor (SAPR) design distributes the plasma over a broad range instead of a narrow arc. The plasma is thereby confined in a rotational field. This rotational field may enable to maintain a liquid film to facilitate in-situ separation. This is a novel characteristic that may open new avenues to increase the conversion by shifting the reaction equilibrium in favour of product formation. This thesis deals with the particular case of plasma chemical dissociation of CO_2 as the preliminary step in the production of synthetic fuels. The SAPR design was initially conceptualised by Van Kranendonk. This thesis builds upon the work of Van Kranendonk to develop and characterise the SAPR prototype.

1.1. Aims and objectives of research

The aim of this thesis work is to explore the effect of rotational confinement and stabilisation of the plasma on the reaction performance. An experiment with a non-reactive species aims to understand the relationship between the system parameters and the observed plasma confinement and stabilisation. These system parameters are subsequently manipulated in an experiment with a reactive species, to determine the effect on the reaction performance. Lastly, the reaction performance is compared to other plasma reactor designs.

This thesis seeks to address the following research questions:

1. What is the relationship between the system parameters and plasma parameters, i.e. what is the effect of manipulating pressure, power, flow rate and rotational speed and measuring the effect on the electron temperature, electron density and gas temperature for a non-reactive species, argon?

2. What is the relationship between the system parameters and the reactor performance, i.e. what is the effect of manipulating pressure, power and flow rate and measuring the conversion and energy efficiency for a reactive species, CO_2?

3. How does the measured CO_2 reactor performance compare against a benchmark of other reactor configurations?

This study was exploratory and was conducted in the form of a series of experiments with a SAPR. The effect of the system parameters (pressure, power, flow rate and rotational speed) on the plasma parameters (electron temperature, electron density and gas temperature) was measured with spectroscopy. The general structure of the plasma at each measurement was recorded with a digital camera. With the recorded spectra, the electron temperature, electron density and gas temperature were calculated. The reactor performance of the CO_2 dissociation was calculated by analysing the samples from the reactor effluent with a off-stream gas chromatograph in combination with measurement of the feed flow rate and the energy consumption of the plasma reactor. These latter results were compared against a benchmark of other plasma configuration outlined in literature review.

1.2. Thesis structure

This thesis work is composed of six chapters, covering this introduction followed by the literature review, methodology, results, discussion and conclusion.

Chapter 2 provides a brief overview of the fundamentals of plasma physics and plasma chemistry, including the elementary plasma-chemical reactions. Chapter 2 continues to discuss the relevant mechanics in the plasma-chemical conversion of CO_2, most importantly the different dissociation channels. The chapter concludes with a current state of technology. This current state of technology establishes a benchmark which will eventually be used to compare the reactor performance of the SAPR against.

This thesis work continues with the third chapter that is concerned with the methodology. Chapter 3 starts by providing an overview of the experimental setup followed by a description of the SAPR design. The chapter continues by describing the experimental procedures and analytical methods used to characterise the SAPR and conclude with an overview of the design alternations.

Chapter 4 covers the experimental results of both the argon and CO_2 experiments. The chapter starts with the results of argon experiments used to characterise the plasma behaviour of the SAPR and continues with the CO_2 dissociation experiments used to characterise the reactor performance of the SAPR. This is followed by the results of both experiments at a shorter discharge length. Finally, chapter 4 concludes with a comparison against the benchmark established in Chapter 2.

Chapter 5 discusses the results of Chapter 4. Chapter 5 starts with a discussion on the plasma behaviour observed in the argon experiments. This is followed by a discussion on the reactor performance, focusing on the observed emissions in an effort to retrieve the dissociation mechanism. Thereafter, the chapter addresses the differences between the argon and CO_2 plasmas. The remaining part of Chapter 5 reviews the methodology outlined in Chapter 2 and revisits the comparison made in Chapter 4. Last, the chapter concludes with recommendations for future work.

The last chapter, Chapter 6, wraps up the thesis and provides the final conclusions about the SAPR and future outlook.

2

Plasma chemistry

This chapter introduces the main concepts of plasma chemistry. Main topics that will be covered are the fundamentals of plasma physics, plasma chemistry, and plasma-chemical CO_2 dissociation and the current state of plasma-chemical dissociation of CO_2

2.1. Fundamentals of plasma physics

Plasma is an ionised gas, an electrically neutral medium of unbound positively charged ions and negatively charged electrons. Although rarely seen on earth, plasma is the most abundant state of ordinary matter in the universe. On earth, most natural luminous phenomena are plasmas, such as lightning, the Aurora Borealis and St. Elmo's fire.

Plasma is the most energetic state of matter. Molecules become more energetic upon heat addition, eventually this results in phase transitions from a solid state, into liquid and subsequently into a gaseous state. As molecules become even more energetic, matter attains the plasma state, as molecules dissociate into atoms, and atoms dissociate into unbound ions and electrons [7, 8].

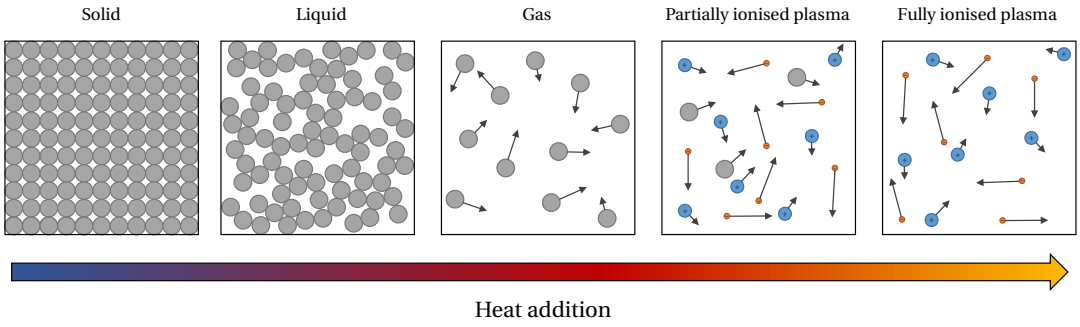

Figure 2.1: Phase transitions of ordinary matter upon heat addition.

Plasma is a distinct state of matter with unique properties due to the presence of a significant amount of electrically charged particles. The unbound electrically charged particles make the plasma highly electrically conductive, internally interactive, and responsive to electromagnetic fields [7].

2.1.1. Basic definitions

Ionisation is required to instigate and sustain the plasma. Ionisation is the process where neutral particles dissociate in unbound ions and electrons. Not all particles need to be ionised; in plasma-chemical applications gases are commonly only partially ionised. The *ionisation degree* of a plasma is defined as the number of ions relative to the total number of heavy particles. A *partially ionised plasma* is a plasma with a low ionisation degree. When the ionisation degree approaches unity, it is referred to as a *fully ionised plasma*.

Plasmas are classified as either *thermal* or *non-thermal* based on the relative temperatures of electrons, ions and neutrals. A thermal plasma is in local temperature equilibrium (LTE) i.e. the relative temperatures

of its components are equal. The plasma is therefore characterised by a single temperature at any point in space. In a non-thermal plasma, the relative temperature of electrons significantly exceeds that of heavy particles. Typically, electron temperatures are around 1 eV whilst the gas temperature can remain close to room temperature [7]. However, plasma-chemical applications require both non-equilibrium, found in non-thermal plasmas and high electron density, commonly found in thermal plasmas. This requires a transitional type of plasma, a so-called *warm plasma*, which still has a high degree of non-equilibrium albeit with gas temperatures around 2000-3000 K; significantly higher than room temperature [5].

Left to its own devices, plasma exhibits a strong tendency to become electrically neutral [9]. Within the plasma, the charge density of ions and electrons are approximately equal due to the electrical forces between opposite charge species. This condition, referred to as *quasi-neutrality*, can only be distorted by external electric fields or by thermal energy of the plasma itself. Futhermore, a plasma is referred to as *optically thin* if radiation absorption is assumed to be negligible.

2.1.2. Electron energy distribution function

Plasma-chemical processes, such as ionisation, excitation and dissociation, depend on the energy level of the electron. In the kinetic theory of gases, the kinetic energy of individual particles in thermodynamic or kinetic equilibrium obeys a Maxwell-Boltzmann distribution. It is commonly assumed that the electron energy distribution function (EEDF) of a plasma, the probability density function for an electron to have energy ε, is described by a Maxwell-Boltzmann distribution strongly dependent on the electron temperature T_e [7],

$$f(\varepsilon) = 2\sqrt{\frac{\varepsilon}{\pi(k_B T_e)^3}} \exp\left(-\frac{\varepsilon}{k_B T_e}\right) \tag{2.1}$$

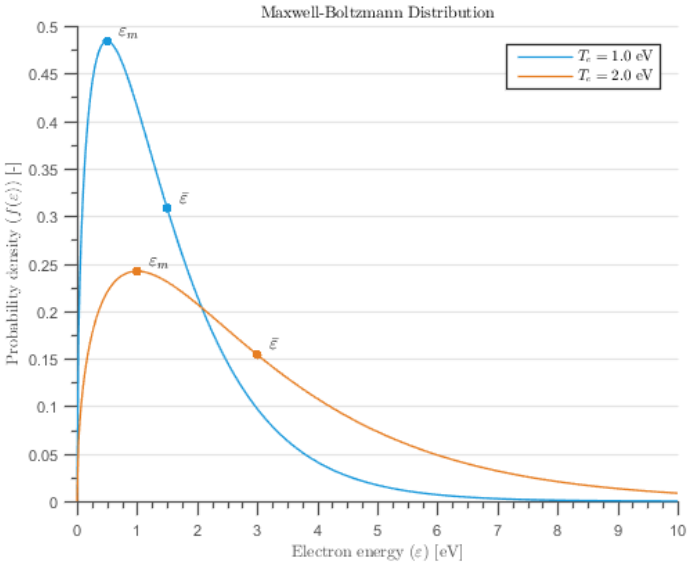

Figure 2.2: Maxwell-Boltzmann electron energy distribution function for various mean electron temperatures.

The most probable kinetic energy in a Maxwellian gas is $\varepsilon_m = k_B T_e/2$ and the mean energy is equal to $\bar{\varepsilon} = 3/2 k_B T_e$ [9]. Figure 2.2 illustrates the EEDF for different electron temperatures. When the electron temperature of the gas increases, the electron population distributes to higher energy levels. For a gas confined to a fixed volume, the area below the distribution function remains constant. As electrons populate the high energy tail, the lower energy levels depopulate, spreading the distribution function for higher electron temperatures, as shown in Figure 2.2.

2.2. Fundamentals of plasma chemistry

In his comprehensive work, Roth [9] defined plasma chemistry as: '...a branch of the discipline of chemistry that concerns itself with chemical reactions which occur in the presence of a plasma'. According to Fridman [7] there are three important features that can significantly intensify traditional chemical processes. First,

plasma components are able to achieve temperatures inconceivable by traditional chemical technology. Second, plasma contains a high concentration of energetic and chemically active species. Third, plasma-assisted systems are able to produce chemically active species far from thermodynamic equilibrium, whilst the bulk temperature of the medium remains low.

2.2.1. Elementary plasma-chemical reactions

Unbound electrons play a key role in plasma-chemical reactions as primary energy carriers. Electrons receive their energy from the electric field and distribute this energy to heavy particles via collisions. These collisions may unleash various chemically active species including ions, radicals, active atoms, high-energy photons and excited atoms and molecules. The reaction rate coefficients of electron impact reactions are dependent on the EEDF [10].

$$k = \gamma \int_0^\infty \varepsilon \sigma(\varepsilon) f(\varepsilon) \, \mathrm{d}\varepsilon \tag{2.2}$$

Here, ε is the electron energy, $\sigma(\varepsilon)$ is the cross section of the collision process, $f(\varepsilon)$ is the EEDF and γ is the conversion units constant. The following subsections describe the different interactions between the various plasma components to understand the role of each in plasma production and plasma chemistry. In general, these processes are shown for a diatomic molecule AB with the rotational number J_i, and vibrational number v_i and neutral colliding partner M. Electronically excited particles are denoted with an asterisk.

2.2.2. Neutral excitation and relaxation

The energy of electron impact collisions may be absorbed by the intermolecular degrees of freedom (rotational, vibrational and electronic) of heavy particles. These internal degrees of freedom consist of quantized energy levels. The absorbed energy elevates the energy level above the ground state into an excited state; this process is referred to as excitation. On the other hand, relaxation is the dissipation of energy as a result of interaction with other inter- or intramolecular degrees of freedom. Table 2.1 summarises the most relevant elementary excitation and relaxation processes.

Amongst the three excitation modes, *electronic excitation* requires the highest electron energy to excite. Table 2.1 describes the transition of an arbitrary atom A from the electronic ground state to the electronic excited state A^*. *Vibrational excitation* is generally regarded as the most important process in non-thermal discharges [7]. Vibrational excitation proceeds through the formation of an intermediate unstable negative ion and requires less energy to stimulate than electric excitation. Table 2.1 describes the transition of molecule AB from vibrational the lower vibrational level v_1 to the higher vibrational level v_2 through the intermediate formation of a negative ion AB^- with the vibrational level v_i. This is considered a resonant process. *Rotational excitation* can be resonant similar to vibrational excitation or nonresonant. Table 2.1 describes the nonresonant excitation of molecule AB from rotational number J_1 to rotational number J_2.

Vibrational-translational (VT) relaxation transfers the vibrational energy to the translational degree of freedom. Table 2.1 describes the collision between a vibrational excited molecule AB and ground state neutral M. The former de-excites as the energy is transferred to the kinetic energy of the colliding particles. The vibrational energy effectively is lost in heating up the gas. *Vibrational-vibrational (VV) relaxation*, transfers vibrational energy between vibrationally excited states. This populates the higher levels by transferring vibrational energy to higher levels. Table 2.1 describes the collision between two excited molecules AB with vibrational level v_1. As a results of VV relaxation one molecules excites to the higher vibrational level v_2 whilst the other de-excites.

Table 2.1: Elementary excitation and relaxation processes [7].

Process	Reaction
Electronic excitation	$e + \mathrm{A} \rightarrow \mathrm{A}^* + e$
Vibrational excitation	$e + \mathrm{AB}(v_1) \rightarrow \mathrm{AB}^-(v_i) \rightarrow \mathrm{AB}(v_2) + e$
Rotational excitation	$e + \mathrm{AB}(J_1) \rightarrow \mathrm{AB}(J_2) + e$
VT relaxation	$\mathrm{AB}(v_1) + \mathrm{M} \rightarrow \mathrm{AB} + \mathrm{M}$
VV relaxation	$\mathrm{AB}(v_1) + \mathrm{AB}(v_1) \rightarrow \mathrm{AB} + \mathrm{AB}(v_2)$

2.2.3. Ionisation

Ionisation is the primary mechanism for electron production. Generally, four main ionisation processes can be distinguished: ionisation by electron impact, stepwise ionisation, ionisation by heavy particle collision and photoionisation.

Direct ionisation by electron impact is ionisation of an unexcited atom or molecule as a result of a collision with an electron. This is predominantly present in non-thermal discharges where electron energies are high but the level of excitation of neutral species is relatively moderate [7]. Electrons need enough energy to exceed the ionisation potential, the energy threshold to liberate a bound electron, to ionise the unexcited neutral from the ground state. Direct ionisation may or may not result in the dissociation of a molecule. When the electron energy does not greatly exceed the ionisation potential, the collision results in a *non-dissociative ionisation* [7], however, when the electron temperature greatly exceed the ionisation potential, the collision may result in *dissociative ionisation*.

Stepwise ionisation is the ionisation of an excited particle and an electron. This ionisation process is relevant for discharges with a high ionisation degree and a high particle density, such as a thermal discharge [7]. Stepwise ionisation requires multiple steps to achieve ionisation. At first, electron-neutral collisions result in a highly excited neutral. Subsequently, a final collision with a relatively low energy electron results in the dissociation of the excited neutral.

Ionisation by heavy particle collision is the ionisation of unexcited or excited particle due to the collision with a heavy particle. Heavy particles are usually unable to provide the energy required for ionisation as a result of their low velocity [8]. When the electronic excitation energy of an excited heavy particle exceeds the ionisation potential of a ground particle, their collision can lead to ionisation, this process is referred to as *Penning ionisation*. When the combined energy is too low, *associative ionisation* can still occur. This results in an ionised molecule.

Photoionisation is the formation of an ion as a result of the interaction of a photon and an atom or molecule. The contribution of photoionisation to electron production is generally low, due to low concentration of high energy photons [8].

Table 2.2: Elementary ionisation processes [7].

Process	Reaction
Direct non-dissociative ionisation by electron impact	$e + AB \rightarrow AB^+ + e + e$
Direct dissociative ionisation by electron impact	$e + AB \rightarrow A + B^+ + e + e$
Stepwise ionisation by electron impact	$e + A \rightarrow A^* + e \rightarrow A^+ + e + e$
Penning ionisation	$A^* + B \rightarrow B^+ + e + A$
Associative ionisation	$A^* + B \rightarrow AB^+ + e$
Photoionisation	$h\omega + A \rightarrow A^+ + e$

2.2.4. Electron and ion recombination

While ionisation generates charged particles, the main mechanisms responsible for the destruction of charged particles are recombination, attachment and detachment.

The recombination of an ion and an electron is a highly exothermic process [7]. The excess energy released by the neutralisation of the charged particles is consumed by specific channels. With relatively low plasma densities the excess energy may be converted into radiation, although the cross section of *radiative electron-ion recombination* is not very high [11]. In high pressure discharges (above 1 atm) *three-body electron-ion recombination* is more common, the excess energy is channelled to the kinetic energy of the free electron [7].

Ion-ion recombinations between positively and negatively charged ions are dominant in low pressure plasmas with electronegative gases and can have very high rate coefficients [11]. The energy released by the collision excites a neutral product. In high pressure discharges, the *three-body ion-ion recombination* is more common.

In attachment processes, collisions between electron and neutrals may produce negative ions by attaching a free electron. *Dissociative electron attachment* is common in molecular gases. The electron attachment proceeds through the intermediate formation of an unstable excited ion which decays either by detachment of the free electron or by dissociation. *Three-body attachment* may occur in atomic gases at high pressure and low electron energies.

Detachment is the destruction of a negative ion with the release of a free electron. The three most-important detachments in plasma-chemical processes are electron impact detachment, associative detachment and detachment with excited species [7]. *Electron impact detachment* is important detachment mechanism in plasmas with high degrees of ionisation [7]. *Associative detachment* is especially important for non-thermal discharges with quite high rate coefficients [7]. In *detachment by excited particles collision*, detachment follows if the excitation energy of the neutral species exceeds the electron affinity of the negative ion, similar to Penning ionisation [11].

Table 2.3: Elementary recombination processes [7].

Process	Reaction
Dissociative electron-ion recombination	$e + AB^+ \rightarrow (AB)^* \rightarrow A + B^*$
Radiative electron-ion recombination	$e + A^+ \rightarrow A^* \rightarrow A + h\omega$
Three-body electron-ion recombination	$e + e + A^+ \rightarrow A^* + e$
Ion-ion recombination	$A^- + B^+ \rightarrow A + B^*$
Three-body ion-ion recombination	$A^- + B^+ + M \rightarrow A + B + M$
Dissociative electron attachment	$e + AB \rightarrow (AB^-)^* \rightarrow A + B^-$
Three-body electron attachment	$e + A + B \rightarrow A^- + B$
Electron impact detachment	$e + A^- \rightarrow A + e + e$
Associative detachment	$A^- + B \rightarrow (AB^-)^* \rightarrow AB + e$
Detachment with excited species	$A^- + B^* \rightarrow A + B + e$

2.3. Carbon dioxide dissociation

The highly stable CO_2 molecule requires a substantial amount of energy to dissociate due to the strong carbon-oxygen bonds. The dissociation of CO_2 starts with and is limited by the dissociation of an oxygen atom as described by [7],

$$CO_2 \rightarrow CO + O, \qquad \Delta H = 5.5 \text{ eV/molecule at 298 K, 1 atm} \tag{2.3}$$

The liberated oxygen atom either recombines with another free oxygen atom to form molecular oxygen or it reacts with another CO_2 molecule according [7],

$$O + CO_2 \rightarrow CO + O_2, \qquad \Delta H = 0.3 \text{ eV/molecule at 298 K, 1 atm} \tag{2.4}$$

This results in an overall highly endothermic process which can be described by [7],

$$CO_2 \rightarrow CO + \tfrac{1}{2}O_2, \qquad \Delta H = 2.9 \text{ eV/molecule at 298 K, 1 atm} \tag{2.5}$$

The equilibrium production of CO is depicted in figure 2.3. Without the removal of one of the products, the equilibrium of the reaction lies strongly to the left. Therefore, the production of CO is only thermodynamically favourable at very high temperatures.

Plasma-assisted CO_2 dissociation occurs through different dissociation channels. These dissociation channels are different mechanisms to transfer the electron energy to the CO_2 molecule. At least three major different channels occur, thermal decomposition, vibrational excitation and electronic excitation. The dissociation mechanism depends on the characteristics of the plasma. To understand the different discharge types the most important dissociation channels are briefly discussed. An extensive description of the CO_2 dissociation mechanisms can be found in the work of Fridman [7].

The exploited dissociation channel has a significant impact on the energy efficiency of the plasma chemical conversion. The energy efficiency is a measure of the effectiveness of the conversion in comparison to the reaction enthalpy.

$$\eta = \Delta H / E_{CO} \tag{2.6}$$

here ΔH is the dissociation enthalpy of 2.9 eV/molecule and E_{CO} the actual energy cost per molecule of CO produced.

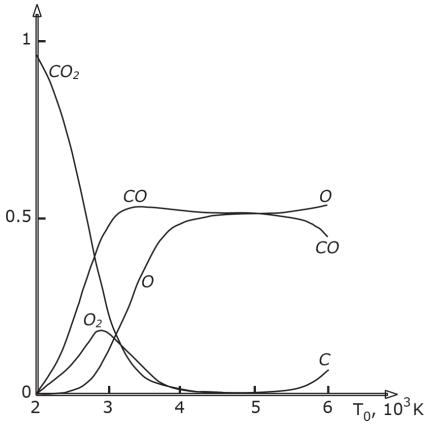

Figure 2.3: Thermal equilibrium of CO_2 dissociation [7]

2.3.1. Thermal decomposition

Thermal decomposition is the predominant process under LTE conditions. Under these conditions the plasma shifts the chemical equilibrium in favour of product formation by thermal heating. Thermal heating distributes the energy over all degrees of freedom uniformly. This limits the conversion and energy efficiency of the process since only a few degrees of freedom are relevant to dissociation. As a result, the maximum energy efficiency is only 43 % [7]. Moreover, as temperature decreases the chemical equilibrium is continuously sustained, which reverts the products back into CO_2. The decomposition products can only be preserved by quenching with very fast cooling rates in the order of $10^7 - 10^8$ Ks^{-1} [7]. To achieve higher rates of energy efficiency and to overcome the limitations of thermal decomposition, different temperatures for the relevant degrees of freedom and different species are required. These temperature variations are achievable under non-thermal equilibrium conditions only.

2.3.2. Vibrational excitation

As a result of the temperature distribution in non-thermal plasmas, it is possible to transfer the discharge energy specifically to the channels relevant for dissociation whilst the gas temperature remains low. The low gas temperature renders quenching unnecessary due to the low reaction rate of the reverse reaction. Figure 2.4 depicts the fraction of discharge energy transferred to the different excitation channels of the CO_2 molecule as a function of the reduced electric field (E/n_0). The reduced electric field is the ratio of the electric field over the neutral gas density. As figure 2.4 illustrates, the reduced electric field has a profound effect on the distribution of the electron energy over the different excitation channels.

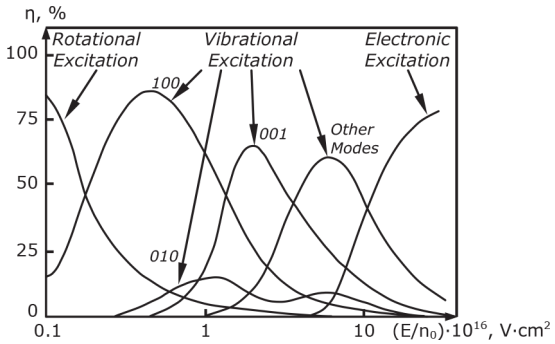

Figure 2.4: Fraction of the discharge energy transferred to different excitation channels of the CO_2 molecule as a function of the reduced electric field (E/n_0) [7]

Prior studies have shown that the most efficient dissociation pathway is based on the vibrational excitation of the CO_2 molecule by electron impact [5, 7]. In addition, Fridman reports that no less than 95% of discharge energy can be transferred to the vibrational excitation of the molecule at electron temperature of

1-2 eV [7]. Although electrons are able to dissociate CO_2 directly from the ground ($^1\Sigma^+$) according,

$$CO_2^*(^1\Sigma^+) \rightarrow CO(^1\Sigma^+) + O(^1D) \tag{2.7}$$

the formation of the excited oxygen atom $O(^1D)$ raises the activation energy to 7 eV/mol [7]. Contrary, stepwise vibrational excitation has a much lower activation energy and as a result it proceeds exponentially faster [7]. This non-direct, multi-step process is initiated by the vibrational excitation of the lowest vibrational levels induced by electron impact. Subsequent vibrational-vibrational collisions gradually populate the higher vibrational levels of the CO_2 molecule. The overall process is described by,

$$CO_2^*(^1\Sigma^+) \rightarrow CO_2^*(^3B_2) \rightarrow CO(^1\Sigma^+) + O(^3P) \tag{2.8}$$

This dissociation process results in the formation of an oxygen atom in the ground state (^3P), this oxygen atom is able to produce another CO according reaction 2.4. The activation energy of vibrational dissociation equals the carbon-oxygen bond strength of 5.5 eV/molecule [7] in the dissociation of the CO_2 molecule.

2.3.3. Electronic excitation

In non-thermal discharges with high values of reduced electric field, typically at low pressure, vibrational excitation is suppressed and electronic excitation becomes the dominant CO_2 dissociation mechanism [11]. This one-step process results in the formation of an electronically excited CO molecule ($a^3\Pi$) [11] according to,

$$e + CO_2^*(^1\Sigma^+) \rightarrow CO(a^3\Pi) + O(^3P) \tag{2.9}$$

The energy of the electron exceeds 14 eV/mol for dissociation to occur, which significantly exceeds the carbon-oxygen bond strength [11]. Besides the electronic excitation of CO_2, numerous irrelevant and ineffective states of the molecule are excited due to the high electron temperatures to achieve a significant contribution towards dissociation. Electronic excitation and the subsequent radiative de-excitation of a neutral particle is a good illustration of an irrelevant process. Consequently the energy efficiency of dissociation by electronic excitation is severely limited, at maximum an energy efficiency of 25 % can be achieved [7].

2.4. Electric discharges

Plasma is commonly generated and maintained through an electrical discharge. The simplest configuration to generate a plasma through electric discharge is by applying a high voltage across two parallel flat electrodes. As the voltage applied across two electrodes exceeds the breakdown voltage, a dielectric breakdown instigates. Primary electrons, which are occasionally generated near the cathode (negative electrode), drift towards the anode (positive electrode). Accelerated by the electromagnetic field, the primary electron collides with other gaseous molecules, liberating their electrons in turn. These additional liberated electrons induce an electron avalanche, generally referred to as a Townsend breakdown (Figure 2.5), which ultimately results into a plasma.

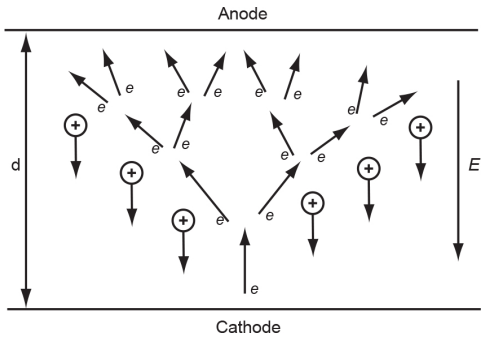

Figure 2.5: Townsend breakdown in a gap, this breakdown is an ionisation process where free electrons are accelerated by the electromagnetic field and collide with gaseous molecules. Additional electrons are liberated from the gaseous molecules upon collision, this results in an electron avalanche. Adopted from [7]

Figure 2.6 depicts the voltage-current characteristics of a low pressure direct current (DC) discharge. Three distinct discharge regimes can be recognised from each other, the dark discharge, the glow discharge

and the arc discharge. As the voltage increases, the plasma transits from an invisible dark discharge, to a faint glow discharge and finally to a luminous thermal arc discharge. The following section briefly describes the glow and arc discharge regime. For a detailed description of the discharge characteristics the reader is referred to the respective literature [7–9].

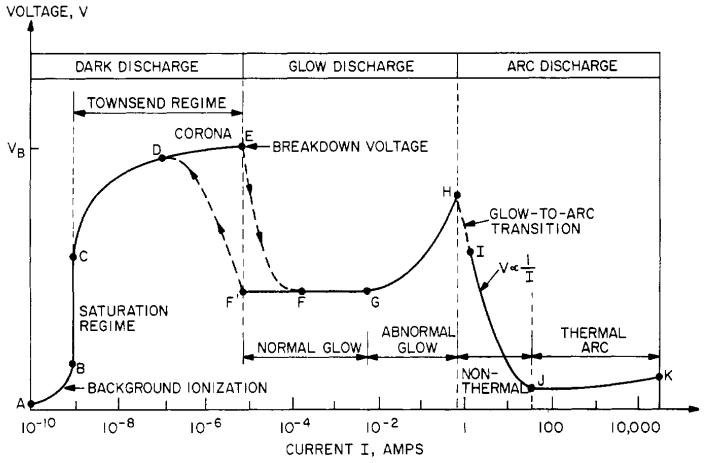

Figure 2.6: DC gas discharge V-I characteristics: point A-J describe various critical phases and tipping points of the discharge, ranging from background ionisation to a thermal arc; adopted from [9]

Once the voltage exceeds the breakdown voltage V_B, the discharge transitions into a self-sustained continuous glow discharge. The glow discharge is a diffuse discharge, with sufficient electron energy and number density to generate visible light by excitation collisions. The discharge is sustained by secondary electron emissions from the cathode induced by ion impact. A low pressure gas discharge features a characteristic appearance as depicted in figure 2.7. The reader is referred to the respective literature for a detailed description on the different regions [9]. As the current density increases the cathode becomes hot enough to emit electrons by thermionic emission and the glow discharge transitions towards a thermal arc discharge. Arc discharges are characterised by high luminosity, high current and high current density. The most basic configuration is the free-burning, linear arc as illustrated in figure 2.8 in a horizontal configuration. In this configuration, the arc bows upward due to the buoyancy of the hot gases.

In general, the different mechanisms and conditions supported by the various discharge types have a significant impact on the plasma parameters. The discharge configurations can be classified according to a number of features. Most importantly, the operating pressure (atmospheric or reduced), operating current (AC, DC or pulsed), power coupling (electrodes or electromagnetic radiation) and thermal equilibrium (LTE or non-LTE). There are numerous configurations with many different applications.

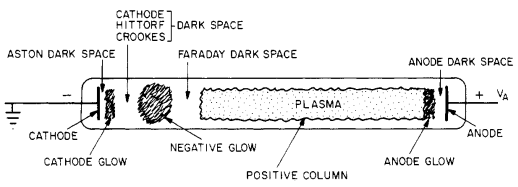

Figure 2.7: Schematic representation of the characteristic regions of the glow discharge; adopted from [9].

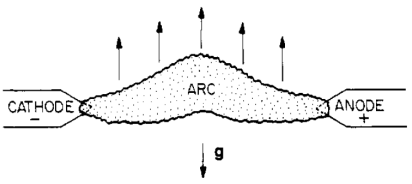

Figure 2.8: Schematic representation of the free-burning horizontal arc discharge; adopted from [9].

The most common discharge configuration used to dissociate CO_2 are the gliding arc (GA) discharge, dielectric barrier discharge (DBD) and microwave (MW) discharge [5]. To a lesser extend, radio frequency (RF), atmospheric glow discharges, corona discharge and nanosecond pulsed discharges have been used [5]. The most important discharge configurations for plasma-assisted CO_2 dissociation will be described below. The reader is referred to the respective literature for a detailed description of these and other discharge configurations [7, 8, 12–14].

2.4.1. Gliding arc (GA) discharge

A GA discharge is an auto-oscillating periodic discharge. At high currents, it generally evolves from an arc to a non-equilibrium discharge in one cycle. The classical GA configuration consists of two flat diverging electrodes submerged in a gas flow as illustrated in figure 2.9(c). When a potential difference is applied on the two electrodes, a plasma column ignites upstream at the narrowest gap. The gas drags the plasma column downstream along the diverging electrodes. The plasma column elongates as the interelectrode gap increases until it reaches a critical length. At this critical length, heat losses exceed the energy supplied to the plasma and the plasma is unable to sustain its LTE state. This accumulates in a fast transition towards a non-LTE state. The plasma column continues until the length attains a new critical value and decays. Afterwards the evolution of the plasma column repeats as it reignites at the narrowest gap. In this cycle, 75-80 % of the energy can be dissipated in the non-LTE regime.

Despite this high dissipation rate, the flat configuration limits the gas conversion as only a fraction of the gas passes through the plasma[5]. In addition, the non-uniformity of the discharge in time and space gives rise to an in-homogeneous distribution of energy and active species which further limits the efficiency [5, 15]. Various configurations have been developed to address these disadvantages by plasma stabilisation. This stabilisation can be achieved by a reverse vortex in a so-called gliding arc plasmatron (GAP) [16], by magnetic confinement [17] or mechanical rotation [15].

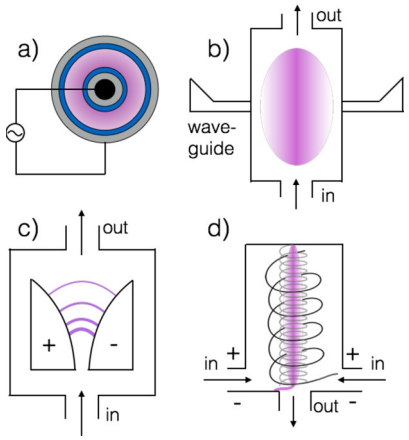

Figure 2.9: Schematic representation of the most common discharge configurations: (a) DBD, (b) MW discharge, (c) GA discharge, (d) GAP [18].

2.4.2. Dielectric barrier discharge (DBD)

DBD configurations consist of two parallel electrodes and at least one dielectric barrier between the electrodes, which restricts the electric current. This dielectric barrier restricts the electric current which prevents spark formation and retains the plasma in a non-LTE state [7]. Instead, the plasma formation is limited to a filamentary mode as shown in figure 2.10, where the discharge occurs in numerous tiny individual breakdown channels, referred to as micro-discharges [8]. The micro-discharges terminate within several nanoseconds due to a reduction in the local electric field as a result of charge accumulation in the dielectric barrier [8]. The short duration of the discharge prevents the streamer channel from overheating and therefore the plasma remains strongly non-thermal [8].

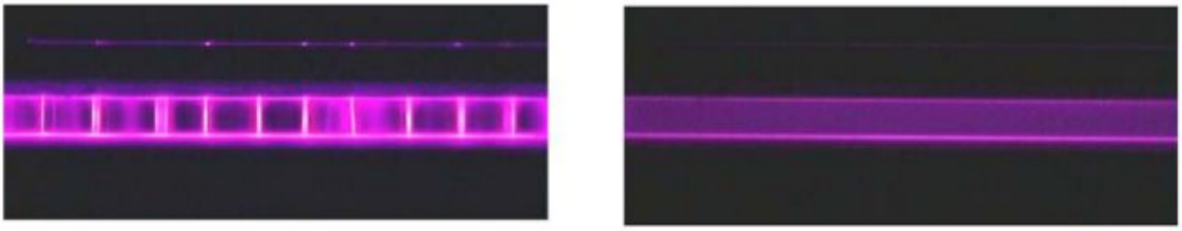

Figure 2.10: Different modes of a non-thermal discharge, on the left a filamentary discharge, on the right a diffuse, homogeneous discharge, adopted from [19]

In gas conversion, concentric metal electrodes as depicted in 2.9(a) are commonly used instead of parallel plates. The interelectrode gap typically ranges from 0.1 to 10 mm [20]. DBDs usually operate at atmospheric pressure. The electrodes are supplied with alternating current (AC) or pulsed power at frequencies between 0.5 and 500 kHz [8]. The material for the dielectric barrier is typically glass, quartz, ceramics, enamel, mica, plastics, silicon rubber or teflon [20].

2.4.3. Microwave (MW) and radio frequency (RF) discharges

A MW discharge is a discharge where the plasma is sustained by electromagnetic microwaves instead of electrodes. MW discharges can be created both at reduced and at atmospheric pressure. The microwaves can be coupled to the plasma in different configurations. The most typical configuration for CO_2 dissociation, the surface-wave discharge, couples the waves with rectangular wave guides to a dielectric discharge tube (figure 2.9(b))[5]. This discharge tube is transparent to microwave radiation and so, within this tube the plasma is ignited and maintained. The microwaves are conducted parallel to the surface of the dielectric tube walls [12]. The waves propagate near the interface where the wave energy is absorbed by the electrons [12]. The heated electron diffuse in the bulk which results in a high density plasma at reasonable absorbed power [5].

RF discharges are similar to microwave discharges with typical frequencies of 1 to 100 MHz, the corresponding wavelength is much larger than the system [5]. The power can be coupled inductively or capacitively to the plasma. In an inductively coupled plasma, the plasma chamber is surrounded by a coil whereas in a capacitively coupled plasma, power is supplied by two parallel plates [12].

2.4.4. Other discharges

Other discharge types occasionally applied apart from the three previously discussed are atmospheric pressure glow discharges, corona discharges, spark discharges and nanosecond pulsed discharges. Atmospheric pressure glow discharges are able to operate in the absence of vacuum, without elevated temperatures. Miniaturised devices prevent the heating of the cathode and the transition towards an arc discharge. The discharge is strongly related to DBDs and can be operated in a filamentary or a dilute mode [5]. Corona discharges form near sharp points, edges or wires. The discharge devices usually consist of a cathode wire and an anode connected to a pulsed DC power supply. The power supply is pulsed to increase power without the transition of streamers into sparks [5]. In spark discharges the absence of the pulsed power supply develops the streamer channels in a spark. These high energy sparks extinguish and reignite periodically without developing in thermal arcs. Nanosecond pulsed discharges are repetitively pulsed excitations which generates a glow-like discharge. The discharge has a high plasma density for a relatively low power consumption.

2.5. Current state of technology

The dissociation of CO_2 has been intensively investigated in numerous thermal and non-thermal systems for over 40 years. The developments made were extensively reviewed by Snoeckx and Bogaerts (2017). The following is a brief description of their work supplemented with the most recent advances in the field.

The dissociation of CO_2 is a simple chemical process with little concern for selectivity due to small variety of products that can be formed. Therefor, the primary focus of research has been on the improvement of the energy efficiency, as described by equation 2.6, and the conversion of the process. In general, the absolute conversion $\chi_{\text{abs},i}$ of component i is defined as [5],

$$\chi_{\text{abs},i} = \frac{\dot{n}_{\text{in},i} - \dot{n}_{\text{out},i}}{\dot{n}_{\text{in},i}} \tag{2.10}$$

where $\dot{n}_i$ is the molar flow rate of component i. Some researches have added admixture gases to ignite the plasma more easily, such as Ar, N_2 and He. The effective conversion takes the dilution of the mixture into account which is important for comparing CO_2 dissociation in different mixtures. The effective conversion $\chi_{\text{eff},i}$ is defined as [5],

$$\chi_{\text{eff},i} = \chi_{\text{abs},i} \frac{\dot{n}_{\text{in},i}}{\sum_i \dot{n}_{\text{in},i}} \tag{2.11}$$

In order for plasma technology to be competitive with electrolysis, Snoeckx and Bogaerts have set an energy efficiency target of 60 % [5]. This energy efficiency target is a minimum, based on the achieved energy efficiencies of 65-75% for commercial electrochemical water splitting [5]. This objective exceeds the energy efficiency of the thermal equilibrium; therefore, most research has been focused on non-thermal discharges, especially on the exploitation of the vibrational excitation channel.

As mentioned previously, most research on the plasmachemical conversion of CO_2 has been performed with non-thermal GA, DBD, and MW plasmas. Additionally, other plasma types have been used to a lesser extend. Figure 2.11 compares the energy efficiency as a function of the conversion of the various plasma types reviewed by Snoecks and Bogaerts and puts this into relation with the thermal equilibrium and the set efficiency target.

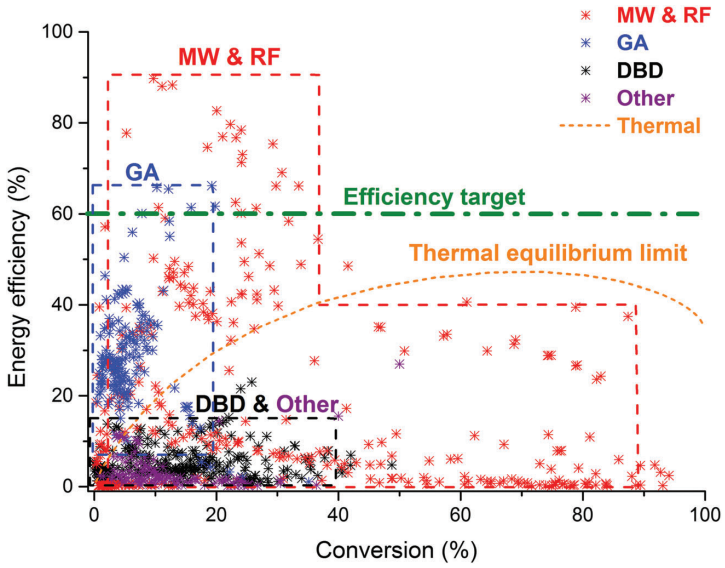

Figure 2.11: Energy efficiency (as defined by Equation 2.6) as function of the conversion for different plasma types; adopted from [5]

What can be clearly seen in Figure 2.11 is a limitation for every discharge configuration in either the conversion or energy efficiency whereby the optimisation of one is often at the expense of the other. It is well known that the specific energy input (SEI), defined as the electrical power P divided by the volumetric gas flow rate $\dot{V}$ [5],

$$\text{SEI} = \frac{P}{\dot{V}_i} \tag{2.12}$$

is the dominant factor governing the conversion and energy efficiency. In general, an increase in the SEI increases the conversion and on the other hand decreases the energy efficiency. This could be explained by the increase in collision frequency due to the high electron density at high values of SEI, which in turn drives the conversion upward. However, since the SEI exceeds the CO_2 bond strength, the surplus energy is effectively wasted resulting in a low energy efficiency.

Figure 2.12 presents the experimental data collected from literature by Snoeckx and Bogaerts for CO_2 dissociation in DBD plasmas. It is evident that most experimental results are situated below an energy efficiency of 15 % and a conversion of 40 %. The highest conversion of 53.7 % was achieved with a packed-bed DBD [21] whereas the highest energy efficiency of 23 % was obtained with a pulsed power DBD [5]. Modelling has shown that DBDs mainly dissociate CO_2 by electron impact and that vibrational excitation is of minor importance [22].

The experimental data on MW and RF plasmas collected from literature by Snoeckx and Bogaerts is presented in figure 2.13. The combination of a high electron density and low reduced electric field favours the vibrations excitation of CO_2 which results in high energy efficiency. The highest energy efficiency reported was up to 80 % in subsonic flow conditions and up to 90 % for supersonic flow. However, these results were reported in the 1970-1980s at reduced pressures and recent studies have not been able to achieve energy efficiencies above 50 %. Conversions of up to 95 % have been achieved with energy efficiencies in the range of 10 to 50 % albeit at low pressure (20-50 Torr) [5]. It has been shown that increasing the pressure severely decreases the energy efficiency [5]. Additionally, the pressure determines to a large degree whether the discharge operates in a contracted, diffuse or combined mode [5].

Figure 2.14 contains the experimental data on GA plasmas collected from literature by Snoeckx and Bogaerts. GA plasmas are able to operate at atmospheric pressure similar to DBD. Unlike DBD plamas, GA discharges are able to stimulate the most energy efficient dissociation channel. This is evident from the experimental data where the the majority of the experiments report a maximum energy efficiency of 40-50 %

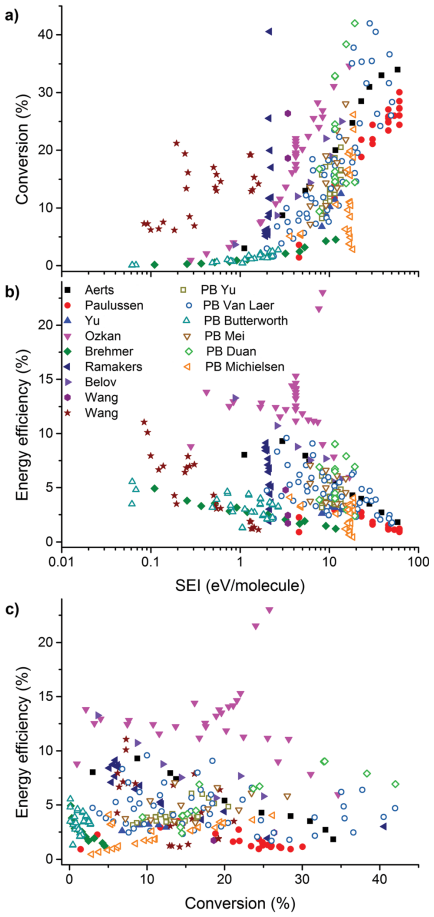

Figure 2.12: Experimental results for CO_2 dissociation in DBD plasmas of Aerts [22], Paulussen [23], Yu [24], Ozkan [25], Brehmer [26], Belov [27], Wang [28], Wang [29], Van Laer [30], Butterworth [31], Mei [32], Duan [33] and Michielsen [34] adapted from [5].

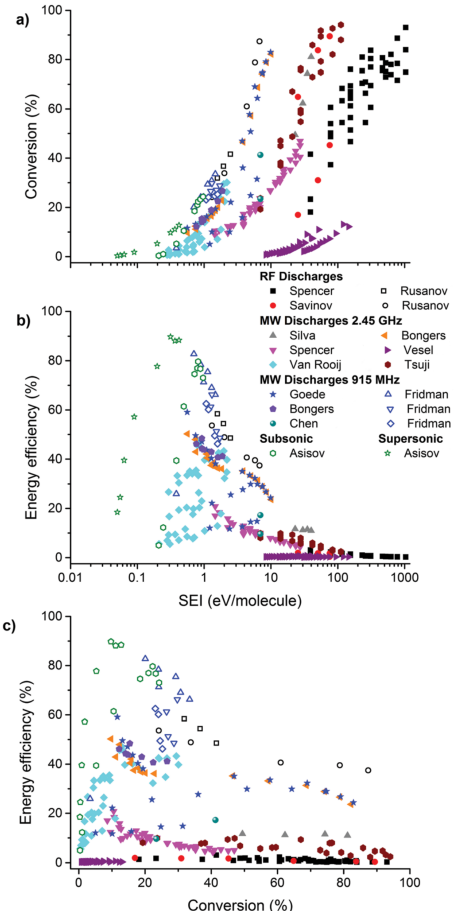

Figure 2.13: Experimental results for CO_2 dissociation in MW plasmas of Spencer [35], Savinov [36], Rusanov [37], Silva [38], Spencer [39], Van Rooij [40], Bongers [41], Vesel [42], Tsuji [43], Goede [44], Chen [45], Fridman [7] and Asisov [46], adapted from [5].

[5]. The highest reported energy efficiency is about 65 % [5]. However the conversion remains mostly below 15 % with the exception of the work of Indarto et al [47] where the mixture was diluted with N_2. As discussed previously, the geometry and non-uniformity of the discharge limits the conversion in a GA discharge.

Lastly, experimental data on the other discharge configurations are given in figure 2.15. It is apparent that the majority of the results are situated below a maximum conversion of 40 % and a maximum energy efficiency of 15 %. The notable exception is the work of Andreev et al on a non-self sustained discharge which achieved a conversion of 50 % with an energy efficiency of 30 %. This was achieved by operating at a reduced electric field of 20 Td (10^{-17} V cm^2) which favours the vibrational excitation channel.

Recent research has been focused on optimising the conditions in the various plasma types to achieve higher energy efficiency and conversion. Aside from the applied power and gas flow rate which are directly correlated to the SEI, research has been conducted on changing the reactor geometry, reactor temperature, admixtures, flow type and packing materials [5]. Data from several studies suggest that the reactor geometry plays an important role on the discharge behaviour and consequently the conversion. Aerts et al. [22] observed that increasing the discharge gap in DBDs can lead to less streamer formation and as a consequence a significant decrease in the conversion. A similar effect has been observed in regular GAs. Here, an increase in the interelectrode gap increases the arc volume which lowers the electron density and as a consequence a drop in the conversion [52].

Interestingly, the effect of the reactor temperature in DBD and MW plasmas is ambiguous, whereas in conventional chemical conversion it is one of the most important governing parameters [5]. In MW the desired situation consists of a low gas temperature with high vibrational and electron temperatures. Gas tempera-

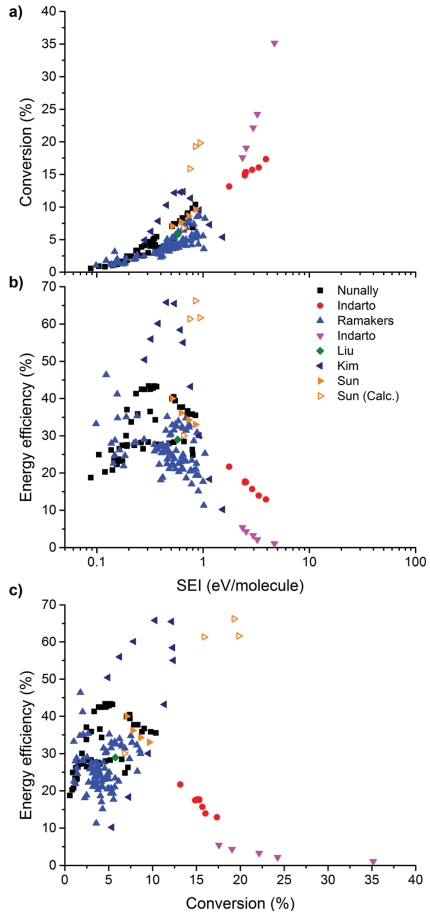

Figure 2.14: Experimental results for CO_2 dissociation in GA plasmas of Nunally [16], Indarto [48], Ramakers [49], Indarto [47], Liu [50], Kim [51] and Sun [52], adapted from [5].

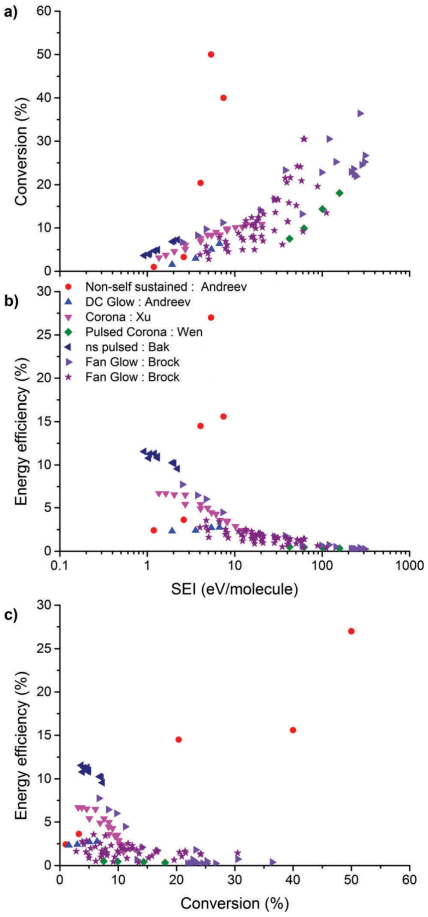

Figure 2.15: Experimental results for CO_2 dissociation in other plasma configurations of Andreev [53], Xu [54], Wen [55], Bak [56] and Brock [57], adapted from [5].

tures around 2000 K have been observed at low pressures and reduced electric fields but rise steeply to 14000 K as a transition occurs from a diffuse to a contracted regime as pressure increases [40]. Recent modelling studies suggest that gas temperature should remain low to reduce energy losses via VT relaxation [58]. In a similar way, the reduction of the arc temperature in GA discharges can result in higher conversion and energy efficiency. Modelling studies suggest a lower arc temperature limits the recombination of CO and O atoms [52].

The addition of inert admixture gases such as Ar, N_2 or He generally allows for easier ignitable mixtures but is not necessarily more energy efficient [5]. Studies on the addition of Ar and He have shown an increase in the absolute conversion of CO_2, but dilution causes a decrease in the effective conversion and as a result a lower energy efficiency in both DBD [59] and MW discharges [11]. In contrast, the addition of N_2 is able to increase the effective conversion of CO_2 in MW [60], however at the cost of unwanted by-product formation of N_2O and several NO_x compounds. On the contrary, in DBD plasmas the addition of N_2 has almost no influence on the effective conversion [61] and in GA discharges the addition has a detrimental effect on the energy efficiency [47].

The longer residence times as a result of the reverse vortex flow allow the GAP to improve the conversion by a factor of 2 over the regular GA configuration [5]. The GAP illustrates the improvements that can be made by adjusting the flow type. A similar approach has been applied to MW discharges, where improved performance has been observed at similar values of SEI for reverse flow configurations [41].

This section has reviewed the current state of technology with respect to plasma-based CO_2 dissociation. It is clear that amongst the three major discharge configurations MW plasmas have shown the widest variety of performance. On one hand, MW plasmas easily exceed the energy efficiency target with conversions up to 40 % [5]. This demonstrates their ability to exploit the vibrational excitation channel. However, this can

only be achieved at low pressure, which makes it less attractive for industrial applications. On the other hand MW plasmas have been able to high conversion rates albeit at lower energy efficiency. It is likely that in this situation MW operate in the thermal regime to achieve high conversion rates.

In contrast to MW plasmas, GA plasmas have been able to exploit the vibrational excitation channel at atmospheric pressure. However, GAs are hampered by their limited gas conversion rates. This is illustrated by their performance, where GAs have been able to surpass the energy efficiency target but conversion rates remain below 20 % [5].

Despite the fact that DBDs have been extensively studied, their performance does not justify their use. Despite the ability to work at atmospheric pressure, DBDs are unable to exploit the vibrational excitation channel. Consequently, the energy efficiency remains too low and conversion rates are similar to GA plasmas.

In summary, none of the three major discharge configurations have been able to exploit the vibrational excitation channel at atmospheric pressure with acceptable conversion rates. Therefore, for CO_2 dissociation new configurations should be explored in order to keep plasma-assisted fuel synthesis a viable option [6].

3

Materials and methods

The main purpose of this thesis is to establish the relationship between conditions of the plasma inside the rotating reactor-electrode assembly and CO_2 dissociation reaction performance, the latter being defined by conversion and energy efficiency. The conditions of the plasma are described by plasma parameters, such as the electron temperature. Therefore, at first the relationship between the system variables and plasma parameters needs to be established. The system variables employed were pressure, applied electric power, rotational speed and gas feed rate.

In order to understand the relation between plasma parameters and system variables, the plasma was investigated in a first round of experiments with a non-reactive species, argon. As a non-reactive species, argon is solely able to ionise and not dissociate. This allows to specifically observe the relationship between the plasma parameters and the system variables, without the complexity added by dissociation processes.

Based on this knowledge, the relationship between plasma conditions and CO_2 dissociation reaction performance could be investigated in a second set of experiments. By manipulating the system variables, for which the effects on the plasma are now known, the plasma conditions could be related to the reactor performance.

This chapter describes the set-up, diagnostic tools and procedures used to perform the experiments described above. The chapter continues with describing the analytical methods used to interpret the experimental results. The last section lists the modifcations made to the original design of the reactor.

3.1. Experimental setup

A schematic representation of the experimental setup is shown in Figure 3.4. The experimental setup consisted of a SAPR prototype connected to a custom built 2 kW high voltage power supply, with feed lines for argon and CO_2, a downstream pump and a vent line. The entire setup was accommodated in a fume hood for safety considerations, with feed lines running in and the vent line briefly passing outside of the fume hood to provide a sample point.

The feed lines for both argon and CO_2 contained open-close ball valve HV01A/B, pressure control valve PCV01A/B to regulate the feed pressure and needle valve HV02A/B to regulate the feed flow rate. Both streams tied in the manifold block of the plasma reactor through hose H01A/B. A flow meter (F-101D,Bronkhorst) was included in the CO_2 feed to measure the flow rate in the feed line.

Hose H03 was tied in the other reactor manifold to collect the reaction effluent. To regulate the operating pressure in the system, vacuum pump P03 (SC920, KNF) was connected downstream. The effluent was subsequently vented to a safe location. A port in the vent line allowed for sampling of the reactor effluent to be analysed by an off-stream gas chromatograph (CP4900, Varian Analytical; CP-molesieve 5A agilent; Ar; Poraplot U agilent; He; $1-10\mu$L). The stream was sampled in 0.6L Tedlar Push Lock Valve Bags by shortly rerouting the effluent stream, opening valve HV05 and closing valve HV04.

The emission light of the plasma was transmitted by an optical fibre cable and analysed by a spectrometer (MAYA2000, Ocean Optics). The behaviour of the plasma was visually captured using a digital camera (D7000, NIKON) with a zoom lens (18-200mm AF-S DX f3.5-f5.6G ED VRII, NIKON).

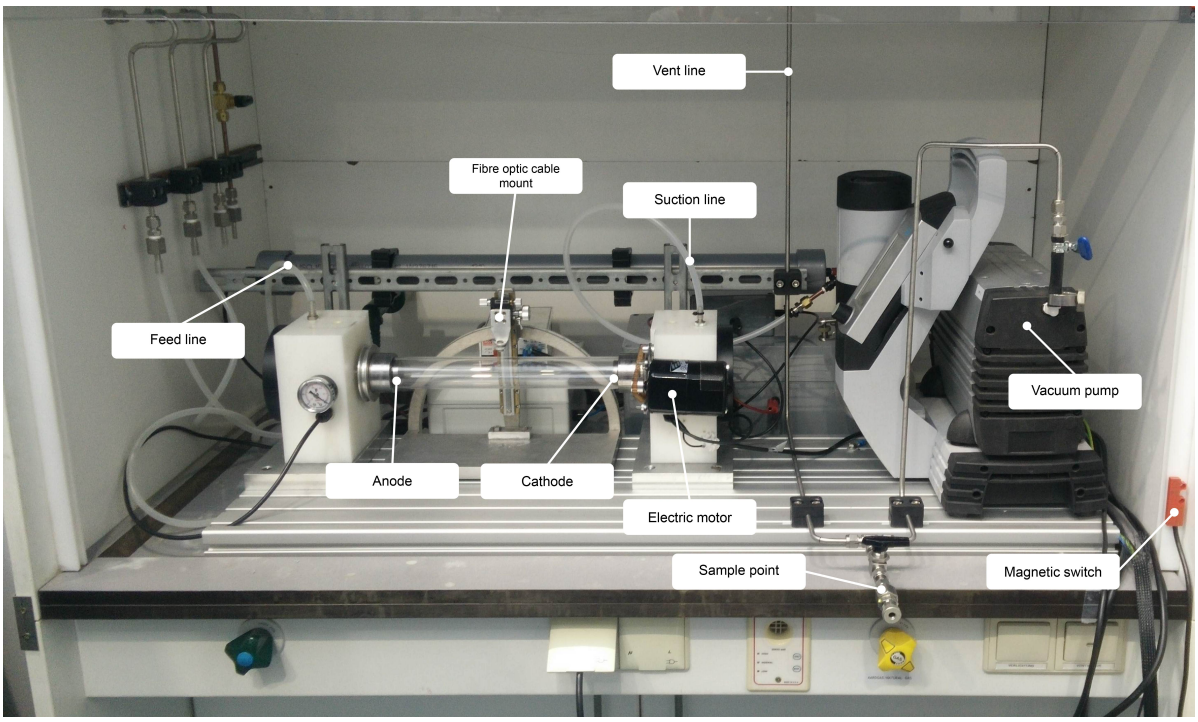

Figure 3.1: Overview of the experimental setup, highlighting the most important equipment.

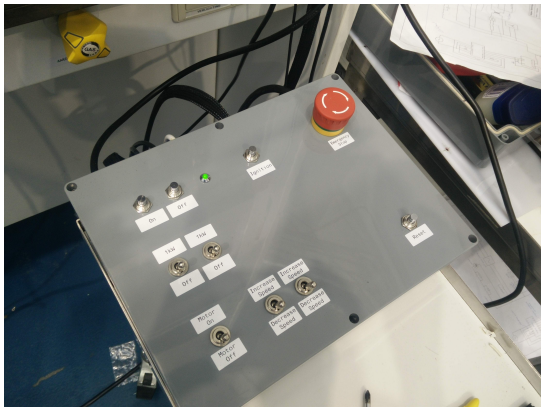

Figure 3.2: Close-up of control panel

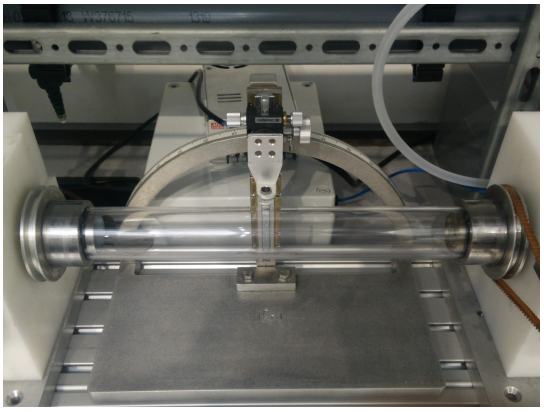

Figure 3.3: Close-up of reactor-electrode assembly

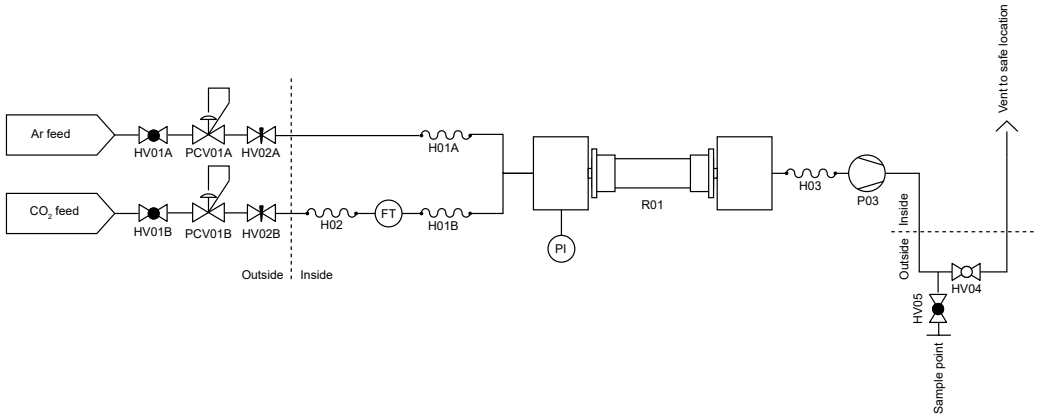

Figure 3.4: Schematic representation of the SAPR experimental setup.

3.1.1. Power electronics

Figure 3.5 presents a simplified schematic representation of the high voltage power supply. The high voltage power supply system consisted of transformer T1 and full-bridge rectifier circuit D1 to D4, increasing the input voltage from 230V single phase AC to 2kV DC. An electric heater (HZ110, Honeywell) was used as the electric load. More specifically, the two heating coils R1 and R2 of the electric heater were used as two parallel electric loads.

Power to the reactor was regulated with a control panel, a detailed wiring diagram can be found in appendix B. The control panel regulates: the electric motor, the fan of the electric heater, and the heating coils of the electric heater and therefore the plasma reactor.

As a safety measure, the control panel should cut power to the plasma reactor R3 when the fume hood sash is open. A magnetic switch, installed on the fume hood sash, was monitored by the safety relay inside the control panel. During operation, the fume hood sash is closed with the face opening kept to a minimum. The safety relay cuts power to the plasma reactor when the normally closed magnetic switch disconnects upon opening the sash. In an emergency, the safety relay can cut the power to the plasma reactor by pressing the emergency button.

Upon engaging power to the plasma reactor the safety relay requires a reset. When the sash is closed the control panel can be switched on by pressing the on-button. By switching on the control panel the fan of the electric heater is powered. The electric motor can be switched on and set to required speed level. Each 1 kW heating coil of the electric heater can be switched on with switch S1 or switch S2, powering the plasma reactor as described previously.

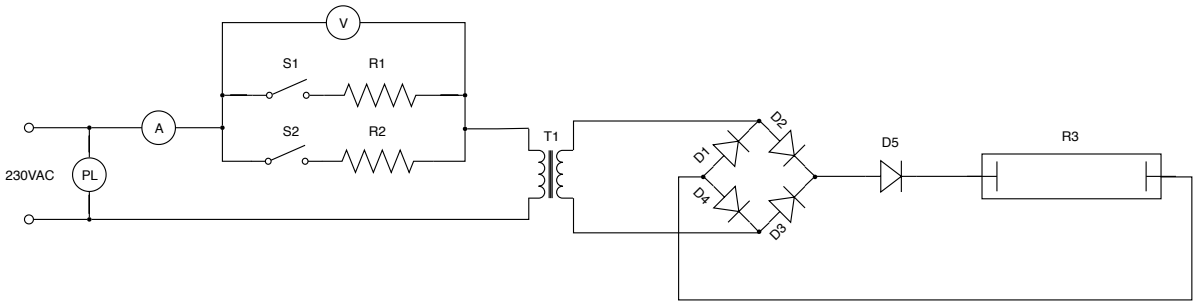

Figure 3.5: Simplified schematic representation of the power supply to the plasma reactor

3.1.2. Spinning arc plasma reactor

In the centre of the SAPR stands the reactor-electrode assembly (Figure 3.6), which accommodates the plasma-assisted reaction. The reactor-electrode assembly consists of a hollow transparent quartz cylinder of about 40 mm in diameter and 300 mm in length (03). On the left and right ends respectively, the cylinder is supported by the anode-service assembly (01) and cathode-service assembly (05). The service assemblies accommodate the anode (02) and the cathode (04) and allow the cylindrical vessel to rotate about its own axis. The axis of the service assembly is a hollow shaft, which allows the gas run through the reactor-electrode assembly. The two electrodes, made of stainless steel disks, extend into the interior of the cylinder and maintain a rotational fixed relation with the cylinder.

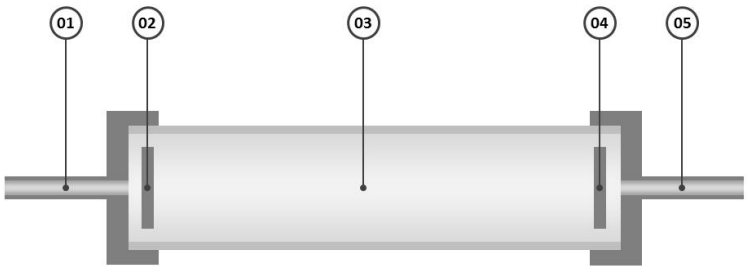

Figure 3.6: Reactor-electrode assembly: (01) anode-service assembly, (02) anode, (03) reactor vessel, (04) cathode, (05) cathode-service assembly.

The discharge is sustained within the interior of the reactor vessel and stabilises due to rotation. A gaseous, ionisable medium enters the interior of the vessel through the anode-service assembly. Reaction effluent is discharged on the other side through the cathode-service assembly.

Figure 3.7 represents the whole SAPR reactor. The reactor-electrode assembly is supported by polyoxymethylene (POM) manifold blocks (01) on both ends. The manifold blocks distribute power and gas to the reactor-electrode assembly and accommodates the electrical motor (05). The 180 W motor (HN-180) has a maximum rotational speed of 10.000 rpm. The reactor-electrode assembly is connected to the motor by a drive belt (04).

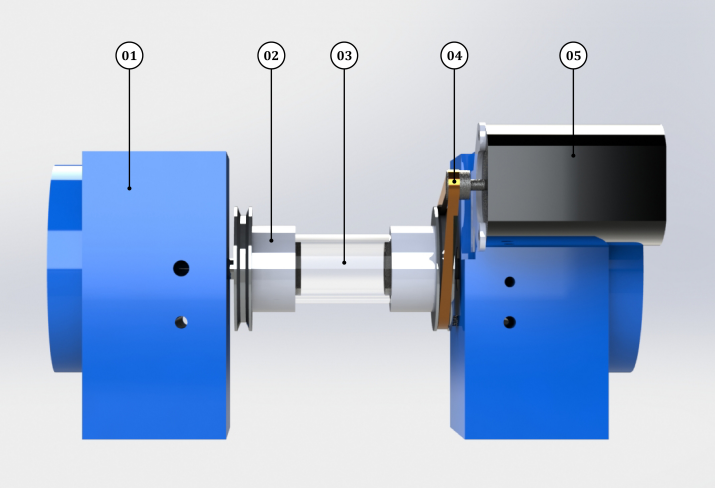

Figure 3.7: Spinning arc plasma reactor: (01) manifold, (02) service assembly, (03) reactor vessel, (04) drive belt, (05) motor.

The cross-section of Figure 3.7 is shown in Figure 3.8. Both the anode and cathode manifold accommodate a vacuum chamber (06). Gas enters the vacuum chamber through the inlet channel on top of the anode-manifold (01) and exits the cathode vacuum chamber through an identical effluent channel, running through the reactor-electrode assembly (03) as described previously in 3.6. The axes of the rotating reactor-electrode assembly are supported by the manifold blocks with bearings (05) on either side of the lubrication channel (02). Lubricant oil is inserted through the lubricant channel to reduce the surface friction between the axis and the manifold (02). The lubrication channel and vacuum chamber are operated at different pressures. Therefore, an oil seal is present between the lubrication channel and the bearings to prevent the oil from leaking into the vacuum chamber. A carbon block (04) is positioned in both manifolds to conduct the electrical current.

3.2. Diagnostics

Several diagnostic tools were employed to determine the CO_2 reactor performance. Outlined below are, optical emission spectroscopy was employed to determine the condition of the plasma. Each of these will be described below.

3.2.1. Reactor performance measurements

The conversion of CO_2 was determined with samples analysed by the gas chromatograph. The energy efficiency requires knowledge on the power dissipated in the plasma, the conversion of CO_2 and the CO_2 flow rate. This flow rate was determined by the feed line flow meter. The dissipated power was measured by a combination of several diagnostic tools to prevent the usage of high voltage diagnostic tools. The total consumed power was measured with an electricity meter (Energy Logger 3500, Voltcraft). Furthermore, the current and voltage over the electric heater was measured with a clamp meter (ST-337, Standard) and a digital multimeter (VC 840, Voltcraft), respectively. Based on the knowledge of the total consumed power and the power consumed by the electric load, the power dissipated in the plasma can be determined. This assumes that all electrical resistance is encountered in the plasma itself.

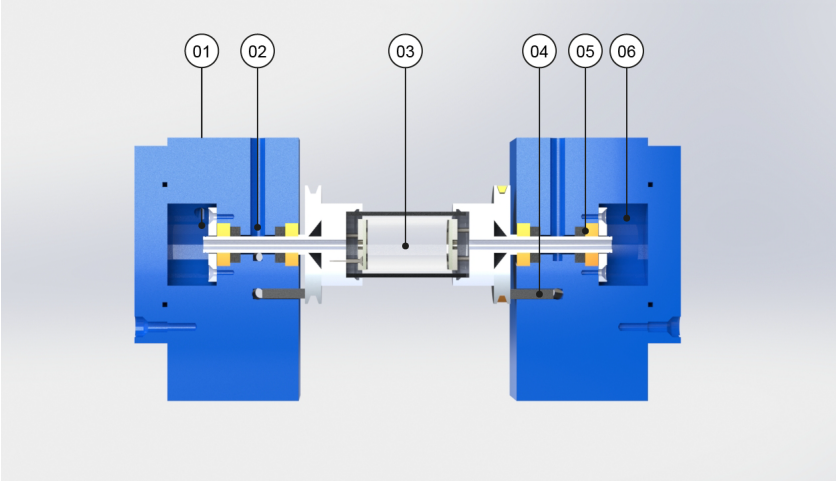

Figure 3.8: Spinning arc plasma reactor: (01) gas inlet in manifold block, (02) lubrication channel, (03) reactor-electrode assembly, (04) carbon block, (05) oil seal (black) and bearing (yellow), (06) vacuum chamber.

3.2.2. Optical emission spectrometry

The plasma discharge was observed by optical emission spectroscopy (OES). OES is a non-intrusive measurement technique which enables the study of a large variety of plasma chemical processes. The radiation detected by OES originates from atomic and molecular electronic transitions [62]. The electronic transition consists of the excitation of heavy particles by electron impact from ground level q to the excited level p and the decay to level k by spontaneous emission. The central wavelength of this emission is characteristic of the radiating particle and the intensity of the emission is correlated to particle density in the excited state [62]. The radiation of reaction products is a valuable indication for dissociation [62]. Electronic states unable to decay through spontaneous emission are called metastable states and have a long life time. Resonant transitions are transitions directly linked to the ground state.

To eliminate the interference of the background radiance originating from the laboratory environment, the spectral radiance was measured prior to ignition of the plasma. To assess whether the background radiance significantly altered over the duration of the experiment, a second measurement was preformed after the plasma extinguished.

The integration time of the spectrometer is analogenous to the shutter speed of a camera. The longer the integration time of the spectrometer, the longer the exposure time of the detector of the spectrometer and thus the time to record incoming photons. The integration time was set according to the OceanView operation manual to the number of counts of the greatest amount of light was about 85 % of the detectors capability, i.e. the number of counts where the detector became saturated [63]. The integration time is highly dependent on the luminosity of the plasma. Therefore, as the plasma significantly changed in luminosity, the integration time was adjusted accordingly.

3.3. Experimental procedure

In order to establish the relationship between conditions of the plasma and CO_2 reactor performance, two rounds of experimental procedures were employed. The first one aims to establish a relation between the system variables and the plasma parameters. The second round aims to couple these system variables to the CO_2 reactor performance.

In this section, the general procedures for executing an experiment will be explained, followed by a more detailed explanation of the specific experimental procedures for Argon and CO_2.

3.3.1. General procedures

Prior to each experiment, the system was depressurised with vacuum pump P03 and then fed with the filling gas. To begin filling the reactor vessel, valve HV01A/B was opened and PCV01A/B was set to 0.1 barg and then HV02A/B was opened to fill the vessel. Once the vessel was filled, the system was depressurised by maximising pump capacity, generally decreasing the pressure to 2 mbara. This was repeated several times to

flush the reactor vessel thereby decreasing the number of background impurities.

After flushing the vessel, the desired pressure was achieved by balancing the feed rate to the pump capacity (generally set at 25%) by adjusting the flow rate with HV02A/B. The plasma was ignited at low pressure at the desired power level. In general, the plasma was ignited at a pressure of 10 mbar and an applied power of 1 kW, unless otherwise stated.

Power to the plasma reactor was regulated by the control panel. For safety considerations this control panel remained unplugged when it was not in use. Upon plugging the control panel, the safety relay has to reset. At this point, the control panel could be turned on. The motor was switched on, after which the applied power on the electric heater was selected, igniting the plasma.

After ignition, the pressure was then elevated slowly by increasing the feed rate by adjusting HV02A/B whilst the pump capacity, applied power and rotational speed remained constant. In general, the pressure gauge was to coarse to determine the absolute pressure. Therefore, the pressure indicator of pump P03 was used to determine the system pressure.

At the end of an experiment, power to the reactor was cut with the control panel. For safety considerations, the control panel was unplugged. Once the power was cut, the feed line was closed and the vacuum pump was opened to equilibrate the pressure inside the vessel to atmospheric pressure.

3.3.2. Argon experiments

The aim of the argon experiments was to establish the relationship between the condition of the plasma and the system variables. The condition of the plasma is characterised by the plasma parameters. These plasma parameters are derived from emission spectra recorded at each measurement. The system variables investigated were pressure, applied electric power, rotational speed and gas feed rate.

The argon was ignited according to the general procedure. The first set of experiments were performed to capture the plasma behaviour with the digital camera at different filling pressures, varying the pressure from 10 to 150 mbar. In the second set of experiments the relationship between the system variables and the plasma parameters was explored. Emission spectra were recorded in OceanView 1.6.7. at the desired conditions to determine the plasma parameters.

The flow rate was varied by adjusting the pump capacity and subsequently balancing the feed with needle valve HV02A in order to keep filling pressure constant. Pump capacity was varied from 15% to 25% and finally to 50%. Applied power was varied by switching on either one or both the heating coils. Each heating coil represents an applied power of 1 kW. Thereby the applied power could either be 1 kW or 2kW. The rotational speed of the reactor-electrode assembly was regulated with the control panel. The rotational speed was varied from 950 rpm to 1500 rpm and finally to 1800 rpm. Pressure was varied from 10 to 150 mbar according to the general procedure.

3.3.3. CO_2 Dissociation experiments

Based on the knowledge of the argon experiments, the relationship between the system variables and the CO_2 reaction performance was assessed in a second round of experiments. The ignition procedure remained largely the same. However, it has proven difficult to ignite CO_2 at the general ignition conditions. Therefore, the ignition pressure had to be reduced 8 mbar and the applied power to 2 kW.

In a first round of experiments concentrated on a pure CO_2 discharge. In a preliminary attempt, the emission spectra was recorded at different filling pressures. Additionally, the plasma was captured with the digital camera at each recording. However, it would prove difficult to sustain the CO_2 plasma. This limited the experiment to varying the pressure from 8 - 16 mbar at an applied power of 2 kW. In addition to these experiments, the reactor performance was measured in time at 2 kW and 10 mbar. The reactor effluent was sampled by rerouting the stream by opening HV05 and closing HV04 for 90 seconds at set instances 0.00, 3.00, 10.00 and 20.00 minutes. These intervals were selected to allow for sufficient handling time and remain within the operational time limit of the prototype. These samples were analysed by gas chromatography to determine the conversion of CO_2. Additionally, at each time instance a read-out of the electricity meter, clamp meter, multimeter and flow meter was performed to determine the energy efficiency.

Based on the results of the first round, a second round of experiments focused on the addition of argon to improve the reactor performance for CO_2 dissociation. The ignition was performed with pure argon instead of CO_2. The effect of an argon admixture was assessed at two different partial pressures, 30 mbar and 100 mbar. After ignition, CO_2 was added to the argon feed and the the emission spectra was recorded in addition to capturing the plasma with the digital camera. Again it would prove difficult to sustain the CO_2 plasma. This limited the experiment to varying the pressure from 30-39 mbar at 30 mbar admixture and 100-103 mbar at

100 mbar admixture, both at 2 kW applied power. Similar to the first round, the reactor performance was measured in time. The procedure remains mostly the same, although the sample time had to be reduced to 60 seconds at 30 mbar and 30 seconds at 100 mbar.

3.3.4. Experiments at reduced interelectrode gap

Based on the results of the argon and CO_2 experiments, the effect of the reduced electric field was investigated by reducing the length of the discharge tube from the original 300mm to 120mm. The experimental procedure for argon experiments remained identical to those preformed prior to the decrease of the interelectrode gap.

At a reduced interelectrode gap of 120 mm, the CO_2 was ignitable at 10 mbar, 1 kW. Thus, the ignition procedure for these experiments remained identical to the general procedure. The operational pressure range was significantly larger. This allowed for a another round of CO_2 dissociation experiments, investigating the effect of the filling pressure and the applied power on the reactor performance at constant rotational speed and pump capacity. In these experiments, the filling pressure was varied from 10 to 70 mbar. This was repeated three times at an applied power of 1 kW and three times at 2 kW. At each condition the emission spectrum was recorded with the spectrometer, the plasma was captured with the digital camera and the reactor effluent was sampled. Samples were taken for a duration of 30 seconds. In addition, a general readout of the electricity meter, clamp meter, multimeter and flow meter was performed.

It is known that the flow rate has a significant effect on the conversion [5]. Therefore, in a last round of experiments the effect of the flow rate on the reactor performance was assessed. This time around, the pump capacity was not constant. Instead, the pump was given a pressure set point of 30 mbar and to achieve this it would vary the pump capacity. The flow rate was regulated with needle valve HV02B, varying the flow rate from about 35 to 300 $NmlCO_2/min$. In addition to a general readout of the meters, the effluent stream was sampled at the various flow rates.

3.4. Analytical methods

Different methods were applied to analyse the data obtained during measurements. This section will provide a description of the analytical methods employed. Most importantly, the analytical methods applied to determine the plasma parameters from emission spectra. In addition, the evaluation of the reactor performance and the identification of chemical species in emission spectra will be discussed.

3.4.1. Evaluation of Reactor Performance

The ideal volumetric fraction (ϕ) of the effluent components was determined by off-stream gas chromatography. Considering the 1:1 molar ratio of CO_2 dissociation and under the assumption that the selectivity is a 100%, the absolute conversion of CO_2 was determined as follows,

$$\chi_{\text{abs,CO}_2} = \frac{\phi_{\text{CO}}}{\phi_{\text{CO}} + \phi_{\text{CO}_2}}, \tag{3.1}$$

The samples would prove to contain significant amounts of nitrogen and oxygen. These were probably a result of either sampling or leakages, or a combination of both. Although less than ideal, these effluent components were ignored.

$$\eta = \frac{\dot{n}_{\text{CO}_2}\chi_{\text{abs,CO}_2}N_a \cdot 1.602 \cdot 10^{-19}(\text{J/eV}) \cdot \Delta H}{P_{\text{plasma}}} \tag{3.2}$$

where $\dot{n}_{\text{CO}_2}$ is the molar flow rate of CO_2 as calculated from the feed line flow meter (FT) in mol/s, N_a is avogadro's number of 6.02×10^{23} molecules/mol, ΔH the dissociation enthalpy of 2.9 eV/molecule and P_{plasma} the dissipated power in the plasma in W. The dissipated power in the plasma is not measured directly. Instead, it is determined according,

$$P_{\text{plasma}} = P_{\text{consumed}} - P_{\text{idle}} - I_{\text{heater}}U_{\text{heater}} \tag{3.3}$$

where P_{consumed} is the power consumed in W as measured by the electricity meter (PL) as shown in figure 3.5, I_{heater} the current on the electric load as measured by the clamp meter (A), U_{heater} is the voltage over the heater as measured by the multimeter (V) and P_{consumed} is the power consumed whilst the reactor is idle. The reactor runs idle when both the reactor-electrode assembly and fan are rotating. At the lowest rotational speed about 130 W is consumed whilst the reactor is idle.

The feed line flow meter was calibrated to measure the normal volumetric flow rate of nitrogen. This can be converted to the molar flow rate of CO_2 according,

$$\dot{n}_{CO_2} = \frac{C_{N_2,CO_2} \dot{V}_{N,N_2} p_s}{R T_s} \tag{3.4}$$

where C_{N_2,CO_2} is the conversion factor for N_2 to CO_2, according to the Bronkhorst technical manual the conversion factor is 0.74 [64], $\dot{V}_{N,N_2}$ is the normal volumetric flow rate of N_2, p_s is the standard pressure and T_s the standard temperature.

3.4.2. Chemical species identification

One of the primary purposes of emission spectroscopy is the identification of chemical species present in the plasma. Each prominent peak present in the recorded spectra was evaluated. Atomic and ionic emissions were identified with wavelength tables from NIST [65] and the emission of molecular species were identified with the book of Pearse and Gaydon [66]. For each prominent peak, the candidates were identified among the species listed below. Besides particles associated with the filling gasses, species commonly associated with background impurities were evaluated. These candidates were identified when a characteristic wavelength of said species was within the resolution of the spectrometer (about 5-10 Å) of the peak wavelength. The most probable candidate was selected on the basis of their relative intensity and the presence of associated band heads. This does not exclude the presence of the other species, as the emission could have been a superposition of multiple emitting species.

- Argon plasma: Ar, Ar^+, H_2O, OH, O, O^+, O_2, O_2^+, N_2, N_2^+, N, NO
- CO_2 plasma: CO_2, CO_2^+, CO, CO^+, C, C_2, N_2, CN, N, NO, N_2, N_2^+, H_2O, OH, O, O_2, O_2^+, O^+

3.4.3. Plasma parameters

Knowledge of the electron temperature, electron density and the EEDF is essential to acquire insight in the physics and chemistry of the plasma [67]. Species in an optically thin, LTE plasma follow a Boltzmann distribution,

$$\frac{n^p}{n^k} = \frac{g_p}{g_k} \exp\left(-\frac{\varepsilon_p - \varepsilon_k}{k_B T_e}\right), \tag{3.5}$$

where n is the population density and g is the statistical weight. The spectral line intensity corresponding to the transition from the excited state p to the lower excited state k for an optically thin plasma is given by,

$$I_{p,k} = K_{p,k} n^p h \upsilon_{p,k} A_{p,k}, \tag{3.6}$$

where $A_{p,k}$ is the transition probability from level p to level k, $\upsilon_{p,k}$ is the collision frequency, $K_{p,k}$ is a calibration factor, which depends on the system. Substitution of equation 3.5 and 3.6 gives the ratio of two spectral lines emitted by the same species [68],

$$\ln\left(\frac{I_{p,k} K_{i,j} \upsilon_{i,j} A_{i,j} g_{i,j}}{I_{i,j} K_{p,k} \upsilon_{p,k} A_{p,k} g_{p,k}}\right) = -\frac{\varepsilon_p - \varepsilon_i}{k_B T_e} \tag{3.7}$$

The electron temperature was determined with the intensity ratio of two spectral lines, the quantity on the left hand side of equation 3.7. This yields the electron temperature for spectral lines with known energy difference, this methods is referred to as the two-line method.

The electron number density was determined from the intensity ratio of an atom and its ion spectral lines through the Boltzmann and Saha equations [7, 69, 70],

$$n_e = \frac{(2\pi m k_B T_e)^{3/2}}{h^3} \left(\frac{2 A^{\mathrm{II}} g^{\mathrm{II}} \lambda^{\mathrm{I}} I^{\mathrm{I}}}{A^{\mathrm{I}} g^{\mathrm{I}} \lambda^{\mathrm{II}} I^{\mathrm{II}}}\right) \exp\left(-\frac{\varepsilon^{\mathrm{II}} - \varepsilon^{\mathrm{I}} + \varepsilon_i^{\mathrm{I}} - \Delta\varepsilon_i^{\mathrm{I}}}{k_B T_e}\right), \tag{3.8}$$

where m is the electron mass, λ is the wavelength, T_e is the excitation temperature, ε is the energy of the emitting level, ε_i^0 is the ionisation energy of the neutral atom and $\Delta\varepsilon_i^0$ is the lowering of the ionisation energy.

The rotational temperature is often a good approximation for the gas temperature when rotational-translational relaxation processes are quick or the nascent distribution is thermalised [71]. As such, the gas temperature can be determined from the population distribution in rotational levels of excited diatomic molecules. Commonly used transitions for the determination of the rotational temperature are $N_2(C^3\Pi_u \rightarrow B^3\Pi_g)$, $OH(A^{2+} \rightarrow X^2\Pi_i)$ and $N_2^+(B \rightarrow X)$ [71]. However, Ar metastable levels are known to increase the population of $N_2(C^3\Pi_u)$ levels through excitation transfer [71]. In this case, the nascent distribution of the rotational population is non-thermal and the population does not adhere a Boltzmann distribution [71]. Therefore, other transitions of diatomic molecules, such as $OH(A \rightarrow X)$, should be used to determine the rotational temperature. In case of $OH(A \rightarrow X)$, the rotational temperature can be deduced from the slope in a Boltzmann plot adhering [72],

$$\ln\left(\frac{I\lambda}{A}\right) = \text{const} - \frac{5040}{T_r}E \tag{3.9}$$

where T_r is the rotational temperature and the constant stands for all factors independent of the rotational quantum number. The Boltzmann plot is constructed with the quantity on the left hand side for the relative intensities of the various band heads as a function of the respective energy level. The rotational temperature can be deduced from the slope $(-5040/T_r)$ of the Boltzmann plot.

The previous methods have all used the intensity of spectral lines to deduce plasma parameters. Besides the intensity, the plasma parameters can be deduced from the spectral line width. Although the resolution of the spectrometer proved to be to coarse to employ these methods, they are discussed in detail for completeness. The spectral line broadening is induced by various broadening mechanisms. Most importantly, van der Waals broadening $(\Delta\lambda_W)$, Stark broadening $(\Delta\lambda_S)$ and Doppler broadening $(\Delta\lambda_D)$ [62]. Van der Waals broadening is the result of dipolar interactions between excited and neutral ground state atoms, Stark broadening due to the electromagnetic field, Doppler broadening due to the velocity distribution and instrumental broadening (Δ_I) due to the apparatus itself [62]. The observed spectral line is a convolution of the different mechanisms, resulting in a the Voigt function. More specifically a convolution of Gaussian broadening, due to Doppler and instrumental broadening, and Lorentz broadening, due to Stark and Van der Waals broadening. The Gaussian full width at half maximum $(\Delta_{\text{FWHM},g})$ is described by,

$$\Delta_{\text{FWHM},G} = \sqrt{(\Delta\lambda_D)^2 + (\Delta\lambda_I)^2} \tag{3.10}$$

Likewise, the convolution of the two Lorentzian profiles whose full width at half maximum $(\Delta_{\text{FWHM},L})$ is described by,

$$\Delta_{\text{FWHM},L} = \Delta\lambda_S + \Delta\lambda_W \tag{3.11}$$

The H_α line is commonly used to determine the gas temperature from Doppler broadening, as Doppler broadening is stronger for light elements [62],

$$\Delta\lambda_D = 2\sqrt{\ln 2}\lambda_0\sqrt{\frac{2kT_g}{mc^2}} \tag{3.12}$$

Alternatively, the electron density can be determined from the Stark broadening of H_α line [73],

$$\Delta\lambda_{\text{FWHA},S} = 0.549\text{nm}\left(\frac{N_e}{10^{23}\text{m}^{-3}}\right)^{0.67965}, \tag{3.13}$$

provided that full width at half area is equal to full half width at half maximum [74]. Van der Waals broadening can be expressed by the relation[75],

$$\Delta\lambda_W = K_i\left(\frac{T_g}{\mu}\right)^{3/10}N \tag{3.14}$$

where μ is the reduced mass of the excited and neutral ground state pair, N is the neutral species density and K_i is a constant based on the spectral line and excited particle polerisability.

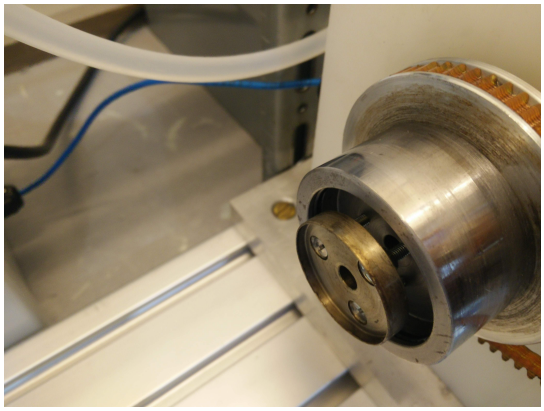

Figure 3.9: Close-up of wolfram service assembly

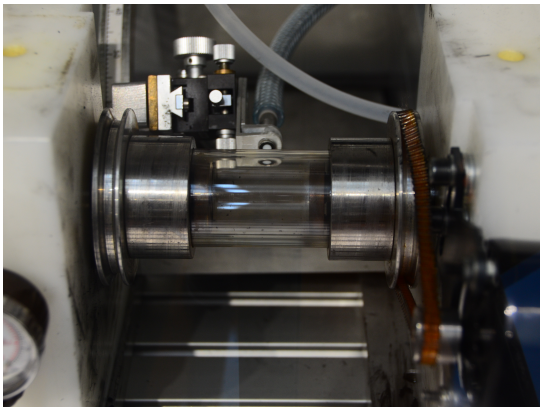

Figure 3.10: Close-up of reduced interelectrode gap

3.5. Design alterations

The initial prototype, as was developed by Van Kranendonk, was tested for non-reactive species. However, further experimental use required additional safety measures and the ability to withstand higher temperatures. Therefore, over the course of this study, several design alterations were made which are shortly discussed below.

First and foremost, all high voltage components were individually encased to prevent inadvertent contact. In addition, an entire rework of the electrical circuit was done to properly insulate and isolate all electrical components. All high voltage components were placed inside a fume hood equipped with a magnetic switch. This magnetic switch cuts the electrical power to prevent inadvertent contact with high voltage components. Additionally, the fume hood sash was replaced with a poly-carbonate sash to act as a barrier in case of an implosion of the discharge tube. Capacitors were neither present nor included in the design, to prevent the storage of electric charge. Additionally, the plasma reactor was installed on a aluminium frame which was grounded to remove any electric charge in case of failure. An inherently safer design was achieved by replacing the electric water boilers with an electrical heater as the main electric load to draw current to the plasma reactor. This replacement reduced the risk imposed by the potential evaporation of water, which would have rendered the electric boiler unable to dissipate the induced heat. At a later stage, the 50 kV ignition was omitted in favour of inherently safer design.

Initially, both the discharge tube and the electrodes were redesigned to withstand higher temperatures. The original poly-carbonate tube was replaced with a quartz tube for its superior melting point and optical transmissivity. Likewise, both electrodes were replaced by wolfram electrodes for their superior melting point. Both changes necessitated a redesign of the service assembly, predominantly to accommodate the wolfram electrodes. However, in time this design would prove to be unsuitable as it relied on a press fit to accommodate the wolfram electrodes. Due to thermal expansion induced by the plasma, this press fit would fail. Therefore, in time, the wolfram electrodes were replaced by stainless steel electrodes.

4

Results

This chapter presents the results obtained from the experimental work outlined in Chapter 3. First, the results of a series of argon experiments is presented, which seeks to relate the plasma parameters to the system variables. Second, the results of the CO_2 are outlined, investigating the relationship between plasma conditions and CO_2 dissociation reaction performance. This reaction performance is bench-marked against existing configurations introduced in Chapter 2.

4.1. Characterisation of argon plasma

The main purpose of the argon experiments is to understand the relationship between the plasma parameters and the observed plasma confinement and stabilisation. To assess this relationship, the plasma was investigated experimentally with argon as a non-reactive species, as outlined in chapter 3. The experiments were

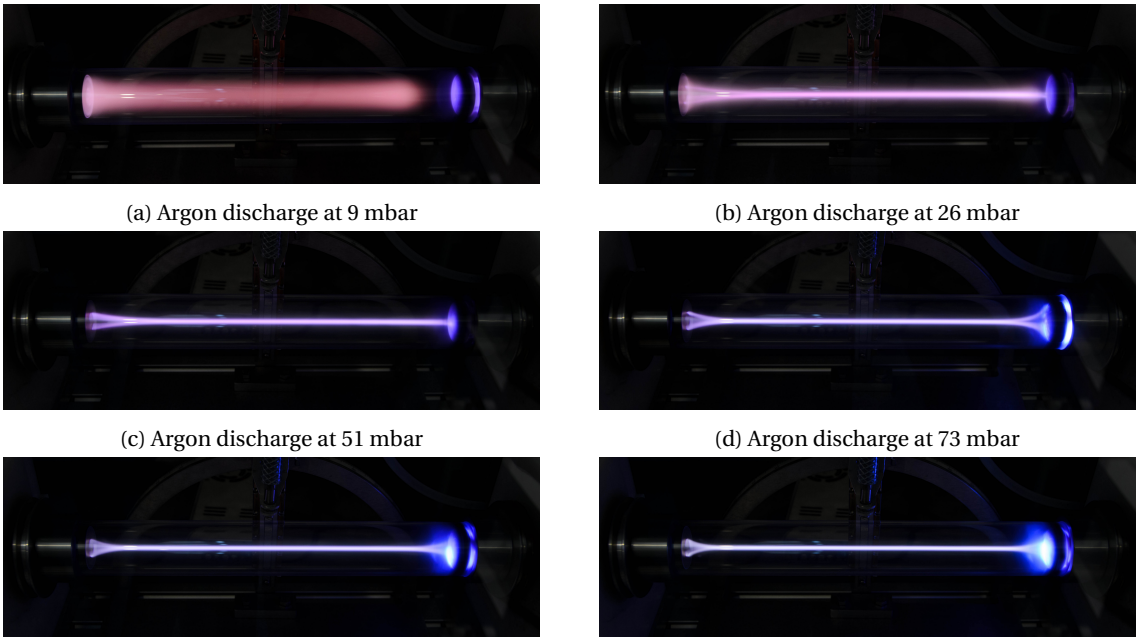

(a) Argon discharge at 9 mbar

(b) Argon discharge at 26 mbar

(c) Argon discharge at 51 mbar

(d) Argon discharge at 73 mbar

(e) Argon discharge at 100 mbar

(f) Argon discharge at 150 mbar

Figure 4.1: Argon discharge at different pressures, 1 kW. The discharge tube has a length of 300mm with the anode situated on the left-hand side and the cathode on the right hand side of the image, ISO400, 1/30s, f5.6

performed sequentially by slowly elevating the filling pressure from 10 mbar to 150 mbar at constant applied power and pump capacity. The images captured by the digital camera during the experiments are presented in Figure 4.1 at the various pressure levels. The characteristically violet/lilac colour of an argon plasma can be observed in these images. As evident from Figure 4.1(a) a glow discharge was induced at low pressure. This

discharge was identifiable by the characteristic diffuse positive column, which occupied almost the entire length of the tube and the dark space near the cathode.

At about 30 mbar the discharge made a transition from a diffuse to a contracted plasma. As pressure increased the plasma became increasingly contracted and luminous. The most interesting aspect at these filling pressures was the confinement and stabilisation of the plasma. This straight line was perturbed by buoyancy forces as soon as the reactor-electrode assembly stopped rotating. Strikingly, a blue hue could be observed around the cathode at irregular intervals. Furthermore, a deposition of an unknown compound was observed over time. This deposition is responsible for the black artefact near the cathode in these images.

4.1.1. Optical emission spectroscopy analysis

The emission spectra of the plasma were recorded at each measurement. These spectra provide insight into the plasma parameters as discussed previously in section 3.4.3. The spectra were recorded over a wavelength range of 180-1090 nm with the tip of fibre optic cable positioned above the reactor tube, aimed at the centre of the reactor-electrode assembly. In order to reduce background noise in the spectrum, 25 scans were made in succession. These scans were averaged to achieve a signal-to-noise ratio of 5:1. Figure 4.2-4.4 depict the recorded emission spectra at different filling pressures whilst applied power, rotational speed and pump capacity were kept constant. Figure 4.5 depicts the emission spectrum at the same filling pressure as Figure 4.4 at 2 kW. Table 4.1 lists the atomic or molecular transitions corresponding to the highlighted peaks in the spectra.

Table 4.1: Peak values of the dominant spectral lines in the reported argon spectra with corresponding particle species, characteristic wavelength as reported in the literature reference and the transition associated with the characteristic wavelength. Atomic term symbols of atomic transition lines have been omitted.

Peak	Species	Wavelength	Transition	Reference
309.47 nm	OH	308.90 nm	$A^2\Sigma^+ \rightarrow X^2\Pi$ (0,0)	[66]
336.67 nm	N_2	337.13 nm	$C^3\Pi_u \rightarrow B^3\Pi_g$ (0,0)	[66]
357.36 nm	N_2	357.69 nm	$C^3\Pi_u \rightarrow B^3\Pi_g$ (0,1)	[66]
655.88 nm	H	656.45 nm	-	[65]
696.365 nm	Ar	696.54 nm	-	[65]
706.448 nm	Ar	706.72 nm	-	[65]
737.919 nm	Ar	738.40 nm	-	[65]
750.988 nm	Ar	750.39 nm	-	[65]
763.16 nm	Ar	763.51 nm	-	[65]
771.85 nm	Ar	772.42 nm	-	[65]
777.052 nm	O	777.1 nm	-	[65]
794.371 nm	Ar	794.82 nm	-	[65]
801.286 nm	Ar	801.48 nm	-	[65]
810.78 nm	Ar	810.37 nm	-	[65]
826.292 nm	Ar	826.45 nm	-	[65]
851.631 nm	Ar	852.14 nm	-	[65]
866.615 nm	Ar	866.79 nm	-	[65]
911.78 nm	Ar	912.29 nm	-	[65]
921.962 nm	Ar	922.45 nm	-	[65]
965.466 nm	Ar	965.79 nm	-	[65]

An example of the emission spectra obtained from measurements at 9 mbar is shown in Figure 4.2. The majority of the spectral lines in red and near-infrared region consisted of argon ($2p \rightarrow 1s$) spectral lines. Besides argon, atomic oxygen emissions at 777.1 nm and the H-alpha line from the hydrogen Balmer series at 656.45 nm were observed. The spectral lines in the ultraviolet region were mainly composed of molecular emissions of OH ($A \rightarrow X$) and N_2 second positive system. These emissions presumably arose from unavoidable traces of nitrogen, oxygen and water as background impurities in the system.

What can be clearly seen in Figure 4.3 compared to Figure 4.2 is the dominance of the argon spectral lines in the recorded spectrum at 30 mbar. As discussed previously, at 30 mbar the plasma transitioned to a luminous contracted plasma. This increase in luminosity coincided with a steep surge in the emission

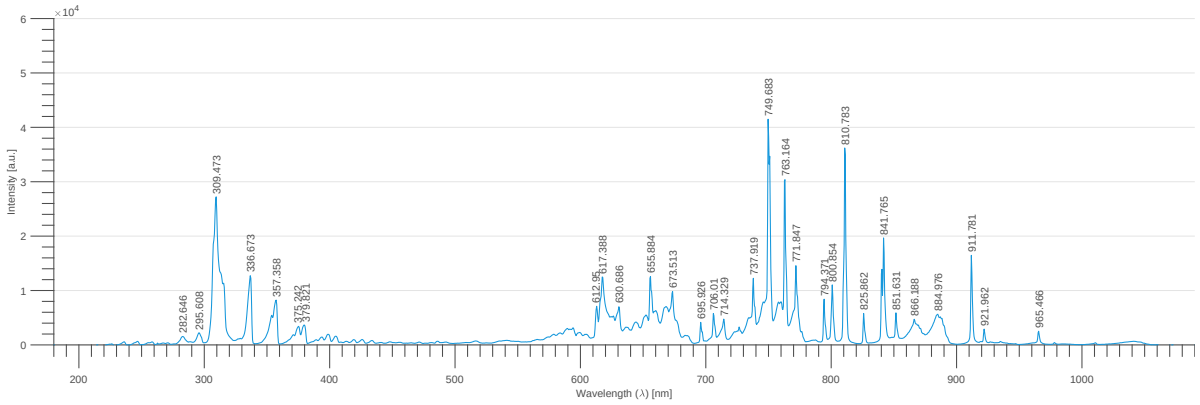

Figure 4.2: Argon emission spectrum recorded at 9 mbar with an applied power of 1 kW, 500 ms

intensity of the spectral lines. As a result, the integration time had to be reduced significantly. Meanwhile, the intensity of impurities fell in comparison to the intensity of the argon spectral lines. Besides the shift in intensity, no additional spectra lines were detected. Most notably, there was a lack of any persistent spectral lines from singly ionised argon atoms Ar−I in the 400-500 nm range.

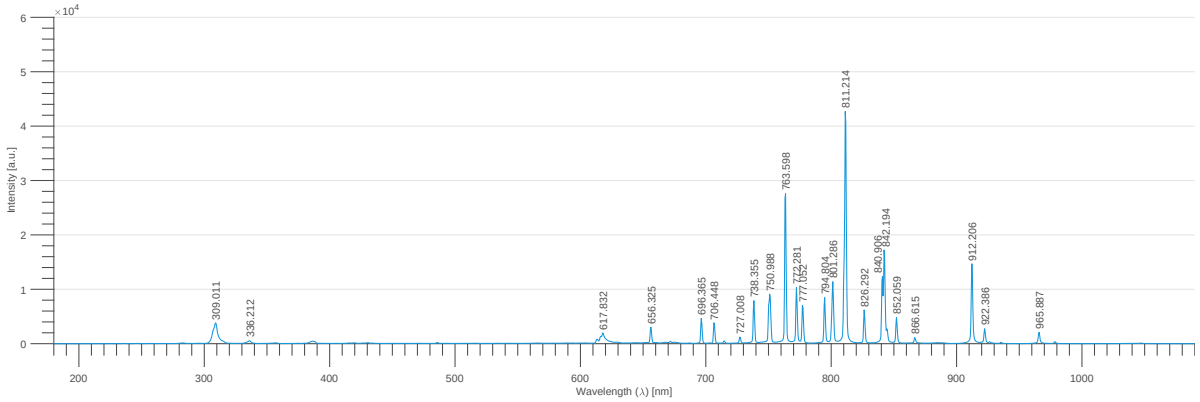

Figure 4.3: Argon emission spectrum recorded at 30 mbar with an applied power of 1 kW, 30 ms

Whereas the increase from 10 mbar to 30 mbar led to a notable rise in intensity of the Ar-I ($2p \rightarrow 1s$) lines, Figure 4.4 indicates that further elevation of the pressure to 100 mbar solely led to a subtle increase in intensity of the Ar lines in comparison to the intensity of impurities.

At first glance, Figure 4.5 shows no differences in the recorded spectrum at increased applied power. However, the integration time had to be reduced even further to 10 ms to prevent overexposure of the spectrometer. This reduction in integration time indicates that an increase in applied power was associated with an increase in the intensity of the Ar-I lines. Again, the distribution of the spectral lines remained largely the same and no Ar-II lines were recorded.

In summary, these results suggest that the distribution of the spectral lines remained largely the same as either pressure or applied power was elevated. Furthermore, an increase in either pressure or applied power was associated with an emission intensity gain of the Ar-I ($2p \rightarrow 1s$) spectral lines. In comparison the spectral lines corresponding with impurities fell in intensity. These impurities encompassed spectral lines of hydroxide, nitrogen and atomic oxygen and were most notable at low pressure. Intriguingly, there was an apparent lack of Ar-II lines, which intensity was at the least negligible in comparison to the Ar-I lines.

So far this section has focused on the recorded spectra. The final part of this section is concerned with the plasma parameters which were obtained from these spectra. As outlined in section 3.4.3, the emission spectra provide knowledge on the electron excitation temperature, electron density and gas temperature of the plasma.

The electron density had to be determined by De Voigt fitting of the H_α line, as the Ar-II lines, required for the two-line method, were not detected. The OH ($A \rightarrow X$) rotational lines in the range of 306-312 nm were

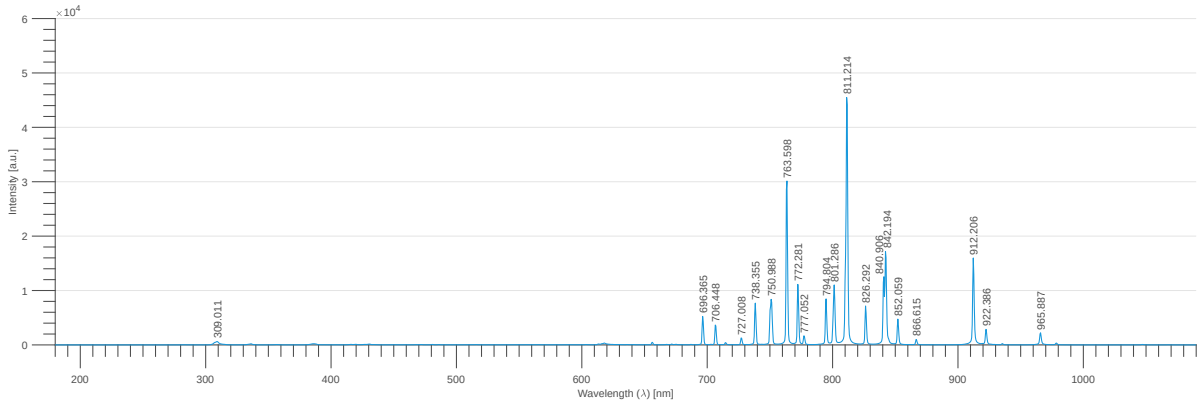

Figure 4.4: Argon emission spectrum recorded at 100 mbar with an applied power of 1 kW, 20 ms

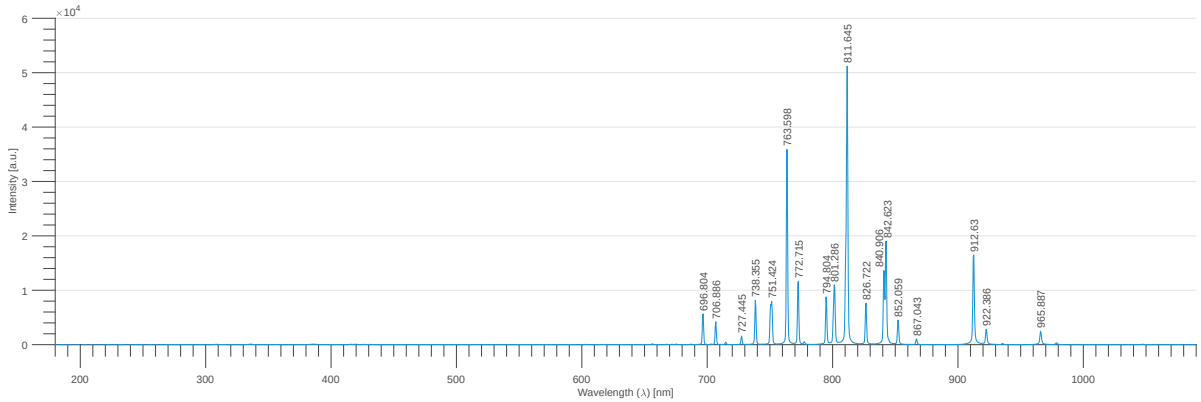

Figure 4.5: Argon emission spectrum recorded at 100 mbar with an applied power of 2 kW, 10 ms

suitable to determine the gas temperature by a Boltzmann plot. However, the resolution of spectrometer proved to be too coarse to obtain an accurate fit of the spectrum for both methods. Therefore, this part solely focuses on the relationship between the electron excitation temperature and the system parameters.

As discussed previously in Section 2.1.2 the excitation temperature affects the EEDF and thus determines the distribution of electron energy levels. A higher excitation temperature is associated with a population shift towards the high energy tail of the Boltzmann distribution, thus a higher mean electron energy. The effect of the system parameters on the excitation temperature was derived from the spectra obtained from measurements as shown previously. More specifically, the excitation temperature was derived from the peak intensity ratio of the Ar-I lines at 706.72 and 750.39 nm. These lines were selected because both lines are not in the vicinity of any other intense spectral lines and the lack of any $5p \rightarrow 4s$ spectral lines in the 400-500 range. The corresponding transition probabilities are listed in Table 4.2.

Table 4.2: Selected argon levels with corresponding wavelength and transition probability

Peak	Transition	A_{ij} [s^{-1}]	g_i [-]	E_i [cm^{-1}]	Reference
706.72 nm	$2p_3 \rightarrow 1s_5$	$0.0395 \cdot 10^8$	5	107290	[76]
750.39 nm	$2p_1 \rightarrow 1s_2$	$0.472 \cdot 10^8$	1	108723	[76]

The effect of the applied power and the filling pressure on the electron excitation temperature is illustrated in Figure 4.6. As can be seen in Figure 4.6a, increasing the applied power tended to elevate the electron temperature. Additionally, the increase in pressure also seems to have led to a slight increase in electron temperature. In Figure 4.6b, the data from Figure was fitted . Neither of the trends described however could be statistically backed as shown by the overlapping confidence intervals, given this data set.

Figure 4.7 illustrates the effect of the rotational speed of the reactor-electrode assembly on the electron excitation temperature. With successive increments in rotational velocity the results remain largely clustered

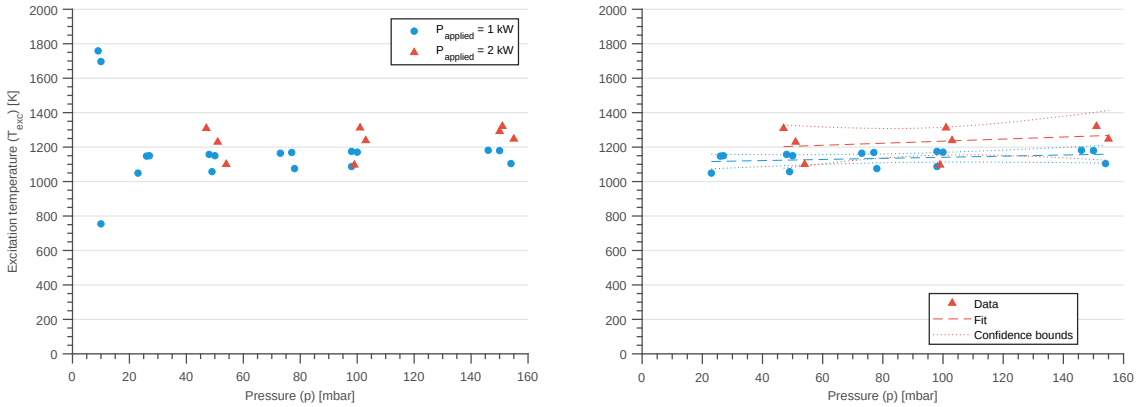

(a) Derived electron temperature from intensity ratio of spectral lines 706 and 750 nm seen at 10, 30, 50, 75, 100, 150 mbar

(b) Same data as in (a) with omission of 10mbar measurements. Trend lines with 95% confidence intervals were fitted onto the data.

Figure 4.6: Electron temperature derived from measured spectra at various pressures and applied power levels.

at the same electron temperature. The measurements were taken sequentially . It seems that the clusters of data correspond with the performed repetitions. As such, the deviation between each repetition is significantly larger than the deviation between the measurements made at different rotational velocities. It is therefore speculated that the rotational speed and the excitation temperature are uncorrelated. Nonetheless, it is evident from the the overlapping confidence intervals in Figure 4.7b that the results obtained here are not statistically relevant.

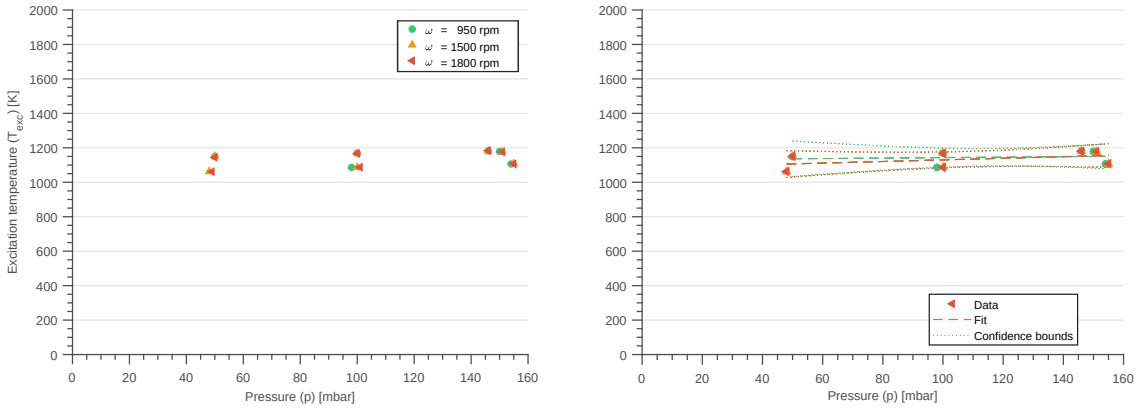

(a) Excitation temperature as a function of filling pressures and rotational speed for pure argon discharge

(b) Same data as in (a). Trend lines with 95% confidence intervals were fitted onto the data.

Figure 4.7: Electron temperature derived from measured spectra at various pressures and rotational velocities.

Finally, the effect of the gas flow rate is given in Figure 4.8 where the pump capacity acts as proxy of the gas flow rate. As outlined in Section 3.3.2, the gas flow rate was manipulated by adjusting the pump capacity followed by a manual adjustment of the feed needle valve to obtain the same filling pressure. A lower pump capacity corresponds with a lower filling pressure and visa versa. Additionally, measurements were taken by adjusting the pump capacity without adjusting the flow rate. This resulted in a pressure rise as the pressure elevated to new equilibrium whilst the flow rate remained constant. Each cluster observed in Figure 4.8a correspond with a single repetition, akin to the data on rotational velocity. The outliers in the data correspond with the measurements made by adjusting the pump capacity without adjusting the flow rate. Again, the overlapping confidence intervals in Figure 4.8b imply that the results are not statistically relevant. Nonetheless, these data clusters seem to suggest that the flow rate and electron temperature are uncorrelated.

In conclusion, although the results cannot be backed statistically given the current data set it seems that the electron excitation temperature rises with increasing applied power. Interestingly increasing the filling

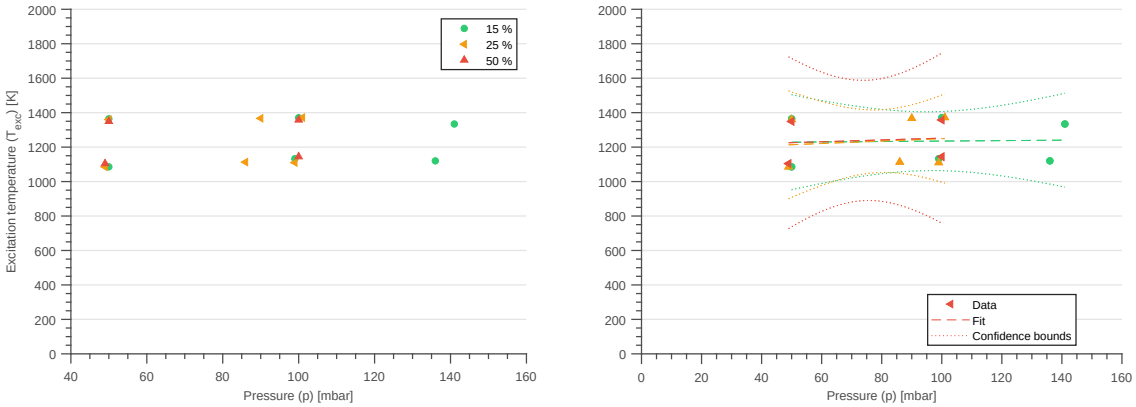

(a) Excitation temperature as a function of filling pressures and pump capacity for pure argon discharge

(b) Same data as in (a). Trend lines with 95% confidence intervals were fitted onto the data.

Figure 4.8: Electron temperature derived from measured spectra at various pressures and pump capacity rates.

pressure seems to elevate the excitation temperature, however the effect is hardly noticeable. The results on the effect of rotational speed and flow rate were largely clustered, which indicates that they either have no effect or a neglectable effect on the electron temperature.

4.2. CO_2 Dissociation

The previous section described the experimental investigation to understand the relationship between the system variables and the plasma parameters for a non-reactive species, such as CO_2. This is an important step to understand the relationship between the system variables and the reactor performance of reactive species. This section describes the results of the experimental investigation as outlined in Section 3.3.3.

The procedure to ignite a CO_2 discharge was identical to an argon discharge. The images captured during these experiments are presented in Figure 4.9. Remarkably, the gas did not ignite at 10 mbar. In order to sustain a discharge the applied power had to be increased to 2 kW and the filling pressure had to be reduced to 8 mbar. This culminated in a faint, green glow discharge. The discharge became increasingly luminous as the filling pressure was elevated. Contrary to an argon discharge, the CO_2 discharge did not transition towards a contracted plasma as the pressure was increased even further. Instead the plasma gradually dimmed with increasing pressure and ultimately extinguished at 16 mbar.

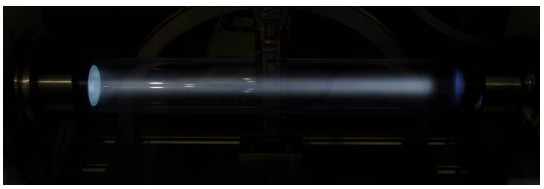

(a) CO_2 discharge at 8 mbar, 2 kW

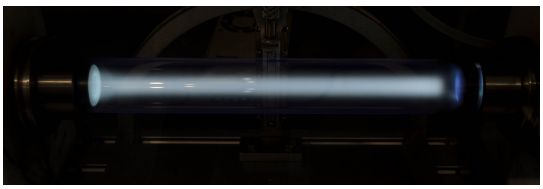

(b) CO_2 discharge at 10 mbar, 2 kW

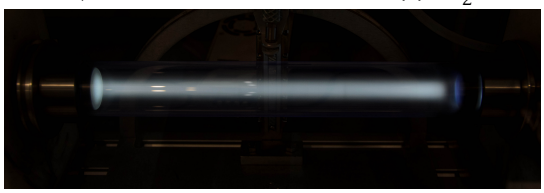

(c) CO_2 discharge at 13 mbar, 2 kW

Figure 4.9: CO_2 discharge at various filling pressures, ISO400, 1/30s, f5.6

4.2.1. Optical Emission Spectroscopy Analysis

This surge and decline of luminosity is clearly reflected in emission intensity of the emission spectra of the plasma recorded at each measurement, as shown in Figure 4.10. In this figure the recorded emission spectra of the CO_2 at filling pressures of 8 mbar, 10 mbar and 13 mbar are visible. Over the duration of the experiments the rotational speed, pump capacity and applied power were kept constant. Because the integration time had to be significantly elongated to acquire the correct exposure, the number of scans was reduced to 9. This culminated in a reduction of the signal-to-noise ratio to 3:1. Table 4.3 lists the molecular or atomic transitions corresponding to the observed intensity peaks in the emission spectra.

The main plasma components identified from the recorded spectra were CO, C_2, O, O_2, N_2, H_2O, OH and H. The recorded emission spectra were dominated by the spectral lines of OH ($A \rightarrow X$) emissions near 308.9 nm, these emissions presumably arose from gas impurities or air inleakage. Additionally, several CO spectral lines were observed in the ultraviolet region. A possible explanation for the intensity of the OH ($A \rightarrow X$) is the superposition of these spectral lines by the emissions of CO ($b^3\Sigma \rightarrow a^3\Pi$) in the 290-325 nm domain. The visible region consisted of overlapping emissions bands of CO and C_2. Most notably, the observed green colour of the plasma stemmed from C_2 Swan band emissions in the 500-570 nm range. A possible explanation for the exalted region in the 400-700 nm is a continuum spectra of various superimposed CO_2 spectral lines. Emissions in the red to near infra-region were concentrated in the 600-700 nm range. These lines comprised of CO^+ and H_α spectral lines. Less intense emissions of oxygen, atomic oxygen and water were observed towards the infrared. Stark differences between the various filling pressures consisted of the emission of the N_2 second positive system at 8 mbar. Interestingly, no observations were made of $CO_2{}^+$ spectral lines. Presumably the intensity of these lines was too weak to be identifiable.

4.2.2. Reaction Performance Evaluation

To assess the reactor performance of the reactor, samples were taken in sample bags from the exhaust gases and evaluated off-stream by gas chromatography. Based on the results obtained from the optical emission

Table 4.3: Peak values of the dominant spectral lines in the reported CO_2 spectra with corresponding particle species, characteristic wavelength as reported in the literature reference and the transition associated with the characteristic wavelength.

Peak	Species	Wavelength	Transition	Reference
216.60 nm	CO	217.30 nm	$A^1\Pi \rightarrow X^1\Sigma$ (5,13)	[66]
262.70 nm	CO	263.00 nm	$A^1\Pi \rightarrow X^1\Sigma$ (11,22)	[66]
282.18 nm	CO	283.31 nm	$b^3\Sigma \rightarrow a^3\Pi$ (0,0)	[66]
296.53 nm	CO	297.74 nm	$b^3\Sigma \rightarrow a^3\Pi$ (0,1)	[66]
309.47 nm	OH	308.90 nm	$A^2\Sigma^+ \rightarrow X^2\Pi$ (0,0)	[66]
329.31 nm	CO	330.57 nm	$b^3\Sigma \rightarrow a^3\Pi$ (0,3)	[66]
336.67 nm	N_2	337.13 nm	$C^3\Pi_u \rightarrow B^3\Pi_g$ (0,0)	[66]
357.36 nm	N_2	357.69 nm	$C^3\Pi_u \rightarrow B^3\Pi_g$ (0,1)	[66]
379.82 nm	N_2	380.49 nm	$C^3\Pi_u \rightarrow B^3\Pi_g$ (0,0)	[66]
387.14 nm	CO	389.31 nm	$C^1\Sigma \rightarrow A^1\Pi$ (0,1)	[66]
410.89 nm	CO	412.48 nm	$C^1\Sigma \rightarrow A^1\Pi$ (0,2)	[66]
449.56 nm	CO	451.09 nm	$B^1\Sigma \rightarrow A^1\Pi$ (0,0)	[66]
481.71 nm	CO	483.53 nm	$B^1\Sigma \rightarrow A^1\Pi$ (0,1)	[66]
518.22 nm	CO	519.82 nm	$B^1\Sigma \rightarrow A^1\Pi$ (0,2)	[66]
559.93 nm	C_2	558.55 nm	$A^3\Pi_g \rightarrow X'^3\Pi_u$ (1,2)	[66]
592.94 nm	C_2	592.34 nm	$A^3\Pi_g \rightarrow X'^3\Pi_u$ (5,7)	[66]
604.07 nm	C_2	605.97 nm	$A^3\Pi_g \rightarrow X'^3\Pi_u$ (2,4)	[66]
612.95 nm	C_2	612.21 nm	$A^3\Pi_g \rightarrow X'^3\Pi_u$ (1,3)	[66]
617.83 nm	CO^+	618.94 nm	$A^2\Pi \rightarrow X^2\Sigma$ (0,2)	[66]
624.04 nm	CO^+	618.94 nm	$A^2\Pi \rightarrow X^2\Sigma$ (0,2)	[66]
655.88 nm	H	656.28 nm	-	[65]
714.77 nm	H_2O	716.45 nm	-	[66]
760.12 nm	O_2	759.37 nm	-	[66]
777.05 nm	O	777.19 nm	-	[65]
844.34 nm	O	844.63 nm	-	[65]

spectroscopy a filling pressure of 10 mbar was selected. At this pressure the spectral lines exhibited the highest intensity, therefore it seemed reasonable that the plasma was in the most energetic state. The gas was sampled at several time points over a duration of 20 minutes whilst the reactor was operated at a filling pressure of 10 mbar with an applied power of 2 kW, constant pump capacity and the lowest rotational velocity. Due to the low filling pressure each sample was filled for 90 seconds.

Figure 4.11 shows the conversion of CO_2 and energy efficiency as a function of time. In this figure, the conversion of CO_2 rapidly increases to a steady-state value, rising from 44.1% to 47.4%. This data must be interpreted with caution as each point represents the conversion of CO_2 over a duration of 90 seconds. The energy efficiency was fairly low and exhibited a similar trend rising from 0.23% to 0.25%. This similarity is consistent with a rise in conversion at constant applied power.

4.2.3. CO_2 dissociation with argon admixture

The results of the previous reaction experiments with CO_2 indicate a fairly low energy efficiency with a reasonable conversion. Given these results, argon was utilised as an admixture in an attempt to improve the reactor performance comparable to the work of Spencer [11]. In this work, Spencer utilised argon to sustain the discharge. She argues that the introduction of argon is beneficial to the plasma as it acts as an electron provider, since argon ionises easily [11].

The effect of an argon admixture on the reactor performance was investigated experimentally. The experimental procedure was similar to the initial experiments discussed in Section 4.1 with the exception of the introduction of CO_2 after ignition. Two background conditions were tested, one with a partial pressure of argon at 30 mbar and one at 100 mbar. The experiment was performed at constant applied power of 2 kW, with constant pump capacity and the lowest rotational speed.

Upon the addition of CO_2 the discharge immediately switches from a violet, contracted plasma to a green diffuse plasma. A similar behaviour has been observed by Spencer [11]. The discharge at different partial

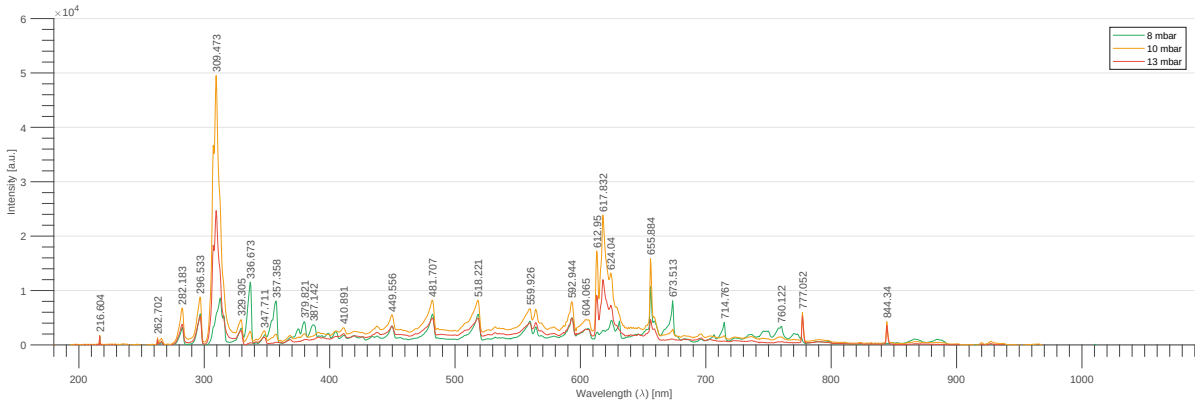

Figure 4.10: Spectrogram CO_2 discharge at various filling pressures

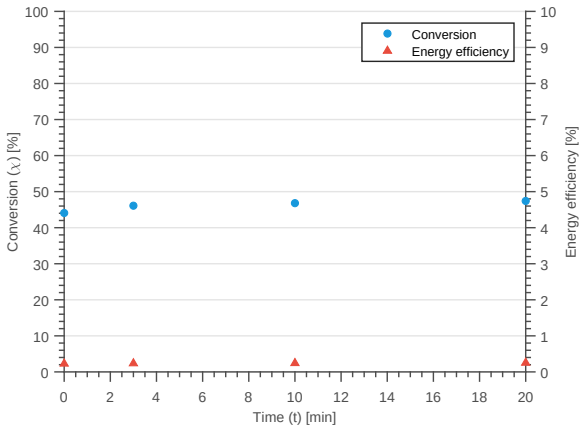

Figure 4.11: Conversion and energy efficiency of CO_2 dissociation at 10 mbar

pressures of CO_2 is visible in Figure 4.12. This transition indicates that argon is no longer the primary excited species [11]. In comparison to the initial pure CO_2 discharge a similar pattern was observed. With an argon background at 30 mbar, the plasma became increasingly luminous as the CO_2 content increased. This luminosity peaked at 33 mbar and gradually degraded until the plasma extinguished at 39 mbar. Both CO_2 plasma with an argon background share this rise and fall pattern in luminosity. The CO_2 plasma with an argon background at 100 mbar differs with the 30 mbar background in the operational range. At 100 mbar, an additional 3 mbar of CO_2 was sufficient to extinguish the plasma.

4.2.4. Optical Emission Spectroscopy Analysis

In Figure 4.13 the recorded emissions spectra at various partial pressures of CO_2 are visible with an argon background pressure at 30 mbar. At first, when the partial pressure of CO_2 is very low, the spectrum is dominated by the argon neutral lines in the 700-900 range. As the CO_2 content increases, the intensity of the argon neutral lines sharply declines. This is in good agreement with the observations made by Spencer [11]. In contrast to the observations of Spencer the decline of the argon neutral lines did not coincide with an increase in intensity of the C_2 Swan bands [11]. Instead, the spectrum was dominated by the lines of OH, CO^+ and O. Again, as the CO_2 content increases further, the intensity of the lines declines. Figure 4.14 shows the recorded spectrum with a background pressure of argon at 100 mbar. Here, increasing the CO_2 content did not coincide with an intensity decline of the Ar-I lines. Instead, the Ar-I remained the dominant part of the spectrum without a clear shift until the plasma extinguished.

4.2.5. Reactor Performance Evaluation

Argon was added in an attempt to improve the reactor performance. The effect of the argon admixture on the reactor performance was investigated according to the same procedure as the pure CO_2 discharge. At 30

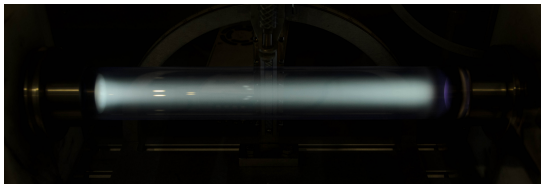

(a) CO_2-Ar discharge at 30 mbar

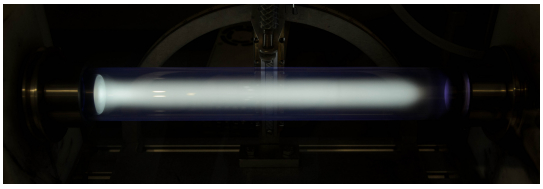

(b) CO_2-Ar discharge at 33 mbar

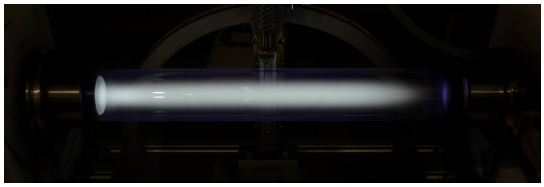

(c) CO_2-Ar discharge at 34 mbar

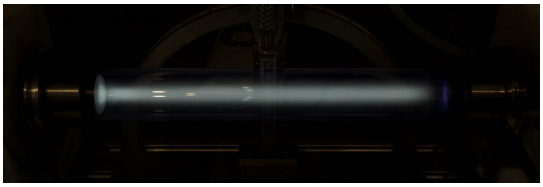

(d) CO_2-Ar discharge at 38 mbar

Figure 4.12: CO_2 discharge with 30 mbar argon admixture at 2 kW with different partial pressures of CO_2

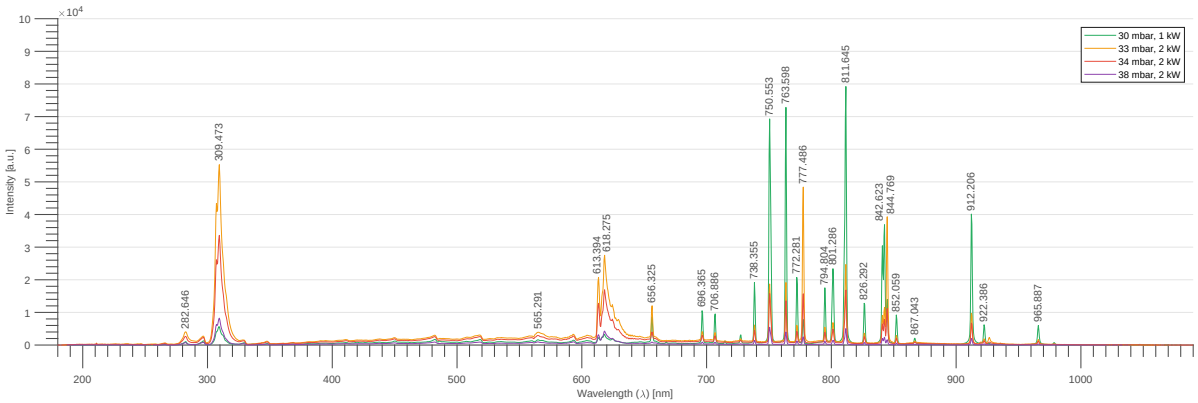

Figure 4.13: Spectrogram CO_2 with 30 mbar Ar admixture at various filling pressures

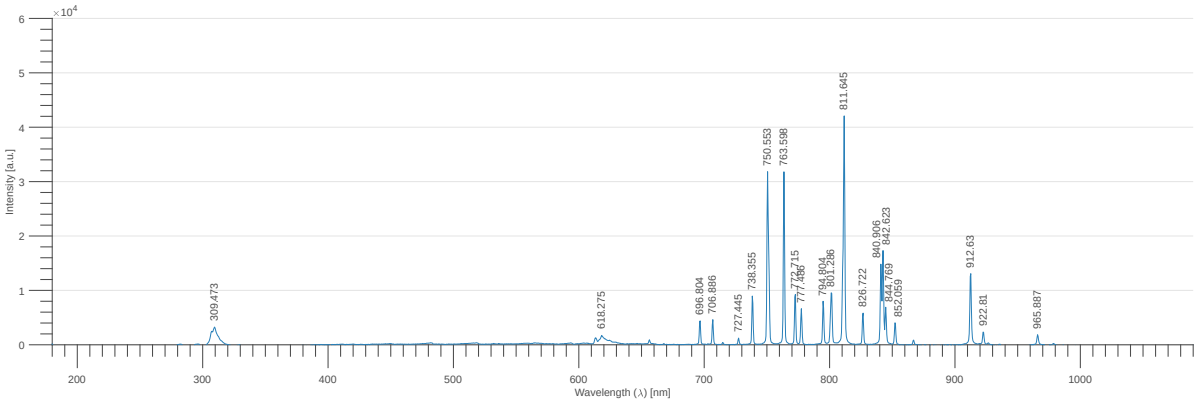

Figure 4.14: Spectrogram CO_2 with 100 mbar Ar admixture at 102mbar, ISO400, 1/30s, f5.6

mbar background pressure the filling time was reduced to 60 seconds and at 100 mbar it was reduced to 30 seconds. Figure 4.15a gives the absolute conversion of CO_2 over time for background pressure of argon at 30 mbar and at 100 mbar. From this Figure it seems likely that the addition of argon to the mixture did increase the conversion slightly. At 30 mbar the absolute conversion rose over time from 44.4% to 49.0% and at 100 mbar from 48.7% to 61.5%. However, this increase in conversion did come at the cost of diluting the mixture. This dilution decreased the effective conversion drastically as shown in Figure 4.15b.

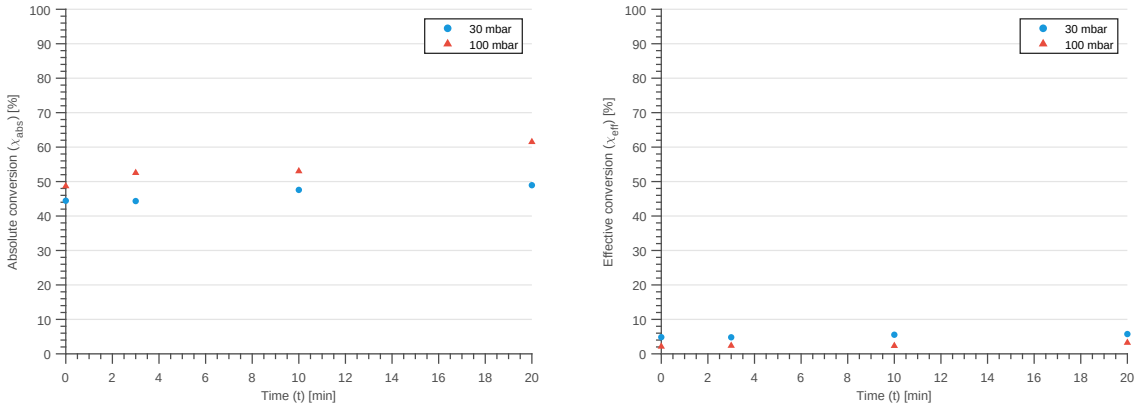

(a) Absolute conversion CO_2 dissociation

(b) Effective conversion CO_2 dissociation

Figure 4.15: CO_2 dissociation in 30 mbar and 100 mbar argon admixture

In conclusion, CO_2 dissociation in the SAPR has shown a reasonable conversion rate paired with a poor energy efficiency. In order to improve the reactor performance argon was introduced as an electron producer. This led to an increase in the absolute conversion. However, the effective conversion drastically dropped due to the dilution of the mixture.

4.3. The effect of a reduced interelectrode gap on a argon discharge

In the previous series of experiments with CO_2, the operational range turned out to be very small and the plasma extinguished by increasing the pressure with only a few mbar. Even with the addition of argon this window remained small. As explained in Section 2.2.3, a plasma extinguishes when the electric field no longer able to ionise the gas. With this information, one may question whether argon can function properly as electron producer in this configuration. Going back to the first experiments with argon, there has been no evidence for the presence of singly ionised argon atoms. A low reduced electric field may be associated with the absence of these ions. This incentivised a reduction in the interelectrode gap. The original, 300mm long reactor tube was replaced by an 120mm long quartz tube of identical diameter. Such a decrease in the interelectrode gap whilst the applied voltage remains constant results in an increase in the electric field. Additionally, it reduces the gas content of the reactor. This reduction in content paired with an increase in the electric field results in a significantly higher reduced electric field. Such an increase in reduced electric field should enable argon to attain its ionisation potential more easily.

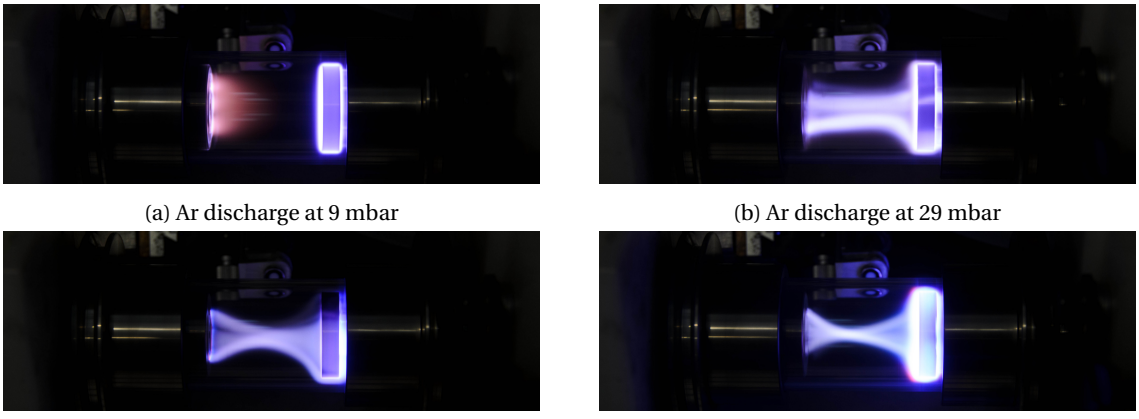

(a) Ar discharge at 9 mbar

(b) Ar discharge at 29 mbar

(c) Ar discharge at 93 mbar

(d) Ar discharge at 163 mbar

Figure 4.16: Argon discharge at various pressures, ISO 400, 1/30 s, f5.6

The effect of the reduced interelectrode gap was investigated experimentally according to the same procedure used in the previous argon experiments. The purpose of this experiment was to gauge whether the reduction in the interelectrode gap would have an impact on the detection of Ar-II emissions. Figure 4.16

presents an argon discharge at various pressures in the short interelectrode gap configuration. Shortly after ignition at about 10 mbar, a glow discharge with a lilac positive column was observed. This behaviour is comparable to the original configuration. However, the Faraday dark space near the cathode occupied a significant larger portion of the discharge length. As pressure increased, the plasma transitioned into a violet, contracted plasma. This contracted plasma appeared to distribute broadly over the radius of the tube. However, on closer inspection with faster shutter speeds of the camera, a single beam could be observed as shown in Figure 4.17 at two different instances. Further increase in pressure decreased the distribution and intensified the luminosity of the plasma.

(a) Ar discharge, ISO 400, 1/500 s, f5.6 (b) Ar discharge, ISO 400, 1/500 s, f5.6

Figure 4.17: Two representative examples of the Ar plasma captured with faster shutter speeds, ISO 400, 1/500 s, f5.6

4.3.1. Optical Emission Spectroscopy Analysis

The emission spectra were recorded at different pressures in order to evaluate the effect of reducing the interelectrode gap on the argon discharge. The fibre optic cable mount had to be relocated as the distance between both manifolds was too small to accommodate the mount. Due to the relocation of the mount, the tip of the fibre optic cable was positioned differently. It was positioned behind the discharge tube, pointing towards the centre of the discharge tube in the horizontal plane.

Figure 4.18 shows the emission spectrum of a argon discharge at 276 mbar at 1 kW. There were no significant differences observed between the measured spectra in this short configuration in comparison to the original configuration. However, as the applied power was increased to 2 kW, several spectral lines were observed in the 300-700 nm range. More specifically, spectral lines occurred at 334.831 nm, 471.759 nm, 480.803 nm, 614.725 nm, 635.998 nm as is visible in Figure 4.19. These spectral lines correspond to emissions of singly ionised Ar atoms. However, the intensity of these Ar-II spectral lines remained small in comparison the Ar-I spectral lines in the infrared range. The same behaviour could be observed at a lower pressures (data not shown). At first, no significant differences were observed at 1 kW. Again, with the subsequent increase of the applied power to 2 kW, Ar-II spectral lines could be observed in the 300-700 nm range. These results suggest that the reactor is capable to ionise argon in this configuration.

The presence of singly ionised argon lines enabled the determination of the electron density with the Saha equation as described in section 3.4.3. The electron density was determined with the atomic argon line at 750.39 nm and the ion line at 480.80 nm. The electron excitation temperature required to determine the electron density was calculated according to same method as used in section 4.1. According to the two-line method the electron temperature was approximately 1000 K. With this electron temperature and transition parameters given in table 4.4, the electron density was about $7.25 \cdot 10^{-27}$ cm^{-3}, which is extremely low in comparison to literature.

Table 4.4: Selected atomic and ion argon levels with corresponding wavelength and transition probability

Species	λ [nm]	A_{ij} [s^{-1}]	g_i [-]	E_i [cm^{-1}]	E [cm^{-1}]	Reference
Ar-I	750.39	$0.472 \cdot 10^8$	1	108723	127110	[76]
Ar-II	480.80	$0.79 \cdot 10^8$	5	155043	222848	[76]

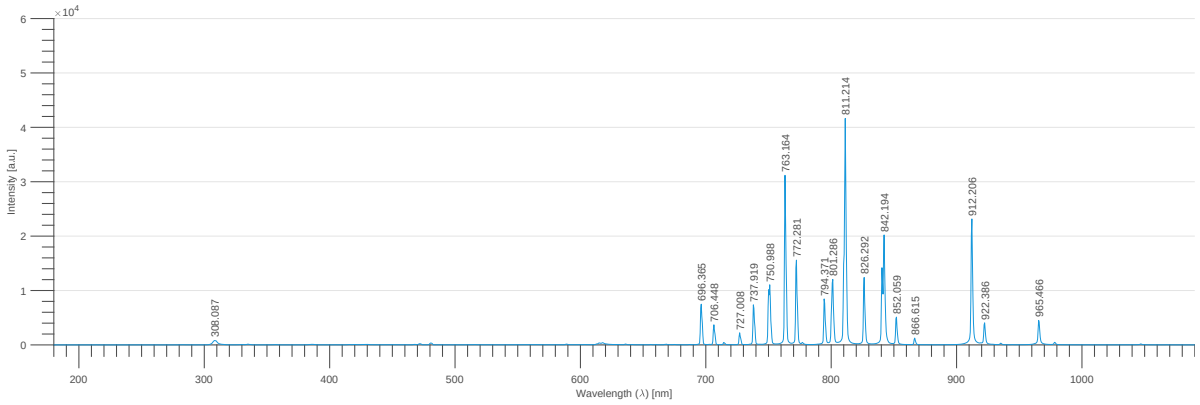

Figure 4.18: Spectrogram Ar at 276 mbar, 1 kW with reduced interelectrode gap

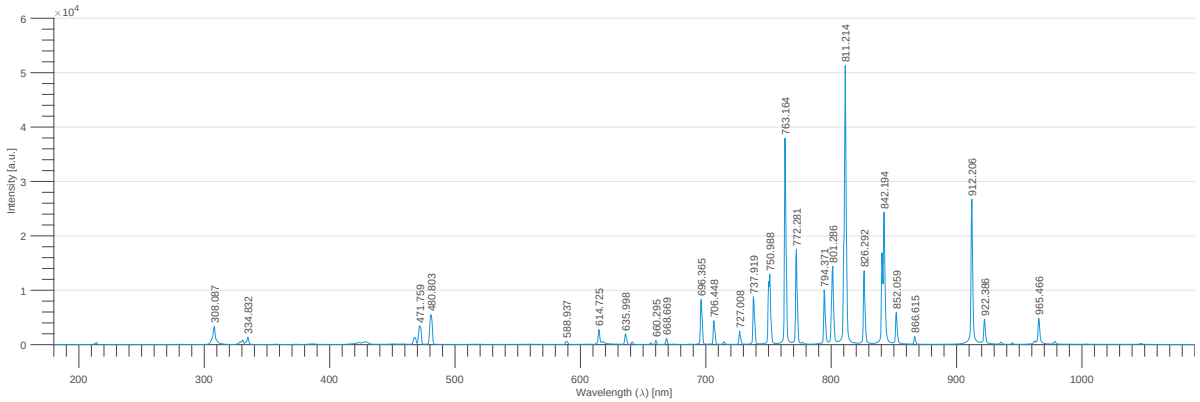

Figure 4.19: Spectrogram Ar at 276 mbar 2 kW with reduced interelectrode gap

4.4. The effect of a reduced interelectrode gap on CO_2 dissociation

The previous argon experiments have shown that a reduction in the interelectrode gap enables the reactor to ionise argon. This experimental investigation assessed the effect of a reduced interelectrode gap on the reactor performance of CO_2 dissociation. The experimental procedure has remained identical to the previous CO_2 experiments.

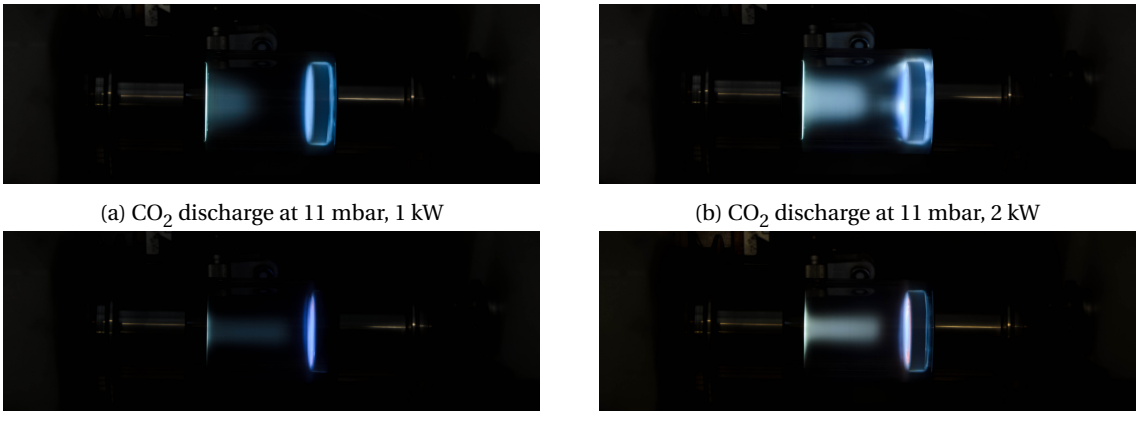

(a) CO_2 discharge at 11 mbar, 1 kW

(b) CO_2 discharge at 11 mbar, 2 kW

(c) CO_2 discharge at 30 mbar, 1 kW

(d) CO_2 discharge at 30 mbar, 2 kW

Figure 4.20: CO_2 discharge at various pressures; ISO400, 1/30s, f5.6

Figure 4.20 presents a CO_2 discharge at various pressures and applied power levels. After ignition at 10 mbar, a faint, green glow discharge could be observed. As pressure elevated the discharge contracted and the

luminosity declined. In contrast to previous experiments with the original configuration, the pressure could be elevated to 60 mbar before the plasma extinguished. However, it is important to bear in mind that this configuration contained a lower amount of CO_2 due to reduction in reactor volume. More strikingly is the effect of an increase in applied power. The plasma significantly increased in luminosity upon elevating the applied power from 1 kW to 2 kW. At 2 kW the discharge could be sustained until the pressure rose above 70 mbar. Over the course of these experiments, the cathode would rapidly heat up within a few minutes and started to emit an incandescent glow as shown in figure 4.21.

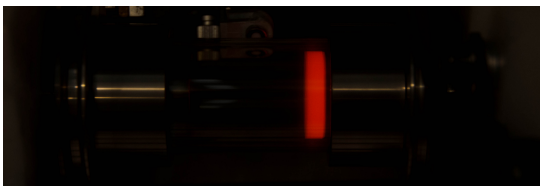

Figure 4.21: Incandescent glow of the cathode, after the plasma extinguished; ISO400, 1/30s, f5.6

4.4.1. Optical Emission Spectroscopy Analysis

The recorded spectra of the CO_2 plasma at 10 mbar are visible in Figure 4.22 for both applied power levels. In contrast to previous findings, the spectra were dominated predominantly by C_2 and CO spectral lines. The most interesting aspect of this graph is the suppression of OH spectral lines at 308.9 nm in comparison to the original configuration. Instead excitation of atomic oxygen lines at 777.05 and 844.34 nm were the most intense spectral lines. Furthermore, whereas the intensity of CO^+ ($A^2\Pi_g \rightarrow X^2\Sigma$) previously dominated the visible to near-infrared range, the intensity of these lines has declined substantially in comparison to the intensity of the C_2 swan bands. As observed previously, the spectrum elevated in the 300-700 nm range albeit considerably more in this configuration, especially at 2 kW. This presumably arose due to a collection of superimposed C_2, CO and CO_2 spectral lines. In general, the spectral lines have remained largely similar to previous results. However, the distribution of intensity of these lines is significantly different in the short configuration from previously observed spectra.

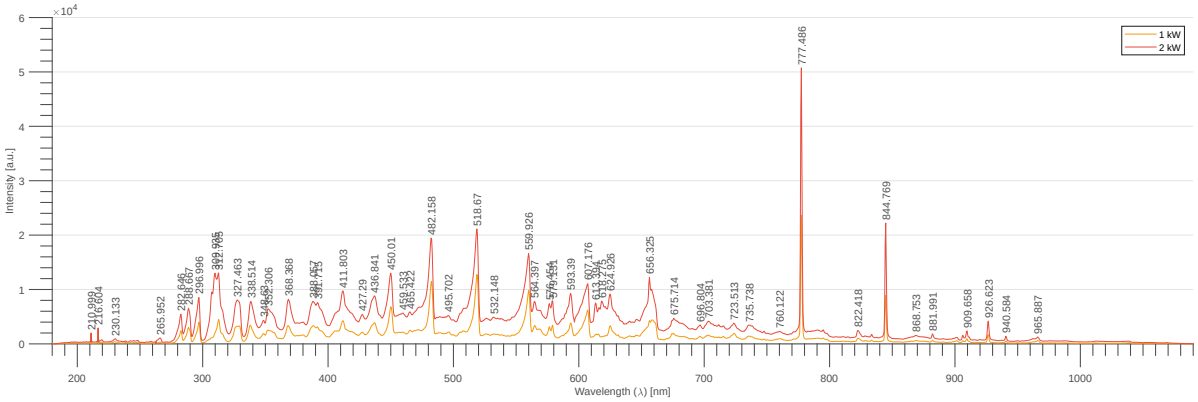

Figure 4.22: Spectrogram CO_2 with 10 mbar at different power levels

4.4.2. Reactor Performance Evaluation

The main purpose of this experimental investigation is to assess the effect of the reduction in the interelectrode gap on the reactor performance. The experimental procedure has remained identical to the previous measurements although significantly higher pressures could be attained. Figure 4.23 shows the absolute conversion and the energy efficiency of the reactor as function of the specific energy input at various pressures and applied power levels.

In these figures, a familiar pattern can be observed, where an increase in the specific energy input leads to an increase in the absolute conversion although at the cost of a reduction in the energy efficiency. This behaviour is demonstrated clearly in Figure 4.24. The highest conversion was achieved at 10 mbar and 2 kW, reaching conversions of 30% to 55%. However, this point corresponds to the lowest energy efficiency as well,

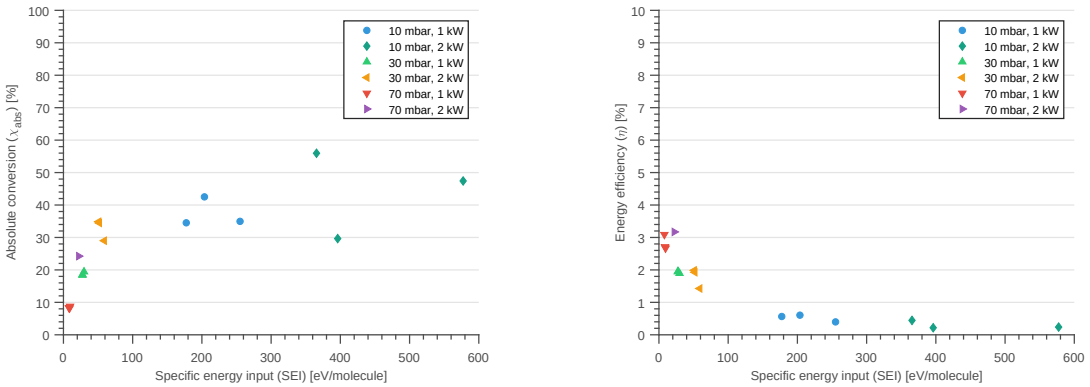

(a) Absolute conversion CO_2 dissociation

(b) Energy efficiency CO_2 dissociation

Figure 4.23: Reactor performance of the short configuration for CO_2 dissociation at various pressures and applied power levels.

attaining solely about 0.25%. The highest energy efficiency was achieved at 70 mbar and 2 kW, amounting to 3.09%.

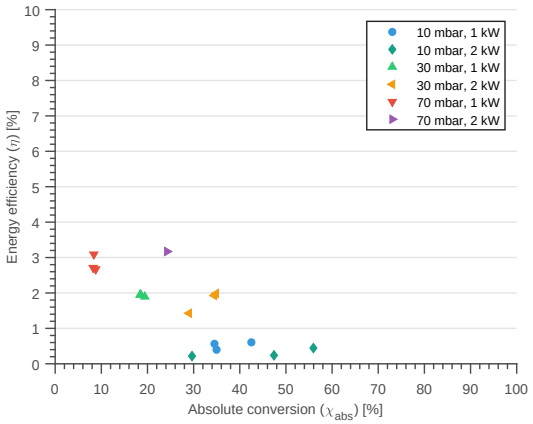

Figure 4.24: Energy efficiency of CO_2 dissociation as function of the conversion

The effect of pressure and applied power are reflected by the effect of the specific power input. Since an increase in applied power at constant pressure increases the specific power input, this results in increased conversion and decreased energy efficiency. Conversely, an increase in pressure elevates the number density of gas, this decreases the specific power input when the applied power remains constant. Additionally, in this experimental setup the pressure is correlated to the flow rate. The effect of the flow rate on the reactor performance was investigated experimentally. Figure 4.25 presents the absolute conversion and energy efficiency as a function of the flow rate at constant pressure and applied power. What can be clearly seen in these figures is the increase in energy efficiency and decline in conversion with increasing flow rates.

4.4.3. Benchmarking reactor performance for CO_2 dissociation

Figure 4.26 presents an overlay of the reactor performance results, previously presented in figure 4.23, compared to the different plasma configurations reviewed by Snoeckx and Bogaerts. Compared to other plasma configurations, the absolute CO_2 conversion is reasonable, outperforming most GA, DBD & Other reactor configurations. On the other hand, MW and RF plasma are able to achieve significantly higher conversion rates of up to 90 % at similar energy efficiencies. In comparison to all other plasma configurations, the energy efficiency of this reactor is poor and far below the efficiency target set by Snoecks and Bogaerts. GA and MW plasmas are able to achieve similar conversion rates at far higher energy efficiencies. Whilst the energy efficiency of DBD configuration is on par with this reactor, DBDs operate at atmospheric pressure. As such, DBDs are able to operate at higher mass flow rates.

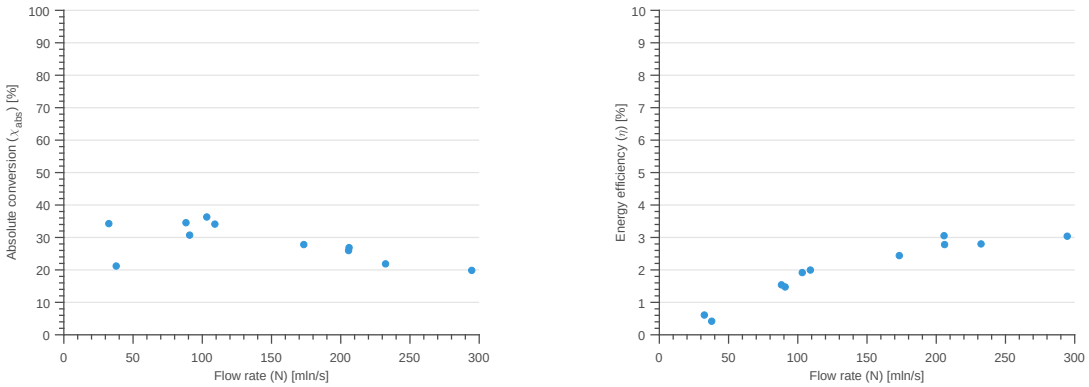

(a) Absolute conversion CO_2 dissociation.

(b) Energy efficiency CO_2 dissociation.

Figure 4.25: Reactor performance for CO_2 dissociation at 2 kW and 10 mbar for various flow rates.

Taken together, this reactor has a reasonable conversion with a poor energy efficiency. Additionally, this reactor performs below the thermal equilibrium limit and efficiency target. The former probably suggest that this configuration did not favour the most energy efficient channel. The consequence of the latter is that this reactor in its current configuration is not viable to compete with electrolysis.

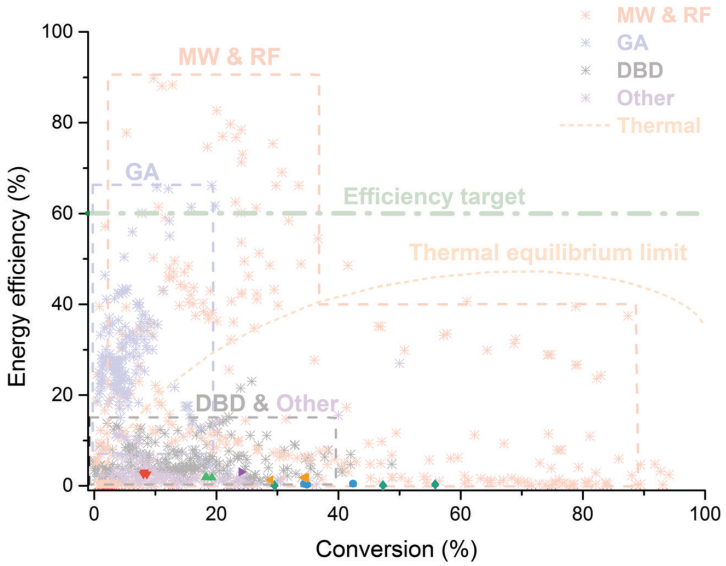

Figure 4.26: Same as Figure 2.11, overlayed with results shown in Figure 4.24

5

Discussion

In this thesis we have explored the properties and abilities of the SAPR. Using argon as a non-reactive medium the relation between plasma parameters and system variables was characterised. Optical emission spectroscopy measurements suggested that the electron temperature increased with higher pressure and power. The electron temperature did not change by increasing either the rotational speed or the gas feed rate. Argon spectral lines were mostly concentrated in the red to near-infrared region. Spectral lines of singly ionised argon were only detected upon increasing the reduced electric field by decreasing the inter-electrode gap.

In subsequent experimentation, the reactor performance of CO_2 dissociation was measured to benchmark the SAPR against other existing plasma configurations. The reactor performance was expressed in the conversion and energy efficiency as a function of pressure, power and flow rate. The maximum conversion of about 30% to 55% was achieved at an energy efficiency of approximately 0.25 %. The maximum energy efficiency of about 3% was achieved at a conversion of approximately 8.5% conversion. In general, CO_2 discharge proved to be difficult to sustain. Upon decreasing the inter-electrode gap, the operation of the discharge was improved and reactor performance was not significantly altered. Comparison to other discharge configurations showed that the SAPR had a reasonable conversion and poor energy efficiency.

This discussion section covers the following main topics: first, the experimental results and the implications for the plasma performance will be discussed, as well as the differences between argon and CO_2 behaviour. Then, the current experimental setup will be reviewed. Last, after benchmarking this reactor against other configurations, a number of recommendations will be given.

The denotation of the molecular term symbol has been omitted in the following section for the ground states of $CO(^1\Sigma^+)$, $CO_2(^1\Sigma^+)$ and $O(^3P)$.

5.1. Argon plasma behaviour

The analysis of the argon emission spectra with the two-line method indicates that the electron temperature rises with the filling pressure. This finding was unexpected as, in general, a rising pressure would increase the number of collisions between electrons and heavy particles [69]. Such a reduction in the mean free path of the electrons would increase the transfer of energy from electrons to heavy particles [69]. As a consequence of this distribution of energy, the gas temperature would rise and the electron temperature would lower [69]. In contrast, a slight increase in electron temperature with rising pressure was observed. Perhaps the observed rise in electron temperature was due to the sequential execution of the experiments. This sequence of experiments could have increased the gas temperature by thermalising heavy particles by electron impact. Presumably, electron collisions with these thermalised heavy particles caused this rise by shifting the EEDF towards higher excitation temperatures.

Likewise, the results of the two-line method showed a rise in the excitation temperature with increasing applied power. In previous studies, the power input has been found to have little effect on the electron temperature [77, 78]. In fact, increasing the power input is known to increase the electron density instead. Therefore, the findings of the current study do not support the previous research. This finding could have been an artefact of the measurements devices. However, one study did observe such an increase in electron

temperature [79]. A possible explanation for this can be that increasing the electron density led to increased gas heating. This gas heating enabled gas density changes, which could drive the heavy particles to the periphery, leading to a higher reduced electric field and thereby higher electron temperatures than at lower applied power levels.

The spectrometer did not detect any evidence for the presence of singly ionised argon. It was suggested that the noticeable absence of Ar-II spectral lines stemmed from a low reduced electric field. Another possible explanation for this observation can be provided by the work of Garamoon et al. [80]. Garamoon et al. recorded the emission spectra of both the positive column and the negative glow region from a low pressure argon glow discharge. Their results showed that the spectral lines of emission in the negative glow region were more intense than in positive column [80]. Furthermore, they clearly noticed the appearance of Ar-II in the negative glow region whereas they hardly detected any Ar-II lines in the positive column [80]. They argued that the observed intensity difference stemmed from an increased collision probability as a consequence of the higher electron temperature and electron density in the negative glow region [80]. This supports the observation of a blue hue near the cathode in the current setup. Such emissions of blue visible light in the 400-485 range imply the presence of Ar-II emissions [65]. Furthermore, most ions should be present in the cathode fall, where ionisation rather than excitation is the main collision process [8]. As a consequence, no light was emitted from the cathode fall and thus were these ions not detected by the emission spectroscopy [8].

Another line of evidence for the presence of argon ions in the cathode fall and negative glow regions could be observed when looking at the effects of the plasma on the reactor. As explained in chapter 3, the previously installed wolfram electrodes detached from the service assembly upon subjection to the plasma. This detachment occurred due to the failure of the press fit as the electrodes and the service assembly were disproportionately subjected to thermal expansion. Such a thermal expansion was almost certainly induced by the ion bombardment. Once the wolfram electrode was replaced with a stainless steel electrode, a deposition near the cathode was observed over time. The subjection of the electrode to ion bombardment may have induced sputtering. The ejected solid particles could deposit on the discharge walls, producing the deposition. Besides sputtering, oil residue was observed on the internals of the service assembly. The residue may stem from a leaking oil seal or could have entered the vacuum chamber when the service assembly was inserted in the manifold block. Traces of this oil residue could have been entrained in the gas flow and subsequently dissociated in the plasma. The product formation of this dissociation could have deposited on the discharge walls. The thin deposition film has not been further studied and the composition of the deposition remains unknown at this point in time.

5.2. Reactor performance of CO_2 dissociation

Analysis of the emission spectra of CO_2 revealed a collection of particles related to the dissociation of CO_2. More specifically, emissions of CO, CO^+, C_2, O and O_2 were detected. These particles are commonly generated in plasmas with electronic impact excitation-dissociation as the predominant dissociation mechanism [7, 81, 82]. These particles were observed due to the emissions of the following systems: fourth positive system of CO($A^1\Pi \rightarrow X^1\Sigma$), third positive system of CO($b^3\Sigma \rightarrow a^3\Pi$), Herzberg system of CO($C^1\Sigma \rightarrow A^1\Pi$), Ångström system of CO($B^1\Sigma \rightarrow A^1\Pi$), comet-tail system of CO^+($A^2\Pi \rightarrow X^2\Sigma$) and Swan system of C_2($A^3\Pi_g \rightarrow X'^3\Pi_u$). In addition to the molecular emissions of CO_2 derivatives, emissions of atomic and molecular oxygen ($b^1\Sigma_g^+ \rightarrow X^3\Sigma_g^-$) were observed.

As mentioned previously, the emissions in the Swan system are responsible for the green colour of the plasma and indicate the formation of carbon either from CO_2 or CO [11]. The detected C_2 almost certainly formed upon the combination of carbon atoms [11]. Based on her results, Spencer argued that the formation of C_2 through the direct dissociation of CO_2 according,

$$CO_2 \rightarrow C + O_2, \qquad \Delta H = 11.5 \text{ eV/molecule} \tag{5.1}$$

would be improbable due to requirement for high energy electrons [11]. Instead, she argued that it would be far more likely that carbon formation would occur through disproportioning,

$$CO + CO \rightarrow CO_2 + C, \qquad \Delta H = 5.5 \text{ eV/molecule} \tag{5.2}$$

as this pathway has a considerably lower energy threshold [7, 11]. However, in contrast to Spencer's study, the current study detected emissions related to the transition of O_2($b^1\Sigma_g^+ \rightarrow X^3\Sigma_g^-$). It may have been possible

that the $O_2(b^1\Sigma_g^+)$ population was formed by electron impact dissociation of CO_2 according to [81],

$$e + CO_2 \rightarrow C + O_2(b^1\Sigma_g^+) + e \tag{5.3}$$

Probably, both mechanisms occurred in tandem as disproportioning can be accelerated via electronic excitation through the excited $CO(a^3\Pi)$ according [7],

$$CO(a^3\Pi) + CO \rightarrow CO_2 + C \tag{5.4}$$

The presence of a $CO(a^3\Pi)$ population is suggested by the emissions in the detected third positive system of $CO(b^3\Sigma \rightarrow a^3\Pi)$. As $CO(a^3\Pi)$ is a meta-stable level, it has a longer lifetime than ordinary excited states. Therefore, it is plausible that the acceleration of disproportioning through $CO(a^3\Pi)$ occurred in this system. Nonetheless, the rapid reverse reaction according,

$$C + CO_2 \rightarrow CO + CO \tag{5.5}$$

is likely to limit the formation of carbon and can only be hampered by cluster formation in the discharge volume or on the walls [7, 11].

In plasmas with electronic excitation by electron impact as the primary dissociation mechanism a signification contribution of the formation of the metastable $CO(a^3\Pi)$ through,

$$e + CO_2 \rightarrow CO(a^3\Pi) + O + e \tag{5.6}$$

is expected [7]. This should entail a significant population of the metastable $CO(a^3\Pi)$. However, the Cameron bands of $CO(a^3\Pi \rightarrow X^1\Sigma)$ were not identified in the recorded spectra. This suggests that these lines were either obscured by other, more intense lines or the population of the metastable is depleted through other mechanisms than radiative de-excitation. The previously stated acceleration of disproportioning is one of such depletion mechanisms. Another possible mechanism of $CO(a^3\Pi)$ population is through the dissociation process of CO_2 according,

$$CO_2 + CO(a^3\Pi) \rightarrow CO + CO + O \tag{5.7}$$

this would harbour a limited improvement to the energy efficiency as the energy of the excited metastable is absorbed in the dissociation process [7].

Besides the formation of $CO(a^3\Pi)$, emissions in the fourth positive system of CO suggest the presence of a $CO(A^1\Pi)$ population. This population could have been formed by electron impact excitation of CO_2 according [83],

$$e + CO_2 \rightarrow CO(A^1\Pi) + O + e \tag{5.8}$$

Although the same $CO(A^1\Pi)$ population could have been formed by the direct excitation of CO according,

$$e + CO \rightarrow CO(A^1\Pi) + e \tag{5.9}$$

as well [83]. It is not readily apparent from the emission spectra which one is the predominant mechanism and the presence of one does not necessarily exclude the other. Actually, it is far more likely that the population arose due to a conglomerate of both mechanisms. In case of emissions in the Ångström system, recent research has suggested that $CO(B^1\Sigma)$ is predominantly formed through the direct excitation of ground state CO by electron impact according [38, 84],

$$e + CO \rightarrow CO(B^1\Sigma) + e \tag{5.10}$$

The above equation clearly shows the loss of energy in the system as an electron is absorbed to electronically excite a CO molecule which upon de-excitation releases a photon.

$$CO(B^1\Sigma) \rightarrow CO + h\nu \tag{5.11}$$

It is reasonable to assume that this photon will not be used in photo-ionisation as the plasma is presumably optically thin and therefore the energy contained in this photon is lost.

Another significant aspect of the recorded spectra were the emissions in the comet-tail system of $CO^+(A^2\Pi \rightarrow X^2\Sigma)$. These emissions imply the presence of a $CO^+(A^2\Pi)$ population which could have been formed by [81],

$$e + CO_2 \rightarrow CO^+(A^2\Pi) + O + 2e \tag{5.12}$$

As previously discussed, the electrodes detached due to thermal expansion that was induced by ion bombardment. Originally, this occurred with the cathode after subjection to an argon plasma. However, as soon as the reactor was subjected to a CO_2 plasma the anode would fail as well. The anode can only be subjected to the impact of negative ions. Therefore, the failure of the anode presumably heralds the presence of negative oxygen ions. Such negative oxygen ions can be formed upon dissociative electron attachment of CO_2,

$$e + CO_2 \rightarrow CO + O^- \tag{5.13}$$

although it has been reported that the contribution towards the total kinetics is not significant [7].

Based on the findings above, it could be hypothesised that electron impact excitation-dissociation is the dominant CO_2 dissociation mechanism. This finding was also reported by Fridman based on the experimental results of Ivanov, Polak and Slovetsky [7]. It is now well established from a variety of studies that electron impact excitation-dissociation is not an energy efficient mechanism [5, 7]. First of all, the required electron energy to achieve dissociation significantly exceeds the carbon-oxygen bond energy [7]. Second, as the diversity of mechanisms listed above demonstrates, the high electron temperatures present lead to the simultaneous excitation of numerous other states of the various particles [7]. Most of these excitations are either not relevant or not efficient for the dissociation of CO_2 [7].

Provided that electron impact excitation-dissociation is the dominant dissociation mechanism, the increased effective conversion of the CO_2-argon mixture can be understood. Ramakers et al. showed that a CO_2/Ar plasma has a higher mean electron energy than a pure CO_2 plasma [59]. They argue that this phenomena arises due to the higher energy threshold for inelastic collisions with Ar particles. This higher energy threshold reduces electron energy losses [59]. Besides a higher mean electron energy, Ramakers et al. found that the electron density is higher in a CO_2/Ar plasma than a pure CO_2 plasma [59]. As the rate of electron impact excitation-dissociation is dependent on the mean electron energy and electron density, a higher effective conversion for the CO_2/Ar mixture is expected and indeed observed in this system.

5.3. Differences between argon and CO_2 plasma behaviour

Even though both discharges were a characteristic glow discharge, they were significantly different from each other in several respects. Two main differences will be discussed in this section: the plasma collapse of a CO_2 discharge at elevated pressure and the constriction of the argon plasma.

In general, when both pressure and electric field are similar, gases are exposed to the same reduced electric field. In this study, however, it proved to be difficult to sustain a CO_2 plasma in similar conditions as an argon plasma. It has been reported that the mean electron energy is far higher in argon than in a CO_2 [59]. This means that the high energy tail of the EEDF in an argon plasma has a far larger population than a CO_2 plasma. As pressure is increased, the EEDF contracts and the population in the high energy tail falls. A plasma collapses once the electron population is no longer able to ionise the gaseous medium. This mean electron energy threshold is met at lower pressures in a CO_2 plasma than an argon plasma as the mean electron energy in a CO_2 plasma is lower in general. Therefore, a CO_2 plasma collapses at conditions an argon plasma would be able to sustain itself.

Glow discharge contraction as observed in the argon plasma is primarily caused by thermal instability and to a lesser extent by step-wise ionisation and Maxwellisation instabilities [8]. These instabilities affect the growth rate of the electron population, which is the main cause for contraction [8].

The most dominant instability, thermal instability, is the result of a strong non-linear dependence of the ionisation rate on the reduced electric field [8]. Non-homogeneous heating of the gas on the tube axis leads to the development of a local temperature rise [8]. The gas density starts to decrease upon a rising temperature, driving neutral particles to the boundary [8]. This density change increases the local reduced electric field on the tube axis [8]. As a consequence of the strong non-linear dependence of ionisation rate, the electron density sharply inclines upon a local increase in the reduced electric field [8]. Finally, a higher local electron density raises the collision rate which leads to further heating of the gas and closing the chain [8]. In a similar manner, step-wise ionisation instability describes the effect of an additional excited species population as a consequence of local electron density rise [8]. The presence of an increased number of excited species leads to faster ionisation and in turn a rise in electron density [8]. Lastly, Maxwellisation instability describes the

development of the high energy tail of the EEDF as a result of local electron density rise [8]. Here, higher electron energies lead to faster ionisation rates and further increase of the electron density.

In this study, plasma constriction was only observed for argon plasmas. A possible explanation as to why this was solely observed for an argon plasma is given by Fridman and Kennedy. They argue that in contrast to monoatomic gases, electron density variations in molecular gases do not directly result in gas heating but instead heating occurs through intermediate vibrational excitation [8]. VT-relaxation is relatively slow which tempers the instability mechanism [8].

It is arguable whether the observed constriction of the plasma on the tube axis is desirable. Recent studies have sought to limit constriction as it solely serves to thermalise the plasma. Van Rooij et al. demonstrated that the transition from a diffuse to contracted regime led to a gas temperature rise from about 2000 K to 14000 K [40]. This decay of the non-thermal equilibrium significantly alters the conditions of the plasma in a non-beneficial way, as discussed before. Besides the significant changes to the plasma conditions, constriction introduces a non-homogeneity in the distribution of the plasma. Snoeckx and Bogaerts argued that such inhomogeneous distribution is limiting conversion in GA plasmas [5]. In this study, no evidence was found that the rotation of the reactor-electrode distributes the plasma over a broad range. Instead, it solely seemed to serve to constrict an otherwise buoyancy-driven upward drift to the tube's axis. One could argue this would only encourage contraction. As Fridman and Kennedy stated: '...optimal conditions necessary for high efficiency of chemical processes are not always the same as the conditions necessary for stability and homogeneity of relevant nonthermal discharges' [8].

5.4. Experimental setup

Previous research has established that electron impact excitation-dissociation is not the most energy efficient dissociation mechanism. This has been mainly attributed to the high electron energy required, as this has to exceed 14 eV/molecule to enable dissociation [11]. Values for the SEI input of this study resided in the 30 to 600 eV/molecule range. In contrast, optimal SEI values for microwave discharges reside in the 0.3-1 eV/molecule range [11]. Hence, it is not surprising that the highest energy efficiency was encountered at the lowest SEI value. Consistent with literature, it was found that with increasing values of SEI conversion increased and energy efficiency decreased. Again, it is therefore not surprising that the highest conversion was encountered at the highest SEI of about 577 eV/molecule. One could argue that in comparison to the reported literature values, such high values for the SEI required to achieve a reasonably high conversion could be considered the moral equivalent of blunt force.

However, the indirect determination of the power dissipated in the plasma imposed limitations on the accuracy of the SEI calculations. One of the main weaknesses of this method was that it did not account for all the losses in the electric circuit, most importantly the losses in the full bridge rectifier circuit. In addition, the electric power consumed by the motor and fan were assumed to remain constant in time but in practice tended to fluctuate. Another source of uncertainty was the requirement for a simultaneous manual read-out of three measurement devices, namely the voltage, current and power consumption measurements. This manual read-out introduced time discrepancies in the calculation. Although this method was inherently safer than direct high voltage measurements, it tended to overestimate the power dissipated in the plasma and thus the actual SEI.

The two-line method used to determine the excitation temperature of the argon plasma is another potential concern. To obtain high accuracy, the ratio of the two spectral lines needs to be strongly dependent on electron temperature [80]. This is obtained by selecting two spectral lines with large differences in transition energy [80]. However, spectral lines with such stark differences in transition energy were not observed and less ideal lines had to be used to determine the excitation temperature. This hampered the accuracy of the two-line method. Likewise, the electron density proved to be inaccurate. Values reported in this study were in the order of 10^{-27} cm^{-3}, whereas literature values usually reside in the order of 10^{12} to 10^{17} cm^{-3}. The Saha equation proved to be rather sensitive to the electron temperature. Hence, an inaccurate electron temperature results in an inaccurate electron density. A more accurate approach would be to utilise multiple lines to establish a Boltzmann plot. The electron excitation temperature can be deduced from the slope of this Boltzmann plot.

Over the duration of the experiments it proved to be hard to reproduce the exact same conditions in the plasma. This was mostly due to manual operation of the feed flow rate to achieve the desired pressure. One major drawback of this approach was the direct coupling of flow rate and pressure. By raising the pressure,

the flow rate raised as well. Therefore, the effect of the pressure on the system could not be studied in isolation. Similar concerns rise with the method of sequentially measuring different pressures. Stabilisation and thermalisation of the plasma in time could have affected the measurements of the electron temperature. Although at times the same conditions could be achieved, the time it took to achieve these conditions would vary largely. In addition, the pressure was measured by the pump and not directly in the reactor-electrode assembly, which were not necessarily the same.

With these measurement inaccuracies in mind, the results of the present study should be considered as a qualitative assessment of the plasma behaviour and reaction mechanism as starting point for a more accurate and comprehensive approach.

5.5. Comparison to different discharge configurations

The evidence outlined in this discussion suggests that the main mechanism for CO_2 dissociation in this plasma configuration is electron impact excitation-dissociation. These findings, while preliminary, have important implications on the reactor performance as discussed in section 5.2. Knowing this, it would be more fair to compare the reactor to DBD and other DC glow discharges configurations and not to MW and GA plasmas as done earlier in this thesis. These latter two are able to exploit the vibrational excitation channel to dissociate CO_2. This difference in dissociation mechanism explains the relatively poor energy efficiency of the current configuration, as the vibrational excitation channel has far superior energy efficiency performance. DBD and other DC glow discharges have a similar dissociation mechanism as the SAPR. Compared to these configurations the energy efficiency of this reactor is on par with their performance.

Consistent with the literature, this study found that the reactor performance was limited in either conversion or energy efficiency, where increasing either one led to the decrease of the other. High conversion rates of about 30% to 55% were encountered at high values of specific energy input. Conversely, the best energy efficiency results of about 3% were encountered at the lowest specific energy input. The specific energy input of this configuration was relatively high in comparison to values reported in the literature. Increasing the reduced electric field by reducing the inter-electrode gap led to an even further increase of the specific energy input. The reduced electric field affects the distribution of the electron energy. Figure 5.1 presents the effect of the reduced electric field on the distribution of the input energy over the various mechanisms. The current configuration seems to operate in the same region as DBD configurations. Operating the plasma at this point distributes a large fraction of the energy to electronic excitation, which does not contribute effectively to dissociation. To improve energy efficiency, operating at a lower reduced electric field would enable to dissociate CO_2 through the more favourable vibrational excitation channel. However, with the current plasma configuration, the plasma could not be sustained at lower values of the reduced electric field.

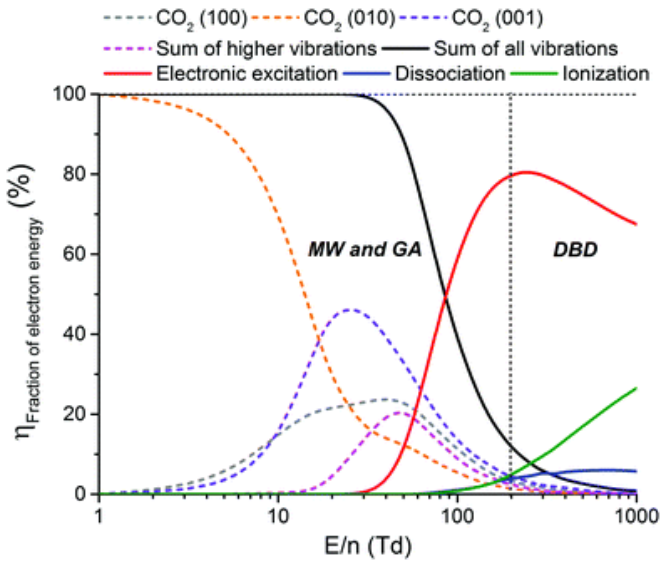

Figure 5.1: Electron energy distribution over the different mechanisms as a function of the reduced electric field (E/N). Adopted from [5]

6

Conclusion

This thesis explored the properties and applications of the SAPR, a novel plasma reactor configuration characterised by the rotational confinement and stabilisation of the plasma. Using a non-reactive and reactive species, argon and CO_2 respectively, the relationship between the system parameters and plasma parameters, and the relationship between these system parameters and the reactor performance were established. Optical emission spectroscopy measurements suggested that, for argon, the electron temperature increased with higher pressure and power and not with flow rate and rotational speed of the reactor assembly. The other plasma parameters, the gas temperature and the electron density could not be calculated. The reactor performance for CO_2 dissociation was expressed as the conversion and the energy efficiency. The conversion decreased with increasing flow rate and pressure, and increased with increasing power. In contrast, the energy efficiency increased with increasing flow rate and pressure, and decreased with increasing power. The maximum conversion of about 30% to 55% was obtained at an energy efficiency of approximately 0.25% and the maximum energy efficiency of about 3% was achieved at a conversion of approximately 8.5% conversion. Comparison to other discharge configurations showed that the SAPR has a reasonable conversion with a poor energy efficiency. The performance is on par with DBD but outperformed by MW and GA configurations.

The evidence outlined in the discussion suggests that the main mechanism for CO_2 dissociation in this plasma configuration is electron impact excitation-dissociation. The reactor performance of the SAPR is on par with other plasma configurations with the same dissociation mechanism. However, it is nowhere near the energy efficiency target set for plasma-chemical conversion of CO_2 to compete with electrochemical conversion. With the limitations imposed by the current dissociation mechanism, it is unlikely that any future improvements would be sufficient to achieve the energy efficiency target that has been set. The conditions of plasma currently achievable with the SAPR are unsuitable for the energy-efficient conversion of CO_2 and in order to succeed, as with any plasma-chemical reactor, it needs to be tailored to generate the precise conditions suitable to increase energy efficiency and conversion. To run the SAPR energy efficiently, the discharge itself most likely has to be changed to enable the far more energy efficient vibrational excitation channel.

Nevertheless, the rotational confinement remains an interesting potential of this reactor. Not because of the plasma conditions it enables but the potential to insert a liquid film which could allow for the in-situ removal of reaction products. Previous studies have shown time and time again that every plasma-chemical reactor is either limited in conversion, energy efficiency or flow rate. This study showed that the SAPR is not an exception. However, the in-situ removal of reaction products shifts the equilibrium in favour of product formation, enabling an energy efficient discharge to drive its conversion by shifting the equilibrium. Regardless of its energy efficiently, this configuration is able to investigate the potential of the rotational confinement based on the results and conclusions of this study.

6.1. Recommendations

This study has established that the predominant dissociation mechanism is electron impact excitation dissociation. Further studies, aiming to improve energy efficiency, should seek to reduce the reduced electric field to shift to vibrational excitation-dissociation as the predominant mechanism. Sustaining the plasma at such low values of the reduced electric field will prove to be difficult. At such low values of the reduced electric field the plasma is not self-sustained. As the process of plasma stabilisation by mechanical rotation

does not necessarily require a discharge between two electrodes, future work could consider an alternative discharge mechanism, for example a microwave discharge. Still the question remains what the exact benefit of rotational stabilisation is on the behaviour of the plasma.

Another promising line of research is to establish the viability of sustaining a plasma in the presence of a liquid film. This liquid film could enable the in-situ separation of reaction products, thereby shifting the equilibrium in favour of product formation. This would enable plasma-chemical reactions to achieve the same conversion at a higher energy efficiency. A consideration that should be taken into account is the selection of the film. A liquid should either have a low vapour pressure at reduced pressure or the plasma should be able to operate at atmospheric conditions. Future work should also consider that such a liquid film would hinder the line of sight, thus rendering it difficult to perform optical emission spectroscopy.

With regard to the quality of measurements, a number of improvements have been identified. Increasing the resolution of the spectrometer to at least 0.5 Å enables the distinction of the individual rotational lines. This would enable future research to investigate the gas temperature of the plasma. Calculations of the electron temperature can be improved by expanding upon the two-line method. Instead of using a single pair of transition lines, multiple pairs would be used in a Boltzmann plot technique. The electron temperature can be determined from the slope in the Boltzmann plot as outlined in the work Gordillo-Vazquez et al [85]. Further improvement could be achieved by an absolute spectral radiance calibration with a source with known radiance profile supported by a collisional-radiative model to gain more insight in the population densities of the various states [62].

The determination of the specific energy input can be improved by directly measuring the current and potential over the plasma. Moreover, the current can be used to determine the electron density. Inline positioning of the gas chromatograph eliminates sample bag handling, which could avoid contamination of the samples with air. Automatic readout of measurement devices should eliminate the time discrepancies that can distort the calculation of the specific energy input. Furthermore, improvement can be made by independent pressure measurements directly in the vacuum chamber. A flow controller in the feed line would allow for more accurate flow manipulation and reduce the time it costs to attain the same conditions. Reducing this time will improve the reproducible of the plasma conditions.

A practical consideration in the current construction concerns the three holes that were drilled in the electrode to mount the revised electrodes to the service assembly. These holes introduced distortions in the electric field near the edge of the cavity. These local distortions attract the plasma to edge of the cavity instead of in the middle of the electrode. This may introduce entry effects of which the consequences for the plasma are currently unknown.

Bibliography

[1] Frankfurt School-UNEP centre. Global trends in renewable energy investment 2017. 2017.

[2] I. Wilson, A. Grant, and P. Styring. Why synthetic fuels are necessary in future energy systems. *Frontiers in Energy Research*, 5:19, 2017.

[3] E.I. Koytsoumpa, C. Bergins, T. Buddenberg, S. Wu, Ó. Sigurbjörnsson, K.C. Tran, and E. Kakaras. The challenge of energy storage in europe: Focus on power to fuel. *Journal of Energy Resources Technology*, 138, 2016.

[4] P. schmidt, V. Batteiger, A. Roth, W. Weindorf, and T. Raksha. Power-to-liquids as renewable fuel option for aviation: a review. *Chemie Ingenieur Technik*, 90(1-2):127–140, 2018.

[5] R. Snoeckx and A. Bogaerts. Plasma technology - a novel solution for CO_2 conversion? *Chemical Society Reviews*, 46:5805–5863, 2017.

[6] A. Lebouvier, S.A. Iwarere, P. d'Argenlieu, D. Ramjugernath, and L. Fulcheri. Assessment of carbon dioxide dissociation as a new route for syngas production: A comparative review and potential of plasma-based technologies. *Energy & Fuels*, 27(5):2712–2722, 2013.

[7] A. Fridman. *Plasma Chemistry*. Cambridge University Press, 2008.

[8] A. Fridman and L.A. Kennedy. *Plasma Physics and Engineering*. Taylor & Francis, 2004.

[9] J. Reece. Roth. *Industrial Plasma Engineering*, volume 1. Institute of Physics Publishing, 1995.

[10] S.H. Moreno Wandurraga. Reduced reaction kinetics model for CO_2 dissociation in non-thermal microwave discharges: a non-equilibrium distribution averaged kinetic model for multidimensional simulations. Master's thesis, Delft University of Technology, 2015.

[11] L.F. Spencer. *The study of CO2 Conversion in a microwave plasma/catalyst system*. PhD thesis, University of Michigan, 2012.

[12] A. Bogaerts, E. Neyts, R. Gijbels, and J. Van der Mullen. Gas discharge plasmas and their applications. *Spectrochimica Acta Part B: Atomic Spectroscopy*, 57(4):609 – 658, 2002.

[13] C. Tendero, C. Tixier, P. Tristant, J. Desmaison, and P. Leprince. Atmospheric pressure plasmas: A review. *Spectrochimica Acta Part B*, 61:2–30, 2006.

[14] H. Conrads and M. Schmidt. Plasma generation and plasma sources. *Plasma Sources Science and Technology*, 9:441–454, 2000.

[15] A. Wu, J. Yan, H. Zhang, M. Zhang, C. Du, and X. Li. Study of the dry methane reforming process using a rotating gliding arc reactor. *International Journal of Hydrogen Energy*, 39(31):17656–17670, 2014.

[16] T. Nunnally, K. Gutsol, A. Rabinovich, A. Fridman, A. Gutsol, and A. Kemoun. Dissociation of CO_2 in a low current gliding arc plasmatron. *Journal of Physics D: Applied Physics*, 44(27):274009, 2011.

[17] S. P. Gangoli, A. F. Gutsol, and A. A. Fridman. A non-equilibrium plasma source: magnetically stabilized gliding arc discharge: I. design and diagnostics. *Plasma Sources Science and Technology*, 19(6):065003, 2010.

[18] A. Bogaerts and E.C. Neyts. Plasma technology: An emerging technology for energy storage. *ACS energy lett.*, 3:1013–1027, 2018.

[19] A. Bourdon. Simulations fluides pour les décharges plasmas froids à pression atmosphérique. La Rochelle, 20-23 October 2014. 12émes Journées d'Echanges du Réseau Plasmas Froids.

[20] R. Brandenburg. Dielectric barrier discharges: progress on plasma sources and on the understanding of regimes and single filaments. *Plasma Sources Science and Technology*, 26(5):053001, mar 2017.

[21] Y. Uytdenhouwen, S. Van Alphen, I. Michielsen, V. Meynen, P. Cool, and A. Bogaerts. A packed-bed DBD micro plasma reactor for CO_2 dissociation: Does size matter? *Chemical Engineering Journal*, 348:557–568, 2018.

[22] R. Aerts, W. Somers, and A. Bogaerts. Carbon dioxide splitting in a dielectric barrier discharge plasma: a combined experimental and cumputational study. *ChemSusChem*, 8:702–716, 2015.

[23] S. Paulussen, B. Verheyde, X. Tu, C. De Bie, T. Martens, D. Petrovic, A. Bogaerts, and B. Sels. Conversion of carbon dioxide to value-added chemicals in atmospheric pressure dielectric barrier discharges. *Plasma Sources Science and Technology*, 19(3), 2010.

[24] Q. Yu, M. Kong, T. Liu, J. Fei, and X. Zheng. Characteristics of the decomposition of CO_2 in a dielectric packed-bed plasma reactor. *Plasma Chemistry and Plasma Processing*, 32(1):153–163, 2012.

[25] A. Ozkan, A. Bogaerts, and F. Reniers. Routes to increase the conversion and the energy efficiency in the splitting of CO_2 by a dielectric barrier discharge. *Journal of Physics D: Applied Physics*, 50:084004, 2017.

[26] F. Brehmer, S. Welzel, M.C.M. Van de Sanden, and R. Engeln. CO and byproduct formation during CO_2 reduction in dielectric barrier discharges. *Journal of Applied Physics*, 116:123303, 2014.

[27] I. Belov, S. Paulussen, and A. Bogaerts. Appearance of a conductive carbonaceous coating in a CO_2 dielectric barrier discharge and its influence on the electrical properties and the conversion efficiency. *Plasma Sources Science and Technology*, 25(1):015023, 2016.

[28] S. Wang, Y. Zhang, X. Liu, and X. Wang. Enhancement of CO_2 conversion rate and conversion efficiency by homogeneous discharges. *Plasma Chemistry and Plasma Processing*, 32(5):979–989, 2012.

[29] J. Wang, G. Xia, A. Huang, S.L. Suib, Y. Hayashi, and H. Matsumoto. CO_2 decomposition using glow discharge plasmas. *Journal of Catalysis*, 185(1):152–159, 1999.

[30] K. Van Laer and A. Bogaerts. Improving the conversion and energy efficiency of carbon dioxide splitting in a zirconia-packed dielectric barrier discharge reactor. *Energy Technology*, 3(10):1038–1044, 2015.

[31] T. Butterworth, R. Elder, and R. Allen. Effects of particle size on CO_2 reduction and discharge characteristics in a packed bed plasma reactor. *Chemical Engineering Journal*, 293:55–67, 2016.

[32] D. Mei, X. Zhu, Y. He, J.D. Yan, and X. Tu. Plasma-assisted conversion of CO_2 in a dielectric barrier discharge reactor: understanding the effect of packing materials. *Plasma sources science and technology*, 24, 2014.

[33] X. Duan, Z. Hu, Y. Li, and B. Wang. Effect of dielectric packing materials on the decomposition of carbon dioxide using DBD microplasma reactor. *AlChE*, 61(3), 2014.

[34] I. Michielsen, Y. Uytdenhouwen, J. Pype, Michielsen B., J. Mertens, F. Reniers, V. Meynen, and A. Bogaerts. CO_2 dissociation in a packed bed DBD reactor: first steps towards a better understanding of plasma catalysis. *Chemical engineering journal*, 326:477–488, 2017.

[35] L.F. Spencer and A.D. Gallimore. Efficiency of CO_2 dissociation in a radio-frequency discharge. *Plasma Chemistry and Plasma Processing*, 31:79–89, 2010.

[36] S.Y. Savinov, H. Lee, H.K. Song, and B.-K. Na. The decomposition of CO_2 in glow discharge. *Korean Journal of Chemical Engineering*, 19:564–566, 2002.

[37] V.D. Rusanov, A.A. Fridman, and G.V. Sholin. The physics of a chemically active plasma with nonequilibrium vibrational excitation of molecules. *Uspekhi Fizicheskikh Nauk*, 134:185–235, 1981.

[38] T. Silva, N. Britun, T. Godfroid, and R. Snyders. Optical characterization of a microwave pulsed discharge used for dissociation of CO_2. *Plasma Sources Science and Technology*, 23(025009), 2014.

[39] L.F. Spencer and A.D. Gallimore. CO_2 dissociation in an atmospheric pressure plasma/catalyst system: a study of efficiency. *Plasma Sources Science and Technology*, 22:15019, 2013.

[40] G.J. Van Rooij, D.C.M. Van den Bekerom, N. Den Harder, T. Minea, G. Berden, W.A. Bongers, R. Engeln, M.F. Graswinckel, E. Zoethout, and M.C.M. Van de Sanden. Taming microwave plasma to beat thermodynamics in CO_2 dissociation. *Faraday Discuss*, 183:233–248, 2015.

[41] W. Bongers, H. Bouwmeester, B. Wolf, F. Peeters, S. Welzel, D. Van den Bekerom, N. Den Harder, A. Goede, M. Graswinckel, P.W. Groen, J. Kopecki, M. Leins, G. Van Rooij, A. Schulz, M. Walker, and R. Van de Sanden. plasma-driven dissociation of CO_2 for fuel synthesis. *Plasma Processes and Polymers*, 14:e1600126, 2017.

[42] A. Vesel, M. Mozetic, A. Drenik, and M. Balat-Pichelin. Dissociation of CO_2 molecules in microwave plasma. *Chemical Physics*, 382:127–131, 2011.

[43] M. Tsuji, T. Tanoue, K. Nakano, and Y. Nishimura. Decomposition of CO_2 into CO and O in a microwave-excited discharge flow of CO_2He or CO_2/Ar mixtures. *Chemistry Letters*, pages 22–23, 2001.

[44] A.P.H. Goede, W.A. Bongers, M.F. Graswinckel, R.M.C.M. Van De Sanden, M. Leins, J. Kopecki, A. Schulz, and M. Walker. Production of solar fuels by CO_2 plasmolysis. *EPJ Web of Conferences*, 79:1005, 2014.

[45] G. Chen, V. Georgieva, T. Godfroid, R. Snyders, and M.P. Delplancke-Ogletree. Plasma assisted catalytic decomposition of CO_2. *Applied Catalysis B: Environmental*, 190:115–124, 2016.

[46] R.I. Asisov, A.K. Vakar, V.K. Jivotov, M.F. Krotov, O.A. Zinoviev, B.V. Potapkin, A.A. Rusanov, V.D. Rusanov, and A.A. Fridman. Nonequilibrium plasma-chemical process of CO_2 decomposition in a supersonic microwave discharge. *Proceedings of the USSR Academy of Sciences*, 271:94–98, 1983.

[47] A. Indarto, J. Choi, H. Lee, and H.K. Song. Conversion of CO_2 by gliding arc discharge. *Environmental Engineering Science*, 23(6):1033–1043, 2006.

[48] A. Indarto, J.-W. Choi, H. Lee, and H.K. Song. Gliding arc plasma processing of CO_2 conversion. *Journal of Hazardous Materials*, 146:309–315, 2007.

[49] M. Ramakers, G. Trenchev, S. Heijkers, W. Wang, and A. Bogaerts. Gliding arc plasmatron: Providing an alternative method for carbon dioxide conversion. *ChemSusChem*, 10(12), 2017.

[50] J.L. Liu, H.W. Park, W.J. Chung, and D.W. Park. High-efficient conversion of CO_2 in AC-pulsed tornado gliding arc plasma. *Plasma Chemistry and Plasma Processing*, 36:437–449, 2017.

[51] S.C. Kim, M.S. Lim, and Y.N. Chun. Reduction characteristics of carbon dioxide using a plasmatron. *Plasma Chemistry and Plasma Processing*, 34:125–143, 2014.

[52] S.R. Sun, H.X. Wang, D.H. Mei, X. Tu, and A. Bogaerts. CO_2 conversion in a gliding arc plasma: performance improvement based on chemical reaction modeling. *Journal of CO_2 Utilization*, 17:220–234, 2017.

[53] S.N. Andreev, V.V. Zakharov, V.N. Ochkin, and S.Y. Savinov. Plasma-chemical CO_2 decomposition in a non-self-sustained discharge with a controlled electronic component of plasma. *Spectrochimica Acta Part A: Molecular and Biomolecular Spectroscopy*, 60:3361–3369, 2004.

[54] W. Xu, M.-W. Li, G.W. Xu, and L Tian, Y. Decomposition of CO_2 using DC corona discharge at atmospheric pressure. *Japanese Journal of Applied Physics*, 43(12):8310–8311, 2004.

[55] Y. Wen and X. Jiang. Decomposition of CO_2 using pulsed corona discharges combined with catalyst. *Plasma Chemistry and Plasma Processing*, 21:665–678, 2001.

[56] M.S. Bak, S.K. Im, and M. Cappelli. Nanosecond-pulsed discharge plasma splitting of carbon dioxide. *IEEE Transactions on Plasma Science*, 43:1002–1007, 2015.

[57] S.L. Brock, M. Marquez, S.L. Suib, Y. Hayaschi, and H. Matsumoto. Plasma decomposition of CO_2 in the presence of metal catalysts. *Journal of Catalysis*, 180:225–233, 1998.

[58] T. Kozk and A. Bogaerts. Evalutaion of the energy efficiency of CO_2 conversion in microwave discharges using a reaction kinetics model. *Plasma Sources Sci. Technol.*, 24:015024, 2015.

[59] M. Ramakers, I. Michielsen, R. Aerts, V. Meynen, and A. Bogaerts. Effect of argon or helium on the CO_2 conversion in a dielectric barrier discharge. *Plasma Processes and Polymers*, 12:755–763, 2015.

[60] S. Heijkers, R. Snoeckx, T. Kozk, T. Silva, T. Godfroid, N. Britun, R. Snyders, and A. Bogaerts. CO_2 conversion in a microwave plasma reactor in the presence of N_2: Elucidating the role of vibrational levels. *Journal of Physical Chemistry*, 119:12815–12828, 2015.

[61] R. Snoeckx, S. Heijkers, K. Van Wesenbeeck, S. Lenaerts, and A. Bogaerts. CO_2 conversion in a dielectric barrier discharge plasma: N_2 in the mix as a helping hand or problematic impurity? *Energy & Environmental Science*, 9:999–1011, 2016.

[62] U. Fantz. Basics of plasma spectroscopy. *Plasma Sources Science and Technology*, 15(4):S137, 2006.

[63] Bronkhorst. *OceanView: Installation and Operation Manual*, 2018. (000-20000-310-02-201602c).

[64] Bronkhorst. *General instructions digital mass flow/pressure instruments laboratory style/in-flow*, May 2018. (917.022AA).

[65] NIST Physical Measurement Laboratory. Handbook of basic atomic spectroscopic data. `https://www.nist.gov/pml/handbook-basic-atomic-spectroscopic-data`, 2013. accessed: 27-09-2018.

[66] R.W.B. Pearse and A.G. Gaydon. *The identification of Molecular Spectra*. Wiley, 4 edition, 1976.

[67] F. Deeba, A. Qayyum, and N. Mahmood. Optical emission spectroscopy of 2.45 ghz microwave induced plasma. 2015, 01 2015.

[68] P. Chapelle, T. Czerwiec, J.P. Bellot, A. Jardy, D. Lasalmonie, J. Senevat, and D. Ablitzer. Plasma diagnostic by emission spectroscopy during vacuum arc remelting. 11:301, 06 2002.

[69] A. Qayyum, M. Ikram, M. Zakaullah, A. Waheed, G. Murtaza, R. Ahmad, A. Majeed, N.A.D. Khattak, K. Mansoor, and K.A. Chaudhary. Characterization of argon plasma by use of optical emission spectroscopy and langmuir probe measurements. *International Journal of Modern Physics B*, 17(14):2749–2759, 2003.

[70] Y. Vitel, M. Lamoureux, H. Abada, A. Lejeune, C. Faure, P. Le Tourneur, X. Godechot, and S. Cochard. Spectroscopic investigation of vacuum-arc anode plasmas for thin film deposition. *Plasma Sources Science and Technology*, 11:333–337, 2002.

[71] P.J. Bruggeman. Gas temperature determination from rotational lines in non-equilibrium plasmas: a review. *Plasma Sources Science and Technology*, 23(023001), 2014.

[72] C. Engelhard, G.C.-Y. Chan, G. Gamez, W. Buscher, and G.M. Hieftj. Plasma diagnostic on a low-flow plasma for inductively coupled plasma optical emission spectrometry. *Spectrochimica Acta Part B: Atomic Spectroscopy*, 63(6):619 – 629, 2008.

[73] M.A. Gigosos, M.A. Gonzalez, and V. Cardenoso. Computer simulated balmer-alpha, -beta and -gamma stark line profiles for non-equilibrium plasmas diagnostics. *Spectrochimica Acta Part B: Atomic Spectroscopy*, 58:1489–1504, 2003.

[74] L. Yang, X. Tan, X. Wan, L. Chen, D. Jin, M. Qian, and Q. Li. Stark broadening for diagnostics of the electron density in non-equilibrium plasma utilizing isotope hydrogen alpha lines. *Journal of Applied Physics*, 115(163106), 2014.

[75] J. Torres, J.M. Palomares, A. Sola, J.J.A.M. Van der Mullen, and A. Gamero. A stark broadening method to determine simultaneously the electron temperature and density in high-pressure microwave plasmas. *Journal of Physics D: Applied Physics*, 40:5929–5936, 2007.

[76] W.L. Wiese, M.W. Smith, and B.M. Miles. *Atomic transition probabilities - sodium through calclium*, volume II of *NSRDS-NBS 22*. 1969.

[77] D.L. Crintea, U. Czarnetzki, S. Lordanova, S. Koleva, and D. Luggenholscher. Plasma diagnostics by optical emission spectroscopy on argon and comparison with thomson scattering. *Journal of Physics D: Applied Physics*, 42(4), 2009.

[78] A. Palmero, E.D. Van Hattum, H. Rudolph, and F.H.P.M. Habraken. Characterization of a low-pressure argon plasma using optical emission spectroscopy and a global model. *Journal of Applied Physics*, 101:053306, 2007.

[79] R. Miotk, B. Hrycak, M. Jasinski, and J. Mizeraczyk. Characterization of an atmospheric-pressure argon plasma generated by 915 MHz microwaves using optical emission spectroscopy. *Journal of Physics D: Applied Physics*, 42(4), 2009.

[80] A.A. Garamoon, A. Samir, F.F. Elakshar, A. Nosair, and E.F. Kotp. Optical emission spectroscopy of CO_2 glow discharge at low pressure. *IEEE Transactions on Plasma Science*, 35(1), 2007.

[81] E.F. Mendez-Martinez, P.G. Reyes, D. Osorio-Gonzalez, F. Castillo, and H. Martinez. Langmuir probe and optical emission spectroscopy studies of low-pressure gas mixture CO_2 and N_2. *Plasma Science and Technology*, 12(3), 06 2010.

[82] P.G. Reyes, E.F. Mendez, D. Osorio-Gonzalez, F. Castillo, and H. Martinez. Optical emission spectroscopy of CO_2 glow discharge at low pressure. *Physica Status Solidi (C)*, 5(4):907–910, 2008.

[83] M.J. Mumma, E.J. Stone, and E.C. Zipf. Excitation of the CO fourth positive band system by electron impact on carbon monoxide and carbon dioxide. *The Journal of Chemical Physics*, 54(2627), 1971.

[84] Y. Du, K. Tamura, S. Moore, Z. Peng, T. Nozaki, and P.J. Bruggeman. CO($B^1\Sigma^+ \rightarrow A^1\Pi$) Angstrom system for gas temperature measurements in CO_2 containing plasmas. *Plasma Chemistry and Plasma Processing*, 37:29–41, 2017.

[85] F.J. Gordillo-Vázquez, M. Camero, and C. Gómez-Aleixandre. Spectroscopic measurements of the electron temperature in low pressure radiofrequency $Ar/H_2/C_2H_2$ and $Ar/H_2/CH_4$ plasmas used for the synthesis of nanocarbon sturctures. *Plasma Sources Science and Technology*, 15:42–51, 2006.

A

Experimental Data

Table A.1: Gas chromatography results of a pure CO_2 discharge over time at a reactor length of 300mm

Pressure	Power	Time stamp	H_2	O_2	N_2	CH_4	CO	CO_2	Conversion
10 mbara	2 kW	0.00 - 1.30 min	0%	19.701%	67.253%	0.033%	5.518%	7.001%	44.08%
10 mbara	2 kW	3.00 - 4.30 min	0.001%	19.681%	67.378%	0.015%	5.861%	6.853%	46.10%
10 mbara	2 kW	10.00 - 11.30 min	0%	19.32%	68.843%	0.001%	5.397%	6.134%	46.80%
10 mbara	2 kW	20.00 - 21.30 min	0%	19.331%	68.015%	0.002%	5.984%	6.637%	47.41%
10 mbara	2 kW	Null result	0%	18.624%	69.676%	0.021%	0.385%	11.307%	3.29%

Table A.2: Continued experimental results of a pure CO_2 discharge over time at a reactor length of 300mm

Pressure	Power	Time stamp	Voltage (V)	Current (A)	Power (PL)	Flow rate (FT)	Energy Efficiency
10 mbara	2 kW	0.00 - 1.30 min	102.0 V	3.8 A	945.0 W	14.3 NmL_{N_2}/min	0.23 %
10 mbara	2 kW	3.00 - 4.30 min	100.6 V	3.7 A	933.3 W	14.3 NmL_{N_2}/min	0.24 %
10 mbara	2 kW	10.00 - 11.30 min	100.5 V	3.7 A	928.6 W	14.3 NmL_{N_2}/min	0.24 %
10 mbara	2 kW	20.00 - 21.30 min	100.0 V	3.7 A	914.9 W	14.3 NmL_{N_2}/min	0.25 %

Table A.3: Gas chromatography results of a CO_2 with a 30 mbara Ar admixutre reactor over time at a discharge length of 300mm

Pressure	Power	Time stamp	H_2	O_2	N_2	CH_4	CO	CO_2	Conversion
30 mbara	2 kW	0.00 - 1.30 min	0%	9.601%	26.676%	0.033%	3.083%	3.855%	44.44%
30 mbara	2 kW	3.00 - 4.30 min	0%	9.58%	26.695%	0.021%	3.06%	3.841%	44.34%
30 mbara	2 kW	10.00 - 11.30 min	0%	9.15%	24.717%	0.011%	3.667%	4.04%	47.58%
30 mbara	2 kW	20.00 - 21.30 min	0%	9.374%	25.785%	0.032%	3.722%	3.883%	48.94%
30 mbara	2 kW	Null result	0.001%	7.981%	25.84%	0.004%	0.279%	7.104%	3.78%

Table A.4: Gas chromatography results of a CO_2 with a 100 mbara Ar admixutre reactor over time at a discharge length of 300mm

Pressure	Power	Time stamp	H_2	O_2	N_2	CH_4	CO	CO_2	Conversion
100 mbara	2 kW	0.00 - 1.30 min	0%	4.998%	12.623%	0.03%	1.744%	1.839%	48.67%
100 mbara	2 kW	3.00 - 4.30 min	0%	4.249%	10.159%	0.014%	2.027%	1.832%	52.52%
100 mbara	2 kW	10.00 - 11.30 min	0.001%	4.229%	9.962%	0.036%	1.993%	1.766%	53.02%
100 mbara	2 kW	20.00 - 21.30 min	0.001%	4.314%	9.811%	0.003%	2.778%	1.739%	61.50%
100 mbara	2 kW	Null result	0.001%	3.504%	11.102%	0.014%	0.218%	0.121%	64.31%

Table A.5: Gas chromatography results of a pure CO_2 discharge at various pressure (10-75 mbara) and various power levels (1-2 kW), at a reactor length of 120mm

Pressure	Power	H_2	O_2	N_2	CH_4	CO	CO_2	Conversion
11 mbara	1 kW	0.002%	19.505%	61.391%	0%	6.315%	11.981%	34.52%
10 mbara	1 kW	0%	19.704%	63.531%	0.033%	5.486%	10.204%	34.96%
10 mbara	1 kW	0.001%	20.105%	61.492%	0.004%	7.222%	9.767%	42.51%
11 mbara	2 kW	0%	20.517%	59.984%	0.028%	10.174%	8.009%	55.95%
10 mbara	2 kW	0.001%	18.686%	62.487%	0%	5.45%	12.929%	29.65%
10 mbara	2 kW	0%	20.106%	66.233%	0.008%	6.422%	7.123%	47.41%
32 mbara	1 kW	0%	14.296%	30.653%	0.052%	9.574%	42.499%	18.39%
30 mbara	1 kW	0%	13.831%	27.682%	0.057%	10.724%	44.492%	19.42%
32 mbara	1 kW	0%	13.918%	28.683%	0.011%	10.185%	44.746%	18.54%
36 mbara	2 kW	0%	17.784%	27.378%	0.014%	17.614%	32.921%	34.86%
33 mbara	2 kW	0%	17.456%	26.926%	0.032%	17.573%	33.405%	34.47%
34 mbara	2 kW	0%	16.389%	27.562%	0.016%	14.92%	36.514%	29.01%
67 mbara	1 kW	0%	8.158%	15.155%	0.001%	6.774%	70.292%	8.79%
73 mbara	1 kW	0%	8.33%	14.559%	0.026%	6.454%	70.563%	8.38%
65 mbara	1 kW	0%	8.006%	15.509%	0%	6.287%	70.139%	8.23%
67 mbara	2 kW	0%	13.9%	17.07%	0%	16.165%	50.52%	24,24%

Table A.6: Continued experimental results of a pure CO_2 discharge at various pressure (10-75 mbara) and various power levels (1-2 kW), at a reactor length of 120mm

Pressure	Power	Voltage (V)	Current (A)	Power (PL)	Flow rate (FT)	Energy Efficiency
11 mbara	1 kW	167.2 V	3.1 A	826.1 W	18.9 NmL_{N_2}/min	0.56%
10 mbara	1 kW	167.7 V	3.2 A	847.9 W	13.4 NmL_{N_2}/min	0.40%
10 mbara	1 kW	169.0 V	3.1 A	847.2 W	17.9 NmL_{N_2}/min	0.61%
11 mbara	2 kW	152.2 V	5.7 A	1360 W	18.7 NmL_{N_2}/min	0.44%
10 mbara	2 kW	154.0 V	5.8 A	1395 W	17.7 NmL_{N_2}/min	0.22%
10 mbara	2 kW	153.2 V	5.9 A	1389 W	11.6 NmL_{N_2}/min	0.24%
32 mbara	1 kW	151.1 V	2.7 A	739.3 W	138.5 NmL_{N_2}/min	1.94%
30 mbara	1 kW	152.3 V	2.7 A	754.7 W	135.4 NmL_{N_2}/min	1.89%
32 mbara	1 kW	151.3 V	2.7 A	747.4 W	143 NmL_{N_2}/min	1,95%
36 mbara	2 kW	141.2 V	5.1 A	1249 W	147.8 NmL_{N_2}/min	1.99%
33 mbara	2 kW	139.9 V	5.2 A	1225 W	133.6 NmL_{N_2}/min	1.93%
34 mbara	2 kW	140.0 V	4.9 A	1232 W	133.1 NmL_{N_2}/min	1.43%
67 mbara	1 kW	142.8 V	2.4 A	649.1 W	348.5 NmL_{N_2}/min	2.67%
73 mbara	1 kW	135.2 V	2.4 A	608.9 W	370.3 NmL_{N_2}/min	3.09%
65 mbara	1 kW	141.4 V	2.5 A	636.5 W	328 NmL_{N_2}/min	2.71%
67 mbara	2 kW	120.0 V	4.2 A	1001 W	312.2 NmL_{N_2}/min	3.17%

Table A.7: Gas chromatography results of a pure CO_2 discharge at 30 mbara, 2 kW with various gas feed rates, at a reactor length of 120mm

Pressure	Power	H_2	O_2	N_2	CH_4	CO	CO_2	Conversion
30 mbara	2 kW	0.003%	12.919%	14.619%	0.02%	15.434%	55.161%	21.86%
31 mbara	2 kW	0.003%	14.458%	16.132%	0.034%	17.349%	49.468%	25.96%
31 mbara	2 kW	0.005%	16.706%	28.603%	0.036%	15.444%	34.822%	30.72%
32 mbara	2 kW	0%	16.919%	48.638%	0%	6.89%	25.621%	21.19%
30 mbara	2 kW	0.006%	17.352%	25.03%	0.017%	18.01%	34.772%	34.12%
30 mbara	2 kW	0%	14.47%	16.068%	0.009%	17.803%	48.459%	26.87%
31 mbara	2 kW	0.008%	11.685%	11.838%	0.046%	14.789%	59.7%	19.85%
30 mbara	2 kW	0.004%	17.72%	29.11%	0.032%	16.871%	31.967%	34.54%
30 mbara	2 kW	0%	18.081%	24.774%	0.034%	18.855%	33.072%	36.31%
31 mbara	2 kW	0.001%	18.676%	49.48%	0.055%	10.179%	19.528%	34.26%
30 mbara	2 kW	0%	15.261%	18.554%	0.016%	17.371%	45.087%	27.81%

Table A.8: Continued experimental results of a pure CO_2 discharge at 30 mbara, 2 kW with various gas feed rates, at a reactor length of 120mm

Pressure	Power	Voltage (V)	Current (A)	Power (PL)	Flow rate (FT)	Energy Efficiency
30 mbara	2 kW	142.1 V	5.3 A	1260 W	314 NmL_{N_2}/min	2.80%
31 mbara	2 kW	140.5 V	5.4 A	1252 W	277.9 NmL_{N_2}/min	3.05%
31 mbara	2 kW	142.6 V	5.2 A	1265 W	122.8 NmL_{N_2}/min	1.47%
32 mbara	2 kW	140.3 V	5.0 A	1229 W	51.1 NmL_{N_2}/min	0.42%
30 mbara	2 kW	140.5 V	5.1 A	1234 W	147.4 NmL_{N_2}/min	2.00%
30 mbara	2 kW	144.8 V	5.1 A	1282 W	278.4 NmL_{N_2}/min	2.78%
31 mbara	2 kW	141.0 V	5.1 A	1249 W	398.1 NmL_{N_2}/min	3.04%
30 mbara	2 kW	143.1 V	5.1 A	1271 W	119.2 NmL_{N_2}/min	1.54%
30 mbara	2 kW	144.2 V	5.2 A	1286 W	139.5 NmL_{N_2}/min	1.92%
31 mbara	2 kW	144.8 V	5.3 A	1277 W	43.9 NmL_{N_2}/min	0.61%
30 mbara	2 kW	142.1 V	5.1 A	1265 W	234.2 NmL_{N_2}/min	2.44%

B

Diagrams

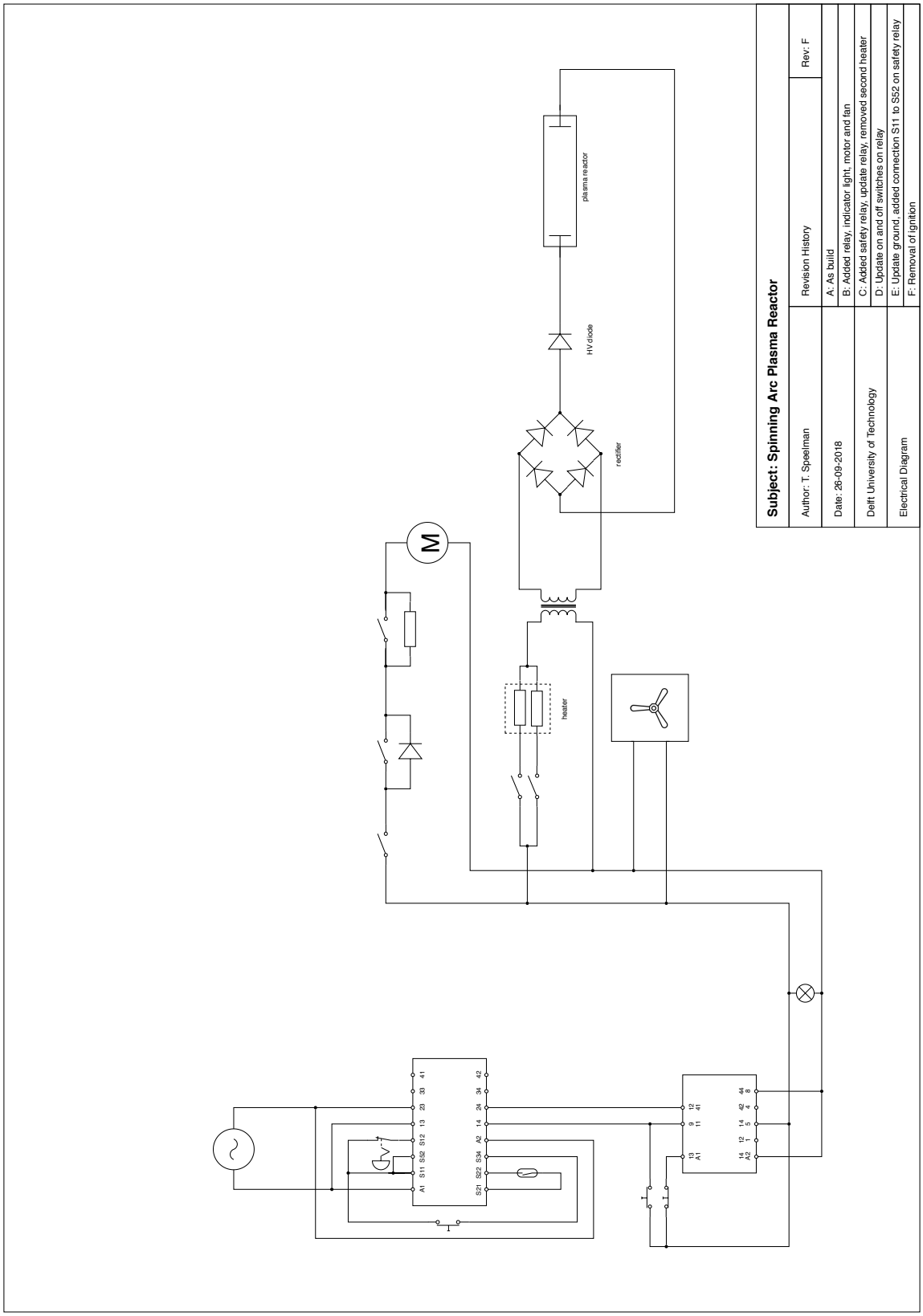
plasma reactor
HV diode
rectifier
heater
M
Subject: Spinning Arc Plasma Reactor
Author: T. Speelman
Date: 26-09-2018
Delft University of Technology
Electrical Diagram
Revision History
Rev: F
A: As build
B: Added relay, indicator light, motor and fan
C: Added safety relay, update relay, removed second heater
D: Update on and off switches on relay
E: Update ground, added connection S11 to S52 on safety relay
F: Removal of ignition